

Motion at low Reynolds number

by

Daniel See-Wai Tam

Submitted to the Department of Aeronautics and Astronautics
in partial fulfillment of the requirements for the degree of

Doctor of Philosophy

at the

MASSACHUSETTS INSTITUTE OF TECHNOLOGY

September 2008

© Massachusetts Institute of Technology 2008. All rights reserved.

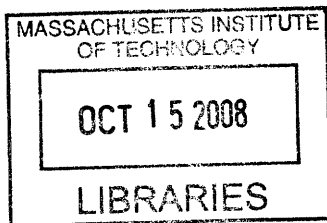
Author .. Department of Aeronautics and Astronautics
June 27, 2008

Certified by A. E. Hosoi
Associate Professor of Mechanical Engineering
Thesis Supervisor

Certified by..... Karen E. Willcox
Associate Professor of Aeronautics and Astronautics
Thesis Committee Chair

Certified by Roman Stocker
Doherty Assistant Professor of Ocean Utilization
Thesis Committee Member

Accepted by ... David L. Darmofal
Associate Department Head
Chair, Committee on Graduate Students



ARCHIVES

Motion at low Reynolds number

by

Daniel See-Wai Tam

Submitted to the Department of Aeronautics and Astronautics
on June 27, 2008, in partial fulfillment of the
requirements for the degree of
Doctor of Philosophy

Abstract

The work described in this thesis centers on inertialess motion at low Reynolds numbers at the crossroad between biofluids and microfluids. Here we address questions regarding locomotion of micro-swimmers, transport of nutrient around micro-organisms as well as mixing and heat exchange inside micro-droplets of water.

A general framework for the investigation of optimal locomotion strategies for slender swimmers has been developed and applied to different systems. Here we exclusively study the hydrodynamical aspects of locomotion without further consideration for the swimmers internal dynamics. The first system studied is the “three-link” swimmer, first introduced and discussed by Nobel prize laureate E.M. Purcell in his famous lecture “Life at low Reynolds number” [121]. For this simple swimmer, we find and later discuss optimal stroke kinematics and swimmer geometries. We then further investigate flagellated swimmers and verify the convergence of the optimization procedure in the case of a single flagellum, for which the optimal stroke kinematics are known analytically. Optimal stroke kinematics and geometries for unflagellates are also computed and found to be relevant in the context of biological microorganisms. We then turn our attention to stroke kinematics of biflagellates and demonstrate that all the different strokes, which are experimentally observed to be performed by biflagellated organisms such as green algae *chlamydomonas*, are found to be local hydrodynamical optima. These observations strongly suggest the central role of hydrodynamics in the internal dynamical organization of the stroke patterns.

Finally, we present experimental results on convective transport and mixing inside small droplets of water sitting on superhydrophobic substrates. We demonstrate by a scaling analysis, that the regular convection pattern is due to a thermocapillary driven Marangoni flow at the surface of the droplet. We develop an analytical solution for the temperature and flow field inside the droplet, which is found to be in agreement with our experimentally recorded data.

Thesis Supervisor: A. E. Hosoi

Title: Associate Professor of Mechanical Engineering

Acknowledgments

First I want to thank Professor A.E. Hosoi, “Peko”, for giving an opportunity to a student in Aeronautics to join her group and work on *very* low Reynolds number fluid dynamics. Working with her has been a real learning experience. Her enthusiastic approach to science through asking relevant, simple and fun questions has challenged and changed how I consider my own work. It is also quite remarkable how she was involved in my project and always willing to discuss and provide detailed help but, at the same time, gave me all the freedom I wanted to explore new problems. Equally remarkable is how she always encouraged me in my work and managed to take the pressure off my shoulders rather than putting it on them.

I am also grateful to my thesis committee Professor Roman Stocker and Professor Karen Willcox for their time, advice, guidance and encouragement over the years. Their comments and suggestions have helped me structure my project from the beginning and improve my work.

I want to thank Professor Gareth McKinley and Doctor Volkmar von Arnim, who initiated the work on the thermocapillary driven Marangoni flow. I want to particularly thank Volkmar for helping me in setting up the experiments in the early stage of the project and for making this first experimental experience enjoyable.

I want to thank Professor Eric Lauga for fruitful and challenging discussion throughout my PhD and for encouraging me on many occasions to aim for more. I also thank Professor Eric Lauga and Doctor Roland Bouffanais for reading my thesis and particularly Roland for useful suggestions on the manuscript and help in implementing them.

The past few years would not have been as enjoyable without all my friends and colleagues in HML. Although many of them have left, all of them have contributed to making my daily life in lab so pleasant. In particular, I want to thank all my labmates: Amos, Brian, Dawn, Randy, Sarah, Sungyon, Tony (Number One forever!) and, of course, Debbie! Each one of you has helped and encouraged me in so many different ways. I truly count myself lucky for having been part of such a wonderful

and stimulating research group.

I also want to thank all the friends I made over the years at the MIT Graduate Christian Fellowship and at Cambridgeport Baptist Church for their friendship, support and prayers. In particular, I want to thank Damien, my fellow Frenchman and brother in Christ, for his help and wisdom in the few important decisions I had to make during my time here.

I am grateful for the support and love of my entire family and particularly my parents, who have inspired me again and again throughout the years. Thank you for your patience and for being such an encouraging model of strength, perseverance and steadfastness.

The best part of being at MIT has been meeting Marie-Eve, my wife, and getting to know her better every day. Not only did she encourage and support me with her love, friendship and prayers through these years of graduate work but she also helped and challenged me scientifically as she initiated and suggested many of the ideas which are now part of this thesis. Thank you. I hope Raphaëlle will grow up to look like you one day.

Finally I want to give glory and express my deepest gratitude to my father in heaven, without whom none of this would be and through whom all things are possible.

Trust in the Lord with all your heart and lean not on your own understanding; in all your ways acknowledge him, and he will make your paths straight.

Proverbs 3:5-6

Contents

1	Introduction	21
1.1	Motivations	21
1.2	Outline and contributions	23
2	Low Reynolds number locomotion	27
2.1	Previous work on micro-swimming	27
2.2	Motivations	30
2.3	Modeling approach	33
2.3.1	Representation of a swimming organism	33
2.3.2	Low Reynolds number hydrodynamics	34
2.3.3	Dynamics of the swimmer	36
2.3.4	Locomotion optimization	40
2.3.5	Summary	45
3	Optimizing Purcell’s three-link swimmer	47
3.1	Introduction	47
3.2	Methods	49
3.2.1	Geometry of the three-link swimmer	49
3.2.2	Hydrodynamics	51
3.2.3	Equations of motion	53
3.2.4	Optimization of the three-link swimmer	54
3.3	Optimal strokes for the three-link swimmer	57
3.3.1	Limit of infinitely slender swimmers	57

3.3.2	Effect of finite slenderness	62
3.3.3	Convergence and optimality analysis	64
3.4	Investigating large amplitude strokes	66
3.4.1	Large amplitude strokes of O. Raz and J.E. Avron	66
3.4.2	Efficient large amplitude strokes	68
3.4.3	Optimizing the distance traveled over one stroke	72
4	Optimal unflagellated swimmers	75
4.1	Introduction	75
4.2	Methods	76
4.2.1	Geometry and deformation of the swimmer	77
4.2.2	Hydrodynamics around the swimmer	79
4.2.3	Governing equations	85
4.2.4	Numerical approach	86
4.2.5	Optimization procedure	89
4.3	Validation of the model	93
4.3.1	Analytical optimal for a single-tail swimmer	93
4.3.2	Comparison between analytical and numerical optimal	95
4.4	Optimal stroke kinematics for unflagellates	98
4.4.1	Description of the optimal stroke kinematics	99
4.4.2	Influence of head shape on optimal stroke kinematics	100
4.5	Optimal morphology for unflagellates	105
4.5.1	Optimal ratio of tail length to head length	105
4.5.2	Comparison with reported data on sperm morphology	107
5	Optimizing biflagellates	113
5.1	Introduction	113
5.2	Modeling of the dynamics of biflagellates	114
5.2.1	Geometry of the swimmer	114
5.2.2	Dynamics of the swimmer	115
5.2.3	Optimization procedure	116

5.3	Optimal biflagellated swimmers	118
5.3.1	Swimming efficiency for biflagellates	118
5.3.2	Optimal strokes	119
5.4	Optimal biflagellated feeders	122
5.4.1	Scaling analysis for the transport problem	122
5.4.2	Feeding efficiency for biflagellates	123
5.4.3	Optimal breaststroke for feeding	124
5.4.4	Optimal breaststroke for swimming	126
6	Marangoni convection in droplets on superhydrophobic surfaces	129
6.1	Introduction	129
6.2	Experimental methods	133
6.2.1	Background	133
6.2.2	Experimental setup	133
6.3	Physical model	136
6.3.1	Scaling analysis	138
6.3.2	Governing equations	141
6.3.3	Boundary conditions	143
6.4	Analytical solution	145
6.4.1	Nondimensionalization	145
6.4.2	Temperature field	146
6.4.3	Velocity field	147
6.5	Experimental validation of the model	149
6.5.1	Optical correction for spherical droplet	149
6.5.2	Experimental and analytical results comparison	150
6.6	Validity of the point heat source assumption	154
6.7	Effect of finite Péclet number	156
6.8	Discussion	159
7	Conclusions and outlook	161
7.1	Summary	161

7.2	Future work	164
A	Three-link swimmer coefficients	167
A.1	Expression for drag coefficients	167
A.2	Expression for the artificial lubrication	171
B	Numerical discretization of flagellated swimmers	173
C	Analytical solution for temperature and velocity	177
C.1	Derivation of the solution	177
C.2	Properties of Gegenbauer polynomials	179

List of Figures

1-1	Schematic representation of how the length scale of recent technological innovations compare with biological systems. Red box highlights length scales of interest in the work presented herein. Pictures are reproduced from: myosin [63], E-coli [11], paramecium [130], robosnail [28], robotic fly [166], environmental microfluidics [148], artificial cilia [50]	22
2-1	“A general overview of microorganisms with flagella and related organisms”. (Reproduced from [100])	31
2-2	“The modular structure of a flagellum”. (Reproduced from [162]) . .	32
2-3	Swimmer undergoing one stroke or periodic deformation of period T . The surface is represented at time 0, t and T , which relevant notations.	33
2-4	Schematic representation of a given stroke undergone at different time parameterization functions $q(t)$	38
3-1	Schematic of the swimmer. The slice and corresponding notation on the left refer to the local velocity, tangent vector and drag force per unit length. Notation on the right refers to the velocity, tangent vector and force associated with an entire link. Note that (F_i^x, F_i^y) and (\dot{x}_i, \dot{y}_i) lie in the $x - y$ plane while $\dot{\theta}_i$ and τ_i point out of the page in the \hat{z} direction.	49
3-2	Representation in the (φ_1, φ_2) -phase plane of initial stroke sequences used in the optimization of the three-link swimmer.	60

3-3	Stroke sequences of three-link swimmers in the (φ_1, φ_2) -phase plane for: (black line) optimal efficiency, (medium gray line) optimal velocity and (light gray line) the optimal “Purcell stroke” which corresponds to the square. Small swimmer diagrams correspond to successive configurations of the swimmer during the stroke. The swimmer moves to the left when the trajectory is followed counterclockwise and to the right otherwise.	61
3-4	Efficiency of the three-link swimmer as a function of slenderness. . .	63
3-5	(a): Semi-log plot showing exponential decay of the amplitude of the Fourier coefficients. (b): Log-log plot of the normalized error in the efficiency as a function of the number of terms in the Fourier series used to find the optimal stroke. (c): Efficiency as a function of the two dominant terms in the Fourier expansion.	65
3-6	(a): Three-link swimmer strokes from O. Raz and J.E. Avron. The plot is reproduced from [126] with its original caption: “The φ_1 and φ_2 are the exterior angles made by the center link and the two arms. The approximate rectangle (green) represents the distance optimizer of the moderate strokes of Tam and Hosoi [153]. The (blue) dumbbell is a large stroke that outperforms the moderate stroke. The approximate (light-blue) circle in the center represents the efficiency optimizer of the moderate strokes found by Tam and Hosoi [153]. The off-center (red) wobble oval is a large stroke with higher efficiency”. (b): Optimal large amplitude stroke for swimming efficiency.	67
3-7	Efficiency of our optimized stroke and that of Raz and Avron as a function of $1/\kappa$	71

4-1	Schematic of a uniflagellated swimmer. The slice and corresponding notation on the right refer to the local velocity, tangent vector and drag force per unit length. Note that for the forces and velocities on the head \mathbf{F}_0 and \mathbf{U}_0 lie in the $\hat{\mathbf{x}} - \hat{\mathbf{y}}$ plane while τ_0 and Ω_0 point out of the page in the $\hat{\mathbf{z}}$ direction.	77
4-2	Spatial discretization of the flagellum	87
4-3	Schematic of single-tail swimmer with notation used in the analytical derivation of optimal stroke kinematics.	94
4-4	Representation of typical initial guesses for the optimization of the single-tail swimmer.	96
4-5	(a) Analytical solution for an optimal single-tail swimmer of periodic waveform. (b) Computed optimal single-tail swimmer. (c-d) Timeshots of the curvature distribution γ and angle θ as a function of the arc-length for the computed optimal kinematics of a single-tail swimmer.	97
4-6	Fluorescence microscopy image of human spermatozoa adapted from Neuhaus <i>et al.</i> [113] representing the different parts of a sperm cell.	98
4-7	Representation of typical initial strokes for the optimization of uniflagellated swimmers.	99
4-8	(a) Timeshots of the curvature distribution γ as a function of the arc-length for the optimal stroke of a uniflagellated swimmer with a head of eccentricity of 0.67. (b) Same for a head of eccentricity 0.2.	100
4-9	Representation of optimal stroke kinematics for: (a) single-tail swimmer, (b) uniflagellated swimmer with eccentricity for the head of $e = 1.0$, (c) $e = 0.8$, (d) $e = 0.6$, (e) $e = 0.4$, (f) $e = 0.2$	101
4-10	Variation of the total curvature Γ as the wave propagates down the flagellum for: the single-tail swimmer, uniflagellated swimmers with eccentricity for the head of $e = 1.0$, $e = 0.8$, $e = 0.6$, $e = 0.4$ and $e = 0.2$. Shaded area represent regions for which end effects cannot be neglected in the computation of the total curvature.	102

4-11	(circles): Efficiency of optimal unflagellated swimmers as a function of the eccentricity of the head. (squares): Efficiency for a unflagellated swimmer with eccentricity e whose stroke is the optimal traveling wave of the single-tail swimmer.	103
4-12	Efficiency as a function of the length $2L$ of the flagellum for various sizes of the head L_0 . The black dashed line corresponds to results from J.L.L. Higdon [74] after the data has been renormalized.	106
4-13	Optimal length of the flagellum $2L$ as a function of the size of the head L_0 (black line). Symbols represents data measured experimentally on 302 species of mammalian sperm.	109
4-14	Efficiency normalized with the maximum efficiency as a function of the tail to head size ratio L/L_0 . Histogram represents the relative number of species found to have a given tail to head length ratio L/L_0 in the data set of 302 species.	110
4-15	Efficiency normalized with the maximum efficiency as a function of the tail to head length ratio L/L_0 . Histogram represents the relative number of species found to have a given flagellum length to head size ratio L/L_0 . In this case the data has been rescaled depending on the number of recorded mammalian species in each order to correct for oversampling of a given order.	111
5-1	Schematic of a biflagellated swimmer and related notation.	115
5-2	Representation of typical initial strokes for the optimization of biflagellated swimmers.	118
5-3	Representation of stroke patterns of <i>chlamydomonas</i> using high-speed cinematography, reproduced from Ruffer and Nultsch [131,134]. (a) Free swimming <i>chlamydomonas</i> undergoing an undulatory beat [134]. (b) Representation of an undulatory stroke, in the frame of reference linked to the cell [134]. (c) Computed undulatory stroke optimized for swimming efficiency.	120

5-4	Time snapshots of the curvature γ as a function of the arc-length for all optimal strokes found. Each stroke is further represented by a sequence of shapes. (a) Strokes optimized for swimming efficiency with small amplitude symmetric initial guess. (b) Strokes optimized for swimming with small amplitude antisymmetric initial guesses. (c) Strokes optimized for swimming with large amplitude symmetric initial guesses. (d) Strokes optimized for swimming using optimal feeding stroke as the initial guess. (e) Strokes optimized for feeding.	121
5-5	Representation of stroke patterns of <i>chlamydomonas</i> using high-speed cinematography, reproduced from Ruffer and Nultsch [131,134]. (a) Free swimming <i>chlamydomonas</i> undergoing a breaststroke beat [131]. (b) Representation of a breaststroke, in the frame of reference linked to the cell [131]. (c) Computed breast stroke optimized for the feeding efficiency.	124
5-6	(a-f) Vorticity field around a biflagellated swimmer undergoing a breast stroke. (g-l) Vorticity field around a biflagellated swimmer undergoing the undulatory stroke.	125
5-7	Representation of the particle pathlines of material points for two successive strokes of a biflagellates. The swimmer is represented in its geometry and location at the end of the two strokes. Yellow and red marks represent respectively the initial and final position of the particles. Gray lines represent the particle pathlines. (a) Optimal computed breaststroke for feeding efficiency (b) Optimal undulatory stroke for swimming efficiency.	126
6-1	Schematic and notation for a droplet on a superhydrophobic surface.	134
6-2	Schematic of the experimental setup.	134

6-3	(a) Photo of a water droplet (0.5 mm radius) on a superhydrophobic surface seeded with silica tracer particles. The inset shows an SEM image of the surface coated with a carbon nanotube forest. (b) Thermal image of a drop deposited on the heated substrate. (c) Superposition of 20 consecutive snapshots of the water droplet taken at 10ms time intervals.	137
6-4	Characteristic timescales for various sizes of water droplets. The gray shaded region indicates the range of droplet sizes in our experiments. Material parameters correspond to those of water with $\Delta T = 1^\circ\text{C}$. Note that, as all three curves scale linearly with ΔT , changing the temperature difference does change the radius at which the curves intersect – rather it rescales the vertical axis.	139
6-5	Analytic solution of the temperature field and corresponding streamlines. The colormap represents the dimensionless analytical temperature field for $\text{Bi} = 800$ and the black arrows represent the streamlines of the flow in the centerplane defined by $\varphi = 0$. The analytical solution is computed using $n = 100$ terms in the expansion.	148
6-6	Schematic ray-tracing diagram of the geometrical optics for a spherical liquid droplet.	149
6-7	Analytical and experimental velocity profile, $ \mathbf{u} $. The spatial variable x represents the dimensionless coordinate along the x -axis: $x = 0$ lies at the center of the droplet, $x = 1$ lies at the contact point. The black line represents the analytic velocity profile in the drop for $\text{Bi} = 800$. Different symbols correspond to three sets of data with heat sources of different intensity. Error bars give an estimate of the error in measuring the velocity of a particle by extracting the position of its centroid in successive frames and hence are a reflection of the resolution of the image.	152

6-8	Analytical and experimental streamlines. The colormap represents the analytical streamfunction; black lines represent particular streamlines computed analytically; black squares represent experimentally recorded particle trajectories. The analytical solution is computed using $n = 100$ terms in the expansion.	153
6-9	a) Error $\ T - T^\alpha\ _2$ as a function of α showing the convergence of the sequence T^α to the point heat source solution T . b) Velocity profile $ \mathbf{u} $ along the x -axis for the point heat source solution and for distributed heat source solutions with $\ell/a = 10\%$ and 20%	155
6-10	(a) Effect of increasing Biot number and increasing Péclet number on the velocity along the x -axis. (b) Apparent biot number for which the velocity profile of the numerical solution along the x -axis best fits the experimental data as a function of the Péclet number.	158

List of Tables

3.1	Summary of the parameters optimized in previous work by Becker <i>et al.</i> [10] and in the present study.	48
4.1	Analytical and computed characteristic values of the “saw-tooth” optimal wave.	98
4.2	Extend of data set coverage for mammals.	109
6.1	Summary of heat transfer in various geometries from superhydrophobic surfaces. A few representative studies are listed in each regime.	131
6.2	Characteristic values of relevant physical parameters.	136
6.3	Summary of the experiments	151

Chapter 1

Introduction

1.1 Motivations

The characteristic length scales associated with major technological innovations have decreased dramatically over the past decades, as many fields of engineering are reaching down to the micro and nano scale. Microfluidics, for example, is a prolific research field which holds promise for many applications such as “lab-on-a-chip”-based devices for medical diagnostics, microfluidics for biological assays, tissue engineering or micro-reactors for energy applications. While the advantages of handling such small volumes of fluid are numerous not the least of which being portability, there are inherent physical constraints associated with mixing and transport at the microscale. These new technological challenges are at the center of an intense research effort as described by H. Stone and coworkers [149] and have fostered an increased understanding of fundamental fluid motion and transport processes in the viscously dominated low Reynolds number fluid regime, which governs the hydrodynamics at these scales.

A comparison between the characteristic length scales of biology and man-made devices leads to the observation that recent microfabricated engineering products reside at the same scale as the vast majority of living organisms which are found at the micrometric scale and are able to overcome the physical limitations associated with this scale (see figure 1-1). This observation has initiated a recent research trend at the crossroad between biofluids and microfluids, which presents a unique opportunity to:

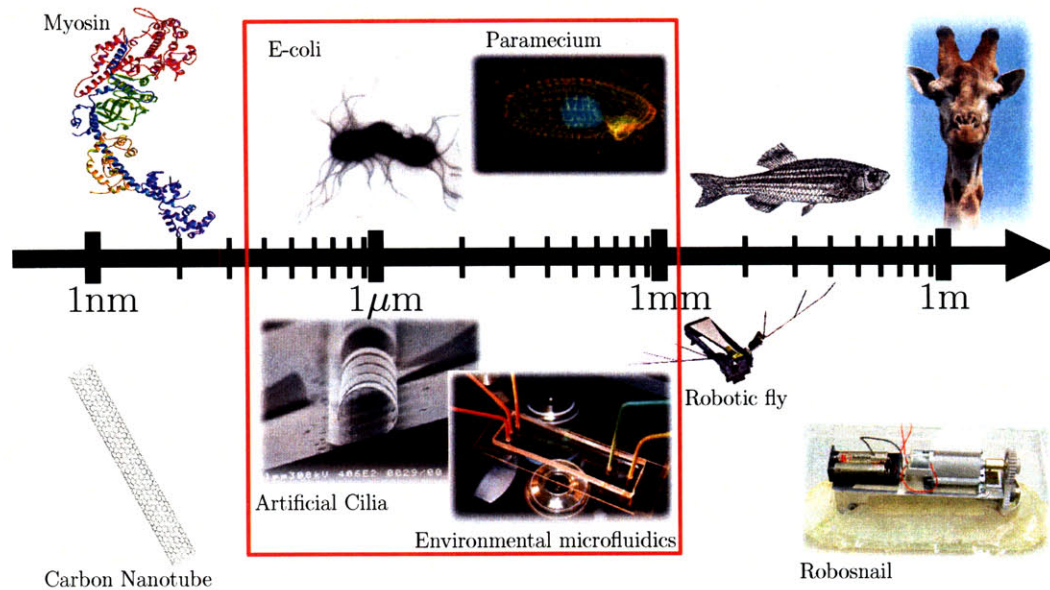


Figure 1-1: Schematic representation of how the length scale of recent technological innovations compare with biological systems. Red box highlights length scales of interest in the work presented herein. Pictures are reproduced from: myosin [63], E-coli [11], paramecium [130], robosnail [28], robotic fly [166], environmental microfluidics [148], artificial cilia [50]

(1) find inspiration in biological micro-organisms to improve micron scale technology and (2) to use engineered micro-devices to better understand locomotion, transport and interactions of micro-organisms with their surrounding environment. Both approaches have been followed recently. Experimental investigations have initiated the use of biologically inspired microfluidic devices to induce: motion via biomimetic micro-pumps [4], transport via bacterial carpets [47] and mixing via biologically inspired artificial cilia [50,90] (see figure 1-1). In return, microfluidic devices have been used to investigate the locomotive response of micro-organisms to mechanical shear in the flow [110,148] (see figure 1-1).

In this thesis we consider several problems which are similar in spirit as they consider motion at low Reynolds numbers at the boundary between biofluids and microfluids. We first investigate locomotion of different flagellated organisms through numerical simulations and optimization. In this study, we seek to rationalize and identify the physical driving forces behind the diversity in stroke patterns observed

experimentally in flagellated microorganisms and the implications regarding locomotion and nutrient uptake. In parallel, we seek to determine efficient beating patterns for the future design of microfabricated swimmers. We also consider systems involving non-biological soft matter and examine the mechanical properties of liquid droplets interacting with recently developed carbon nanotube based superhydrophobic substrates. Our interest is in exploring self-sustained regular convective patterns and heat transfer within the liquid, which have technological implications in mixing and transport of microfluids and could also be used as original microbiological assays.

A thorough presentation of all the motivations behind the study of these different systems is beyond the intentions of this general introductory chapter. The detailed background for each of these studies is further described in subsequent chapters of this thesis.

1.2 Outline and contributions

Chapter 2 through chapter 5 represent the first part of the work related to the biolocomotion of different micro-swimmers. Here we study the deformation and stroke patterns of these swimmers. More specifically we are interested in probing the existence of optimal kinematics with regard to swimming and enhancement of nutrient uptake.

- Chapter 2 presents a general introduction to low Reynolds number swimming and describes the governing hydrodynamics. We develop an original framework for the analysis and systematic investigation of optimal locomotion strategies for deformable slender swimmers in this flow regime. Here we exclusively study the hydrodynamical aspects of locomotion without further consideration of the swimmer’s internal dynamics.
- In chapter 3, the optimization framework is applied to the “three-link” swimmer, which was first introduced and discussed by Nobel prize laureate E.M. Purcell in his famous lecture “Life at low Reynolds number” [121]. For this simple swim-

mer, well-defined optimal stroke kinematics are found for swimming efficiency and distance travelled over one stroke period. The importance of the geometry of the swimmer and the amplitude of the strokes are investigated as well. The efficiency is found to increase with slenderness and approaches the asymptotic optimal value for slendernesses comparable to biological systems. Large amplitude strokes are found to be optimal in the limit of infinitely slender swimmers but to be considerably suboptimal for any realistic value of the slenderness. This simple swimming mechanism provides a benchmark for our modeling approach, which is found to be effective, robust and to rapidly converge toward unique and well-defined optima.

- In chapter 4, we extend our modeling framework to flagellates and consider stroke kinematics of unflagellated swimmers. The optimization procedure is first verified against an analytical solution for optimal single-tail swimmers. We further investigate optimal stroke kinematics for unflagellates. These strokes are always found to be traveling waves propagating along the tail of the swimmer and closely resemble stroke patterns exhibited by biological unflagellated organisms. The question of optimal geometries and morphologies for swimmers is also addressed. We first examine the influence of the head shape on optimality and highlight the positive impact of the head drag anisotropy on optimal swimming. We also discuss the existence of an optimal tail to head length ratio and find a simple morphological criterion which proves to be relevant in the context of sperm morphometry across a large sample of mammalian species.
- Chapter 5 presents a study of a more complex swimmer. The methodology developed in chapters 3 and 4 is generalized to adequately model multiple flagella and is applied to biflagellates. In this case, optimal stroke patterns are compared to experimental observations of green algae *chlamydomonas*, whose strokes have been extensively recorded using high-speed cinematography [131–135]. The optimality of stroke kinematics is discussed in relation to the question of transport and enhancement of nutrient uptake by laminar mixing at the micron scale.

Chlamydomonas primarily exhibits two strokes which are different in structure: the undulatory stroke and the breaststroke which resembles the effective-recovery stroke undergone by cilia. The optimization procedure converges to both the undulatory stroke and the breaststroke, which are found to be local hydrodynamic optima for swimming and feeding respectively. The computation of the vorticity field and the particle pathlines around the swimmer demonstrate enhanced mixing and nutrient flux toward the organism for the breaststroke compared to the undulatory stroke. An important observation from our investigation of both unflagellates and biflagellates is that all biologically observed stroke patterns are found to be hydrodynamical optima, with no further consideration of the internal dynamics of the swimmer. This fact emphasizes the crucial role of the hydrodynamics in the internal self-organization of the flagellum.

The second part of this work also investigates questions related to transport and mixing at the micron scale but in the context of a non-biological system. In this case, we focus our attention on free surface flows, convective transport and heat exchange inside micro-droplets.

- In chapter 6, we report experimental observations of stable axisymmetric convection rolls inside small droplets of water sitting on super-hydrophobic substrates. These stable and regular convective structures appear when the temperature of the substrate is raised by means of a controlled heating plate. We develop a scaling analysis, which strongly suggests that the convection is due to a thermocapillary Marangoni effect at the surface of the droplet, which is in agreement with our experimental observations. An analytical solution is derived for the heat problem as well as for the velocity problem by assuming diffusion dominated heat transfer in the droplet and a point heat source at the contact point between the droplet and the hydrophobic surface. This solution agrees with the data collected experimentally. The effect of finite heat advection as well as the validity of the point heat source assumption are further explored

numerically.

- Chapter 7 presents a brief summary of the thesis as well as suggestions for future work.

Chapter 2

Low Reynolds number locomotion

2.1 Previous work on micro-swimming

Since the early 1950's, the question of locomotion in the inertialess fluid regime has been of great interest to many fluid dynamicists. At first glance, the question appears paradoxical: how can an organism generate propulsion when momentum and inertia are neglected? Early work by G.I. Taylor demonstrated analytically that net propulsion could be induced using purely viscous stresses by the action of a wave of lateral displacement propagating along a sheet [154], as well as by a spiral wave propagating along a cylindrical tail [155]. In these cases, Stokes equations were solved on the entire domain, and no slip boundary conditions were applied on the waving body.

In 1953, G.J. Hancock first introduced the use of fundamental solutions (or singularities) in flagellar hydrodynamics [69]. Using a distribution of singularities along the centerline of a cylindrical rod, he deduced the propulsion velocity and swimming efficiency of an undulating slender rod. This method conveniently models flagellar hydrodynamics as it substitutes the differential Stokes equations in the entire fluid domain by an integral equation over the boundary of the swimmer. This pioneering work introduced the use of singularity methods or integral methods in flagellar hydrodynamics and more generally in slenderbody theory [8,41,83,89,157]. One of the main outcomes of this body of work was the introduction by Gray and Hancock [64,65] of resistive force theory to model the hydrodynamics around a slender rod. This simple

method only retains the leading order term in slenderbody theory and linearly relates via resistive coefficients the local drag force to the local velocity at the centerline of the rod. Resistive force theory remains today the method of choice for first order approximations of flagellar hydrodynamics.

J. Lighthill has also made enormous contributions to the field of Flagellar hydrodynamics and more generally to microbiological fluid mechanics. He generalized Hancock’s use of singularities [100, 102] and analytically solved several problems related to propulsion at low Reynolds numbers [100, 101]. His close collaboration with biologists and zoologists enabled him to identify biologically relevant questions and new research topics in biofluidynamics and to address them rigorously as a fluid dynamicist [16, 100]. An extensive review of the early prolific work on low Reynolds number swimming can be found in [17].

Although his work in the field is relatively limited, E.M. Purcell brought the topic to the forefront of fluid mechanics by posing the problem of low Reynolds number locomotion as an open and famous question to the scientific community. His highly cited paper *Life at Low Reynolds Number* [121, 122], transcribed from his famous lecture, presents a clear picture of the inertialess regime by introducing what is now known as the “scallop theorem”. This “theorem” will be explained in more detail in a later discussion. Also famous is the example, given in this lecture of a simple swimmer, the three-link swimmer, which exhibits non-reciprocal swimming patterns and thus generates net propulsion. In his presentation, the question of the swimming direction of the three-link swimmer remained open. This question has been addressed in a recent study by Becker *et al.* [10], in which the direction of swimming was identified.

From the simple observation that, in the inertialess regime, the net motion of a swimmer only depends on the geometrical deformations of its body, it becomes intuitive that time should not be a relevant parameter. This means that, in principle, one should be able to reformulate low Reynolds number locomotion as a geometrical problem rather than a dynamical problem. This path has been investigated by Shapere and Wilczek [142–144] using Gauge field theory. This geometrical approach to low Reynolds number swimming is particularly useful when looking at optimal ef-

iciency of various stoke patterns. In their study, Shapere and Wilczek looked at the motion generated by infinitesimal deformations of a sphere. Avron *et al.* investigated optimal swimming within a class of two-dimensional swimmers using conformal mapping [5]. Other studies have approached swimming of micro-organisms theoretically using string theory [87, 88]. Using such geometrical approaches, new low Reynolds number swimmers have been imagined and analyzed [6, 112].

More recently, flagellar hydrodynamics has been approached from a dynamical fluid-structure interaction point of view. In this case, the flagella no longer has a prescribed motion, rather it is considered to be an elastic filament interacting with the surrounding Stoke's flow, which is modeled using resistance coefficients. Wiggins *et al.* have studied propulsion of a passive elastic filament, which is set into oscillatory motion at one end of the filament [98, 164, 169]. Other studies have modeled elastic filaments subject to internally generated bending forces [26, 56, 94, 104], which are known to occur in the case of axonemal flagellar beating of spermatozoa for example. It has been suggested that mathematically flagellar beating could be a self-organized phenomenon, generated by internally oscillating stresses [26].

This problem has also been approached from a purely numerical point of view. Extending the immersed boundary method [117] to numerically compute the coupled interactions between a Stokes flow and an elastic boundary [38, 39, 55], Cortez *et al.* developed a method to simulate fluid structure interactions of an elastic filament in the inertialess regime [37]. This computational tool has been used to investigate biological hypotheses concerning internal generation of stress within the flagellum.

Finally, recent technological breakthroughs in microfabrication have opened doors to potential applications of microswimming to targeted drug delivery or minimally invasive surgery. Such critical problems require the design and manufacturing of swimming microrobots. To this end, an increasing number of experimental swimmers have been designed, built and tested. Magnetically driven spiral shaped micro-machines have been reported to self-propel effectively under a large range of Reynolds numbers. In this case, the entire swimming trajectory was successfully controlled throughout the entire motion of the swimmer [79, 80, 114, 167]. The feasibility of propelling a

micro-machine via oscillation of a passive elastic tail has also been investigated, and such swimmers have been build [151]. A magnetically-driven microscopic swimmer made of colloidal magnetic particles linked by DNA and attached to a red blood cell has also been shown to self-propel in the inertialess regime [52].

2.2 Motivations

The vast majority of living organisms are found in an astonishing diversity at micrometric scales. This thesis was originally inspired by microscopic observations of a variety of such organisms. A glimpse of this diversity is given in an illustration drawn by J. Lighthill of different groups of microorganisms presented in the 1975 John Von Neumann lecture [100]. This drawing is reproduced in figure 2-1. Despite many obvious differences, these organisms share a number of common traits. First, they are all unicellular and hence relatively simple systems to model from a hydrodynamical standpoint. Secondly, they all seem to exhibit some degree of locomotion. This implies that motility is a dominant aspect of life at micro-scales, which is quite remarkable as it may seem at first glance that, at these small scales, transport should be dominated by diffusion. Here we ask two questions that are key to this study of microswimming: *How do these organisms propel themselves? Why and how well do these organisms propel themselves?* In an engineering sense these questions translate to : *How can we model motility of micro-organisms? Can we learn anything from optimizing their motile functionality?*

One last dominant trait shared by many microorganisms, which can be readily seen in J. Lighthill's drawing, is the prevalence of flagella as motility appendages. In figure 2-1, organisms with flagella are represented inside the circle in the center of the drawing, which indicates that flagellates are related to many different biological groups. Among eukaryotes, all flagella have the same structure called the eukaryotic flagellum or axoneme, a structure that is extremely well preserved across the eukaryotic domain. This same structure is essentially used to propel eukaryotic unicellular organisms and sperm cells or to expel mucus in the human lungs (cilia) by beating col-

SOME MICROORGANISMS WITH FLAGELLA (CENTRAL CIRCLE) AND RELATED ORGANISMS

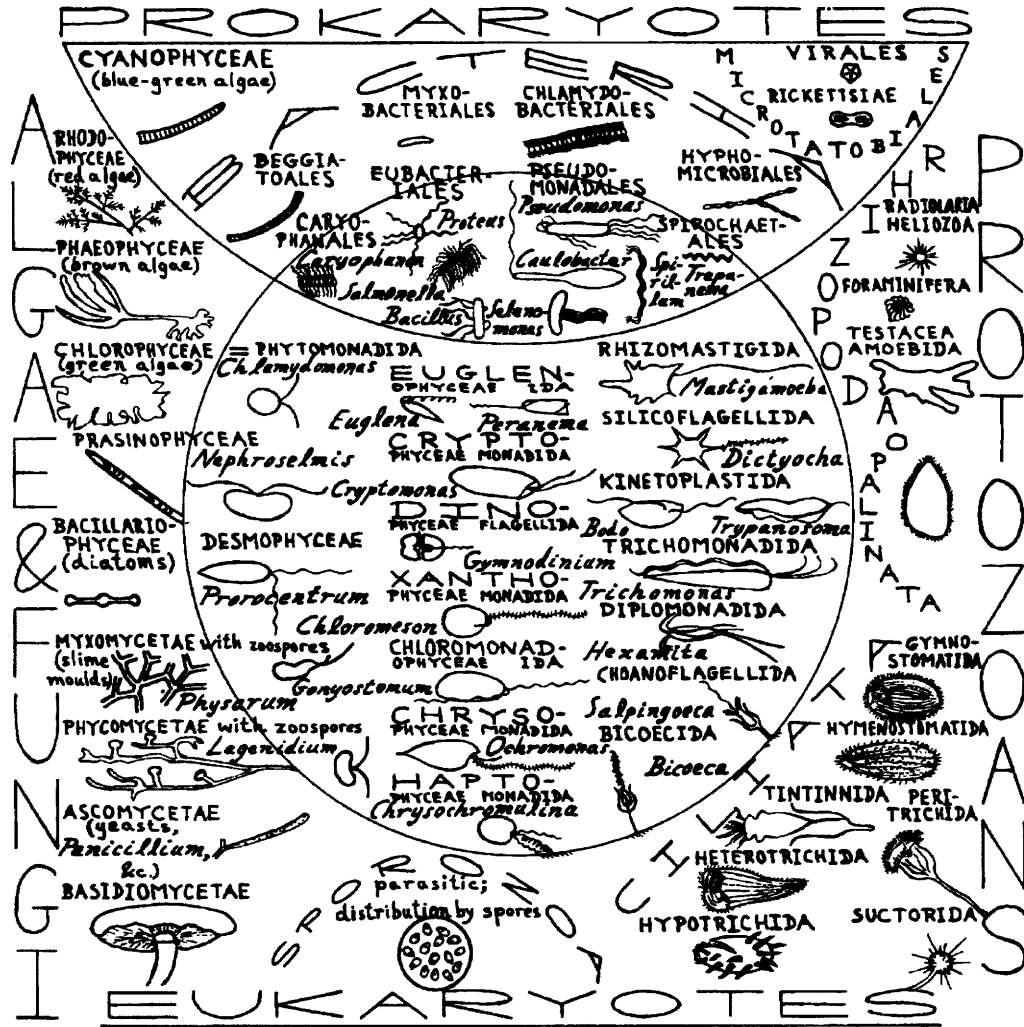


Figure 2-1: "A general overview of microorganisms with flagella and related organisms". (Reproduced from [100])

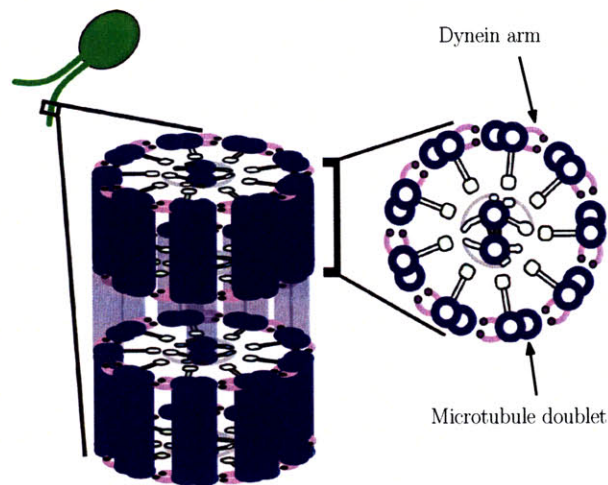


Figure 2-2: “The modular structure of a flagellum”. (Reproduced from [162])

lectively. The eukaryotic flagellum has an internal “9+2” structure [53,77], comprised of a bundle of nine rigid microtubule doublets arranged around two central microtubules (see figure 2-2). Dynein arms, which are ATPase molecular motors, extend from each one of the nine microtubule doublets to the neighboring doublet and induce sliding through ATP-hydrolysis. This mechanism results in bending and can be induced at any location along the flagellum to actively alter its shape. In fact, eukaryotic flagella have been observed to beat in significantly different ways: sperm exhibit traveling waves that propagate down the flagellum, cilia exhibit effective-recovery strokes and the green algae, *chlamydomonas*, exhibits both previously mentioned strokes.

These final observations motivated this study of flagellar locomotion, and in particular, of the stroke patterns of flagellated organisms. Since it is theoretically possible for organisms to alter and possibly control the waveform along the flagellum, it is of interest to investigate whether optimal stroke patterns exist. Hence our two questions become: *How can we model motility of flagellated swimmers? What can we learn from optimizing the stroke pattern of the flagellum?* In the following study, these questions will be addressed by looking only at the hydrodynamics and not the internal dynamics of the swimmer. In chapters 3, 4 and 5 we will investigate three different systems: the simple three link swimmer, uniflagellates and biflagellates.

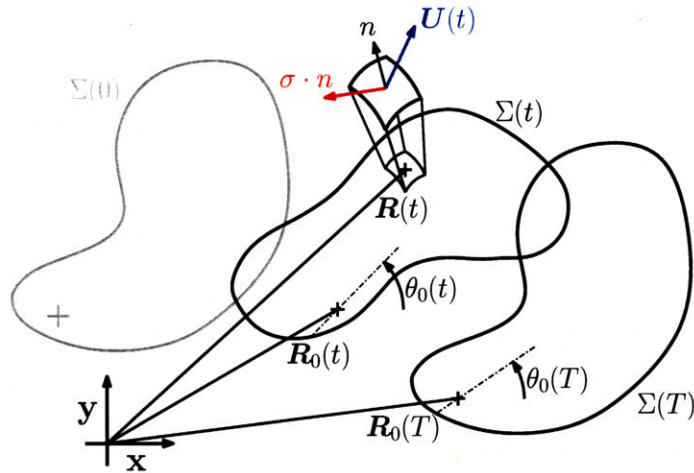


Figure 2-3: Swimmer undergoing one stroke or periodic deformation of period T . The surface is represented at time 0, t and T , which relevant notations.

2.3 Modeling approach

This section describes some general notations and aspects of the modeling approach, which are common to all three studies described in chapters 3, 4 and 5.

2.3.1 Representation of a swimming organism

The focus of this study is on optimality of stroke patterns from a hydrodynamical point of view. Hence, the internal dynamics within the swimmer are not modeled and the swimmer can be simply seen as a deformable surface immersed in a viscous flow, whose kinematics and deformations are entirely prescribed. Let $\Sigma(t)$ represent the surface of the swimmer at time t , and $\mathbf{R}(t)$ and $\mathbf{U}(t)$ be the position and velocity at a given material point on the surface. For two dimensional planar motions, the location of the swimmer at each time t is defined by the position vector of a reference material point $\mathbf{R}_0(t)$ attached to the swimmer and a reference orientation $\theta_0(t)$. Figure 2-3 represents a swimmer undergoing a surface deformation and the related translation and rotation. Because the system under consideration is unsteady, all variables are expected to depend on time t . To simplify the notation, time dependency of all variables will no longer appear explicitly, unless it is required to avoid confusion.

In order to swim continuously, an organism undergoes a “stroke”, which is a periodic deformation of its body-shape. Here, we will explicitly impose the kinematics, i.e. the geometry of the periodic deformation of the surface (or stroke pattern). Over the course of one stroke, the swimmer—starting at $t = 0$ from an original surface geometry—continuously deforms. When at $t = T$ it returns to its initial surface geometry at the end of the stroke, it may no longer be at its original location, in which case there has been a net displacement. Hence, the velocity field \mathbf{U} along the surface Σ of the swimmer can be written at all times as the superposition of a rigid body motion \mathbf{U}^{rig} and a deformation field \mathbf{U}^{def} . The velocity field due to the rigid body motion at a given point \mathbf{R} on the surface Σ reflects the net translation \mathbf{U}_0 and rotation Ω_0 of the swimmer:

$$\mathbf{U}_0 = \dot{\mathbf{R}}_0, \quad \Omega_0 = \dot{\theta}_0, \quad \mathbf{U}^{\text{rig}} = \mathbf{U}_0 + \Omega_0 \hat{\mathbf{z}} \times (\mathbf{R} - \mathbf{R}_0), \quad (2.1)$$

where the dot stands for a time derivative.

The rigid body motion, \mathbf{U}^{rig} , is unknown and must be computed using the appropriate hydrodynamics. The deformation field \mathbf{U}^{def} describes the surface deformation of the swimmer (or stroke pattern) and is prescribed.

2.3.2 Low Reynolds number hydrodynamics

The equations governing the dynamics of newtonian fluids are the Navier–Stokes equations, which for an incompressible flow can be written as

$$\rho \left(\frac{\partial \mathbf{u}}{\partial t} + \mathbf{u} \cdot \nabla \mathbf{u} \right) = -\nabla p + \mu \nabla^2 \mathbf{u}, \quad (2.2)$$

$$\nabla \cdot \mathbf{u} = 0, \quad (2.3)$$

where ρ is the density of the fluid, μ the dynamic viscosity, \mathbf{u} the velocity field and p the pressure field. For a given length scale L and characteristic velocity U , the equations can be made dimensionless. In this case, the only remaining non-dimensional parameter is the Reynolds number $\mathcal{R}e = \frac{\rho L U}{\mu}$, which represents the

ratio of inertial to viscous forces.

When considering microswimming, the characteristic length-scale is in general at most $L \sim 100 \mu\text{m}$ and the characteristic velocity of the swimmer is typically no more than $U \sim 100 \mu\text{m}$. Hence the Reynolds number \mathcal{Re} for microorganisms swimming in water is at most on the order of $\mathcal{Re} \sim 10^{-2}$ and inertia can be neglected. In this regime, the Navier–Stokes equations reduce to Stokes equations

$$\begin{aligned} -\nabla p + \mu \nabla^2 \mathbf{u} &= \mathbf{0} , \\ \nabla \cdot \mathbf{u} &= 0 . \end{aligned} \tag{2.4}$$

Two important properties of Stokes equations are worth mentioning here: the equations are both linear and time reversible. The linearity of the governing equations has important implications in the methods that will be used to solve the hydrodynamics around our microswimmers. Time reversibility leads to the so-called “scallop theorem” [121], which can be understood as follow. Recall that in order to swim, an organism implements periodic deformations of its body-shape. A reciprocal motion is one type of periodic deformation, in which the organism deforms to a new shape and then returns to its original shape by going through the same sequence of deformations but time reversed. Such reciprocal motion is exhibited by an idealized scallop, which can only open and close its shell. The “scallop theorem” simply states that such reciprocal motion does not generate any net translation. A detailed discussion and rigorous proof of the “scallop theorem” can be found in [31].

It follows from this remark that low Reynolds number swimmers need to undergo a non-reciprocal deformation or stroke pattern in order to generate propulsion. One such stroke is exhibited by the three-link swimmer and will be discussed in chapter 3.

2.3.3 Dynamics of the swimmer

Equilibrium equations

Let $(\boldsymbol{\sigma} \cdot \mathbf{n})$ be the hydrodynamic stress acting on the surface Σ at a given point. Since the density of the swimmer is roughly the same as that of water, a dimensional analysis identical to the one in section 2.3.2 but considering the inertia of the swimmer instead enables us to neglect its own inertia compared to the viscous stress acting on its surface. Hence at any time during the stroke, conservation of momentum and angular momentum for the swimmer reduces to the equilibrium equations

$$\begin{aligned} \iint_{\Sigma} (\boldsymbol{\sigma} \cdot \mathbf{n}) \, d\Sigma &= \mathbf{0} \, , \\ \iint_{\Sigma} \mathbf{R} \times (\boldsymbol{\sigma} \cdot \mathbf{n}) \, d\Sigma &= \mathbf{0} \, . \end{aligned} \tag{2.5}$$

Equations of motion

Because of the linearity of Stokes equations, the hydrodynamic stress $(\boldsymbol{\sigma} \cdot \mathbf{n})$ acting on the surface Σ depends linearly on the velocity distribution \mathbf{U} at the surface Σ . This linear relationship can be readily seen in the integral form of Stokes equations, which relates stress and velocity distributions at the surface through a linear integral equation (see [1] for example). Hence the integrals in the equilibrium equations (2.5) can be viewed linear as functions of the velocity distribution \mathbf{U} and can be symbolically written as $\mathcal{L}_{\Sigma}(\mathbf{U}) = \mathbf{0}$. The subscript Σ is a reminder that the integrals in equations (2.5) are taken over the surface Σ , which implies that the linear operator \mathcal{L}_{Σ} depends on the instantaneous shape of the swimmer.

Recall from section 2.3.1 that the velocity \mathbf{U} at the surface of the swimmer can be decomposed into the sum of a prescribed deformation \mathbf{U}^{def} and an unknown rigid body motion \mathbf{U}^{rig} . Substituting this decomposition into the equilibrium equations yields a system of equations $\mathcal{L}_{\Sigma}(\mathbf{U}^{\text{rig}} + \mathbf{U}^{\text{def}}) = \mathbf{0}$, which can be inverted, solved for the rigid body motion components (\mathbf{U}_0, Ω_0) and integrated in time to find the net displacement of the swimmer.

Time integration

The equations of motion discussed in section 2.3.3 take the form of a system of coupled first order nonlinear ODEs for \mathbf{R}_0 and θ_0 . These equations can be written as

$$\begin{aligned} \dot{\mathbf{r}}_0(t) &= f(\mathbf{r}_0(t), \mathbf{c}(t)) , \\ \mathbf{r}_0(0) &\text{ is given ,} \end{aligned} \tag{2.6}$$

where $\mathbf{r}_0 = (\mathbf{R}_0, \theta_0)$ represents the instantaneous position of the swimmer, with given initial conditions $\mathbf{r}_0(0)$ and $\mathbf{c}(t)$ is a prescribed vector of control (or decision) functions which parameterizes the kinematics. This system is integrated in time explicitly with a fifth order embedded Runge–Kutta algorithm using the Cash–Karp parameters. The algorithm allows for accurate and efficient computation by adapting the size of the time step to reach a desired level of accuracy. The same algorithm is used in chapters 3, 4 and 5. More detail on the time integration algorithm can be found in [120].

Rate of work

A quantitative measure, which is essential to this discussion on optimal low Reynolds number locomotion, is the energy expense of the swimmer. Intuitively, one might guess that this energy expense should be minimized when investigating efficient swimming. In this study, which is exclusively concerned with the hydrodynamics of swimming, a measure of the energy expense is given by the total amount of viscous dissipation in the fluid which is equivalent to the work exerted by the swimmer against the viscous fluid.

In the following, we consider a stroke pattern of period T . As the organism swims, the stroke can be represented by a continuous sequence of surface geometries, which we denote by $\Sigma(q)$ for $q \in [0 T]$. The vector $\mathbf{R}(q)$ represents the position vector of a material point on the surface during the stroke. It is important to note that this specific sequence of geometrical configurations can be implemented at different rates as defined by a time dependent parameterization function $q(t)$, with $q(0) = 0$

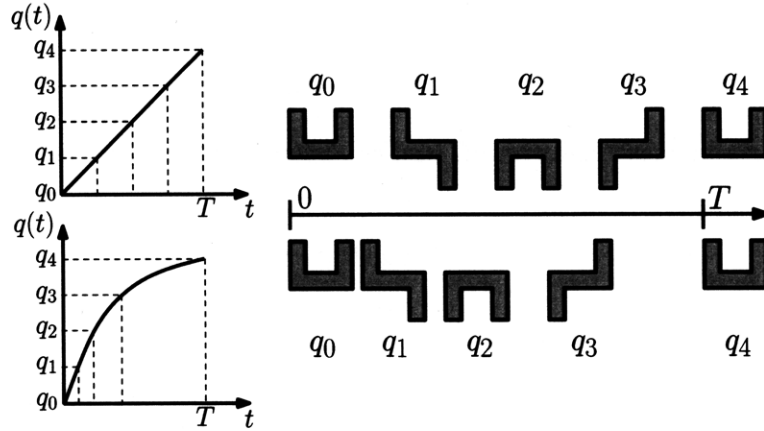


Figure 2-4: Schematic representation of a given stroke undergone at different time parameterization functions $q(t)$.

and $q(T) = T$. A schematic illustration of a given deformation sequence undergone at different time parametrizations $q(t)$ can be found in figure 2-4. For a given parameterization, the surface at time t is given by $\Sigma(q(t))$, while $\mathbf{R}(q(t))$ represents the position vector of a material point on the surface at time t . This is a direct consequence of the properties of Stokes equations mentioned in section 2.3.2. In this section, we will show that for a given sequence of geometrical shapes $\Sigma(q)$, the time parameterization $q(t)$, which minimizes the total mechanical work exerted by the swimmer against the viscous fluid, is such that the rate of work is constant throughout the stroke. This discussion can also be found in the appendix of [10].

For a given time parameterization q , the rate of work at time t can be written

$$\Phi = \iint_{\Sigma(q(t))} (\boldsymbol{\sigma} \cdot \mathbf{n}) \cdot \mathbf{U} d\Sigma . \quad (2.7)$$

At a given point on the surface, the velocity can be expressed as

$$\mathbf{U} = \frac{d\mathbf{R}(q(t))}{dt} = \dot{q}(t) \frac{d\mathbf{R}(q(t))}{dq} , \quad (2.8)$$

which is the product of $\dot{q}(t)$ times a function of q only. Because of the linear dependence of the stress acting at the surface on the velocity distribution \mathbf{U} (which we discussed in section 2.3.3), the stress $(\boldsymbol{\sigma} \cdot \mathbf{n})$ is also the product of $\dot{q}(t)$ times a

function of q only. Hence for a given stroke, the rate of work can be written as

$$\Phi = [\dot{q}(t)F(q(t))]^2, \quad (2.9)$$

and the total work exerted on the viscous fluid during one stroke can be written as

$$W = \int_0^T [\dot{q}(t)F(q(t))]^2 dt. \quad (2.10)$$

It should be noted here that the function F depends of course on the specific stroke under consideration.

A lower bound for the total work W can be readily obtained from Schwartz's inequality

$$\begin{aligned} W &= \frac{1}{T} \int_0^T [\dot{q}(t)F(q(t))]^2 dt \cdot \int_0^T 1^2 dt \\ &\geq \frac{1}{T} \left[\int_0^T \dot{q}(t)F(q(t)) dt \right]^2 = \frac{1}{T} \left[\int_0^T F(q) dq \right]^2. \end{aligned} \quad (2.11)$$

Schwartz's inequality becomes an equality if and only if the function $\dot{q}(t)F(q(t))$ and the function $f = 1$ are linearly proportional, which simply implies that the rate of work $\Phi = [\dot{q}(t)F(q(t))]^2$ is constant.

Hence for a given stroke, the mechanical work W reaches an absolute minimum value which is uniquely defined and equal to $\frac{1}{T} \left[\int_0^T F(q) dq \right]^2$ when the time parameterization is such that the rate of work Φ is constant. This proves that the search for optimal strokes at low Reynolds number is essentially a geometrical problem with the kinematics of each stroke patterns being associated with a uniquely determined minimal mechanical work.

This allows one to reduce the problem of finding optimal strokes to finding optimal stroke kinematics, i.e.: optimal sequences of surface shapes. It bears emphasis that even if the particular time parameterization which minimizes the work is unknown,

the minimal work can still be computed as:

$$W_{\min} = \frac{1}{T} \left[\int_0^T F(q) dq \right]^2 = \frac{1}{T} \left[\int_0^T \sqrt{\Phi(t)} dt \right]^2. \quad (2.12)$$

In the following, all discussion about the work exerted by the swimmer on the surrounding fluid will always implicitly refer to the minimal work W_{\min} given by equation (2.12).

2.3.4 Locomotion optimization

Objective function and efficiency

As mentioned earlier, the present work investigates optimal stroke patterns. To this end, we need to define an objective function, which measures how “good” a given stroke is. This objective function will depend on the specifics of the problem under consideration and will be presented in more detail for each problem individually in the coming chapters.

Nevertheless, a few general comments regarding the objective function are in order here. One possible measure of the “effectiveness” of a given stroke is an *efficiency*, which is a scalar. Here, the term *efficiency* is loosely defined as the fraction of the total energy expense effectively used towards a given objective, such as moving forwards or feeding. One such efficiency is extensively used in the following chapters and will often be referred to as the swimming efficiency.

In the following, we define the swimming efficiency and discuss its relevance with respect to low Reynolds number swimming. Consider a stroke of period T during which the organism swims over a distance ℓ_0 at an average speed of $U_0 = \ell_0/T$. For this particular stroke, the swimming efficiency is defined as the ratio of the work required to move an equivalent swimmer over the distance ℓ_0 at the average speed U_0 , to the total work exerted by the swimmer against viscosity

$$\mathcal{E} = \frac{\alpha U_0 \ell_0}{W_{\min}}. \quad (2.13)$$

Here W_{\min} is the minimal work as given by equation (2.12) and α is the drag coefficient of the equivalent swimmer, which will be specified in later chapters. The quantity αU_0 can be interpreted as the force required to move the equivalent swimmer at velocity U_0 . This definition for the swimming efficiency is consistent with previous work [10, 69]. While in general, the swimming efficiency can be computed for any strokes, we are usually only interested in those strokes resulting in net translation only. Recall from section 2.3.1 that at the end of each stroke, the deformation of the body induces a net displacement, which is composed of both a translation of vector $\mathbf{R}_0(T) - \mathbf{R}_0(0)$ and a rotation of angle $\Delta\theta = \theta_0(T) - \theta_0(0)$. While the change in position corresponds to the distance traveled ℓ_0 and should be maximized, the change in orientation should remain as small as possible. If the net rotation over one stroke is non-zero, the swimmer will move along a circle as it undergoes a series of stroke and will eventually get back to its original location, resulting in no net translation. In the following chapters, the stroke kinematics with non-zero net rotations are avoided as they are by no means optimal for locomotion. It bears emphasis that for all acceptable stroke kinematics with zero net rotation, the efficiency \mathcal{E} of the stroke will have the same value whether it is computed over one, two or n stroke periods. This is because for these strokes, the distance traveled over n strokes is $n\ell_0$ and the minimal work is nW_{\min} , while U_0 is constant.

There are a number of interesting properties of this swimming efficiency due to the particular structure of Stokes equations (2.4). Assuming all swimmers are immersed in the same Newtonian fluid of dynamic viscosity μ , Stokes equations (2.4) can be made nondimensional by fixing a length scale and a time scale. The solution to the nondimensional Stokes equations for the velocity and pressure fields does not depend on any nondimensional parameters. This implies that for a given stroke the nondimensional distance traveled $\tilde{\ell}_0$, average speed \tilde{U}_0 and minimal work \tilde{W}_{\min} do not depend on any nondimensional parameters either. Since the efficiency \mathcal{E} is itself nondimensional, we can conclude that \mathcal{E} depends neither on the chosen length scale nor on the time scale and thus characterizes the kinematics of the stroke itself. A direct consequence is that a swimmer undergoing a given stroke is exactly equivalent

(i.e. same U_0 , ℓ_0 , W_{\min} and \mathcal{E}) to a similar swimmer whose dimensions have been scaled down by a factor of two that executes the same stroke twice as fast.

Finally, it bears emphasis that \mathcal{E} is in fact a measure of both how fast and how “energy efficient” a particular stroke is. In order to demonstrate this point, first suppose we want to find the stroke which will allow the swimmer to go the fastest. A naive approach would be to decrease arbitrarily the period of the stroke T to zero or to increase the characteristic size of the swimmer to infinity, in which case the average speed of the swimmer $U_0 = \ell_0/T$ becomes virtually infinite, regardless of the kinematics of the stroke. This infinite average speed is of course reached at the cost of an infinite energy expense W_{\min} and is in no way representative of an optimal swimming strategy. A more relevant way of investigating fast swimmers is to compare different strokes performed by the same swimmer, for which the energy cost is the same. This is equivalent to assuming that the swimmer always carries the same fixed (and limited) energy supply and to then find the stroke which maximizes the distance over which the swimmer can travel during a given period of time. In this case, for all strokes α is fixed by the geometry of the swimmer, W_{\min} is the fixed amount of energy carried by the swimmer, T is the fixed time for which the swimmer is allowed to travel and hence maximizing the traveled distance or the average swimming speed is equivalent to maximizing the swimming efficiency \mathcal{E} .

Similarly, suppose we now want to find the stroke which is most energy efficient, meaning that the work done against viscous forces W_{\min} is the smallest. Again, a simplistic approach would be to increase the period of the stroke T or to reduce the characteristic size of the swimmer to zero. This would make the total work W_{\min} done by the swimmer go to zero, however the average traveling speed U_0 would also go to zero. The true problem here is to compare the energy cost of strokes performed by the same swimmer, which swims at a prescribed average speed. For all strokes, α is again fixed by the geometry of the swimmer, the average speed U_0 is prescribed, and ℓ_0 is the fixed distance over which the swimmer is allowed to travel. In this case, minimizing the energy cost and hence the total work exerted by the swimmer on the flow is again equivalent to maximizing the swimming efficiency \mathcal{E} .

The use of the term swimming “efficiency” may be confusing as it may seem to only refer to the energy cost minimization problem. However as we have seen here the value of \mathcal{E} measures both how fast and how energy efficient a given stroke is. Hence it represents the adequacy of a given stroke for swimming and will be used as the objective function in our optimization procedure.

Optimization approach

So far, we have presented general aspects of the models used to represent a swimming microorganism. The input of this model is the full description of the stroke kinematics or periodic deformation of the swimmer’s surface. Given this, our model for the dynamics of the swimmer allows us to compute and integrate over one stroke period the motion of the swimmer as well as the rate of work exerted against the fluid. Finally the efficiency can be computed, using equation (2.13).

The form of the equations of motion (2.6) is characteristic of a continuous-time deterministic dynamical system, where the position of the reference point $\mathbf{r}_0(t)$ is the state of the system and the vector of control functions $\mathbf{c}(t)$ parameterizes the deformation of the swimmer. This system is deterministic because the state of the system as well as the control (or decision) function are only required at time t in order to predict the exact evolution of the system. Here, we are interested in finding strokes or control trajectories, determined by the control function $\mathbf{c}(t)$, which maximize the efficiency. This problem bears close similarities with cost minimization problems in optimal control theory [13], which can be derived from Pontryagin’s minimum principle. However in optimal control, the objective function is a cost functional which takes the form of the time integral of an additive cost, which is only a function of the current state of the system and the control (or decision) at that time. The focus of the present study is in optimizing efficiencies, which cannot be written as additive cost functions. Optimal control and related methods such as calculus of variation are therefore not best suited to this analysis.

Another approach to this optimization problem is to represent the continuous control functions describing the stroke or deformation of the swimmer by a finite set

of deformation parameters. These deformation parameters form a vector of finite dimension and will be discussed in more detail for each problem individually in the next chapters. Once this parameterization has been established, the input to the model is simply the vector of deformation parameters or variables. The equations of motion can then be integrated over one period by imposing the surface deformation prescribed by the input deformation parameters. Finally, the efficiency is evaluated and given as an output. In this formulation, since the efficiency can be written as a nonlinear function of a finite set of variables, nonlinear programming can be used in order to maximize the efficiency. This nonlinear programming approach has been used throughout this study. It is interesting to note, that this formulation also allows us to optimize simultaneously the stroke itself as well as other geometric parameters characterizing the swimmer.

Optimization algorithm

In the following chapters, the *optimization toolbox* from *MATLAB* is used in order to find optimal stroke patterns. We use the routine *fmincon*, which finds the minimum of a constrained nonlinear multivariable function. A detailed description of the optimization algorithms implemented in the *fmincon* routine is beyond the scope of the present discussion, which is limited to general remarks.

The efficiency is a complex function of the deformation parameters, which involves the integration of the swimmer's motion over the entire trajectory. Hence, no analytical formulation for the derivatives of the efficiency with respect to each deformation parameter could be derived, and the optimization algorithm relies instead on numerical evaluation via finite differences for the computation of all derivatives required by the algorithm.

In our study, *fmincon*, which finds the optimal of a nonlinear function subjected to constraints, implements sequential quadratic programming. Sequential quadratic programming methods are designed to directly solve the Karush–Kuhn–Tucker (KKT) equations, which are a set of necessary condition on the Lagrangian function for the optimality of constrained problems. In this case, the solution to the KKT equa-

tions is found using a quasi-Newton type iterative process, which closely mimics quasi-Newton methods for unconstrained problems. The quasi-Newton method implemented in *fmincon* is the *Broyden–Fletcher–Goldfarb–Shanno* (BFGS) method, which avoids the numerically costly evaluation of second derivatives by accumulating curvature information from previous gradient evaluations. More detail on these algorithms can be found in classical textbooks on nonlinear programming [13].

2.3.5 Summary

In this chapter, we have discussed general aspects of the methods used to model and optimize swimming at low Reynolds numbers. We explained how the equations of motion can be deduced from the prescribed deformation of the surface of the swimming organism and how these equations can be integrated in time numerically to find the displacements of the swimmer. We then presented the use of a scalar quantity – the efficiency – to compare and characterize the optimality of different swimming strategies. Lastly, we discussed nonlinear programming as a method to optimize stroke patterns for low Reynolds number swimming, and briefly described the algorithm used in the following chapters.

In the three next chapters, the specifics of this method will be developed in detail for each of the three different problems. First, the geometry of the swimmer will be described. Then the equation of motions will be derived by solving the hydrodynamics and applying the equilibrium conditions. The spatial discretization of the swimmer allows us to solve for the displacements numerically and will be discussed for each swimmer. We will then develop and give expressions for the relevant efficiencies. Finally, we will describe the representation of a continuous swimming stroke using a finite set of parameters, which is necessary in order to optimize the stroke kinematics using nonlinear programming.

Chapter 3

Optimizing Purcell’s three-link swimmer

3.1 Introduction

In his famous lecture *Life at Low Reynolds Number* [121], E. M. Purcell presented what may be the simplest active tail that can effectively propel itself at low Reynolds numbers – the three-link swimmer. This swimmer can be viewed as a simplified and discretized version of the eukaryotic flagellum made of three slender rods, which can be actively articulated at the two hinges. Unlike the “two-link scallop”, the additional link enables the three-link swimmer to undergo non-reciprocal motion and hence theoretically to swim forward. An experimental three-link swimmer has been designed and its swimming abilities confirmed in a recent study by B. Chan and A.E. Hosoi [161]. Also a helical bacteria, spiroplasmas, has been conjectured to use a three-link-like mechanism to propel itself [12].

In a recent study, Becker *et al.* [10] optimized a discrete and limited set of geometric parameters characterizing the infinitely slender three-link swimmer. They also addressed the question, which remained open at the end of E.M. Purcell’s lecture, as to which direction the three-link swimmer swims. However, as the authors limited their study to geometric designs, the quantitative results given in this work are suboptimal.

	Geometry			Kinematics
	parameter (scalar) opt.			function opt.
	arm length	slenderness	stroke amplitude	stroke pattern
Becker <i>et al.</i> $\mathcal{O}(1/\ln \kappa)$	×		×	
Present study $\mathcal{O}(1/(\ln \kappa)^2)$	×	×	×	×

Table 3.1: Summary of the parameters optimized in previous work by Becker *et al.* [10] and in the present study.

Two key ideas separate the study presented in this chapter from previous work by Becker *et al.* as summarized in Table 3.1. The first is the concept of *kinematic* optimization versus *geometric* optimization. Geometric optimization addresses questions related to the geometric design of biological and mechanical swimming devices. In contrast, kinematic optimization confronts the question: “Given a swimmer with a particular geometry, what is the optimal actuation strategy?” As an analogy, consider an olympic swimmer. The geometry of the swimmer is fixed but he is physically able to employ any number of strokes: freestyle, breaststroke, butterfly, etc. Kinematic optimization seeks the “best” sequence among this infinite array of possible stroke patterns. The second significant difference between the present study and previous work is that optimizing kinematics requires a functional rather than a parametric variation. Unlike the geometric parameters considered in earlier studies, the stroke shape and sequence cannot be described by a single scalar, rather it must be represented by a continuous function (see Figure 3-3).

In this chapter, the methodology outlined in chapter 2 is applied to one of the simplest, and historical, figures of low Reynolds number studies: the three-link swimmer. This investigation also provides a benchmark for the method developed in this thesis and may give some insight into what to expect for more complex swimmers. In the following, we extend the model used by Becker *et al.* to include stroke kinematics, hydrodynamic interactions between the different links and effects of finite slenderness, to provide a complete description of the three-link swimmer. Both the kinematics of the stroke and the geometry of the swimmer are fully optimized [152]. We also discuss

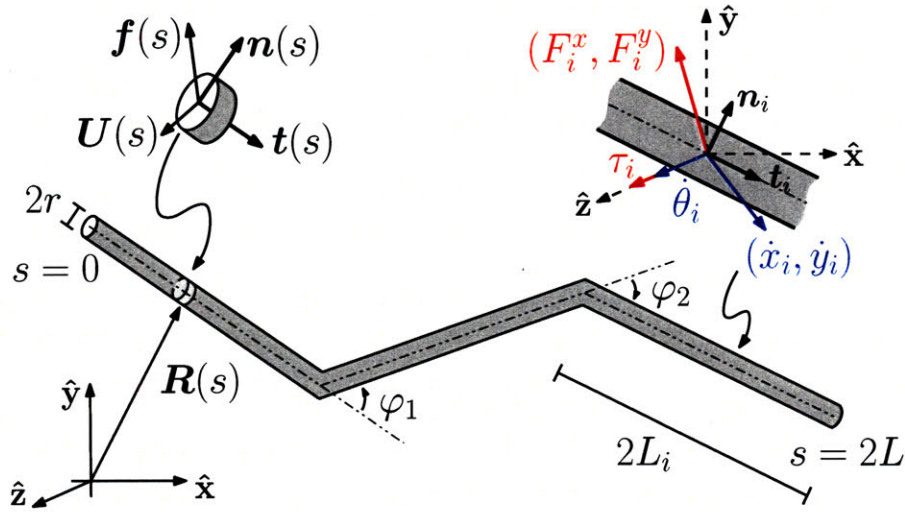


Figure 3-1: Schematic of the swimmer. The slice and corresponding notation on the left refer to the local velocity, tangent vector and drag force per unit length. Notation on the right refers to the velocity, tangent vector and force associated with an entire link. Note that (F_i^x, F_i^y) and (\dot{x}_i, \dot{y}_i) lie in the $x - y$ plane while $\dot{\theta}_i$ and τ_i point out of the page in the \hat{z} direction.

the implications of large stroke amplitudes on optimality [153].

3.2 Methods

This section presents in detail the method used to find optimal stroke patterns and optimal swimming geometries for the three-link swimmer.

3.2.1 Geometry of the three-link swimmer

The three-link swimmer is modeled as a slender fiber of length $2L$ and radius r with characteristic aspect ratio $\kappa = r/2L$ (see figure 3-1). The arc-length s is measured along the centerline from one end of the swimmer to the other. The vectors $\mathbf{R}(s, t)$, $\mathbf{t}(s, t)$ and $\mathbf{n}(s, t)$ represent the position of the swimmer, and the tangential and normal unit vectors respectively at arc-length s and time t .

The swimmer is assumed to be rigid and undeformable except at two joints where

the centerline is free to bend (see figure 3-1). It can therefore be modeled as an inextensible jointed chain of three rigid cylindrical slender rods of length $2L_i$ (where $i = 1, 2, 3$ labels each of the three links), which are free to rotate at the two hinges between two adjacent links. We further consider a swimmer with a symmetric geometry i.e. $L_1 = L_3$ and we define the geometric parameter η as the ratio between the lengths of the middle link and the side links $\eta = L_2/L_1$.

The motion of the three-link swimmer is constrained to remain planar. Therefore the location of each link can be represented by a position vector $\mathbf{X}_i(t)$ corresponding to the three degrees of freedom: the two-dimensional position vector of the center of the link, $\mathbf{R}_i = (x_i, y_i)$ and the rotation angle θ_i , such that $\mathbf{X}_i(t) = (x_i(t), y_i(t), \theta_i(t))$ (see figure 3-1). The tangential and normal unit vectors to each link are given by $\mathbf{t}_i(t) = (\cos \theta_i(t), \sin \theta_i(t))$ and $\mathbf{n}_i(t) = (-\sin \theta_i(t), \cos \theta_i(t))$. For the sake of readability, the time dependency of all parameters will no longer appear explicitly.

The shape and the deformation of the swimmer is completely determined by imposing the value of the angles between two adjacent links at the hinges, $\varphi_1 = \theta_2 - \theta_1$ and $\varphi_2 = \theta_3 - \theta_2$ at all times. The superposition of the rigid body motion and the deformation, which is characterized by φ_1 and φ_2 , leads to the following constraints on the motion of the links relative to one another at each junction

$$\begin{aligned} \begin{pmatrix} \dot{x}_{i+1} \\ \dot{y}_{i+1} \end{pmatrix} - L_{i+1} \dot{\theta}_{i+1} \mathbf{n}_{i+1} &= \begin{pmatrix} \dot{x}_i \\ \dot{y}_i \end{pmatrix} + L_i \dot{\theta}_i \mathbf{n}_i, \\ \dot{\theta}_{i+1} &= \dot{\theta}_i + \dot{\varphi}_i. \end{aligned} \tag{3.1}$$

The two first equations are geometric compatibility equations, which ensure that the velocities of two neighboring links remain equal at the junction, such that the links do not detach. The third equation represents the prescribed deformation of the swimmer. We further define a velocity vector for each link as $\mathbf{V}_i = \dot{\mathbf{X}}_i = (\dot{x}_i, \dot{y}_i, \dot{\theta}_i)$.

3.2.2 Hydrodynamics

Slenderbody theory

The slenderness $1/\kappa$ of the three-link swimmer is assumed to be large. The hydrodynamics of the unbounded flow surrounding such slender deformable swimmers is taken into account using slenderbody theory, which spares us the challenge of solving Stokes equations (2.4) in the entire fluid domain. The slenderbody formulation derived by R.G. Cox [41] is used in this study. This formulation explicitly relates the local hydrodynamic force $\mathbf{f}(s)$ acting on the swimmer at position s to the velocity distribution $\mathbf{U}(s)$ along the entire length $2L$ of the slender fiber. This expression is obtained by asymptotic matching of an expansion in powers of $1/\ln \kappa$. All the details regarding the derivation of the slenderbody formulation can be found in [41]. The integral relationship between the force per unit length \mathbf{f} and the velocity distribution between $\hat{s} = 0$ and $\hat{s} = 2L$ takes the following form:

$$\frac{\mathbf{f}}{2\pi\mu} = \left[\frac{-\mathbf{U}}{\ln \kappa} + \frac{\lim_{\epsilon \rightarrow 0} (\mathbf{J} - \mathbf{U} \ln(2\epsilon))}{(\ln \kappa)^2} \right] \cdot [\mathbf{t}\mathbf{t} - 2 \mathbf{I}] + \frac{-\mathbf{U}}{2(\ln \kappa)^2} \cdot [3\mathbf{t}\mathbf{t} - 2 \mathbf{I}] + \mathcal{O}\left\{ \frac{1}{(\ln \kappa)^3} \right\}, \quad (3.2)$$

where

$$\mathbf{J} = -\frac{1}{2} \left[\int_0^{s-2L\epsilon} + \int_{s+2L\epsilon}^{2L} \right] \left[\frac{\mathbf{I}}{|\Delta|} + \frac{\Delta\Delta}{|\Delta|^3} \right] \times \left[\mathbf{I} - \frac{1}{2} \hat{\mathbf{t}}\hat{\mathbf{t}} \right] \cdot \hat{\mathbf{U}} d\hat{s}, \quad (3.3)$$

here \mathbf{I} stands for the identity operator and the following notation simplifications have been used: $\mathbf{f} = \mathbf{f}(s)$, $\mathbf{U} = \mathbf{U}(s)$, $\hat{\mathbf{U}} = \mathbf{U}(\hat{s})$, $\Delta = \mathbf{R} - \hat{\mathbf{R}}$, $\mathbf{R} = \mathbf{R}(s)$, $\hat{\mathbf{R}} = \mathbf{R}(\hat{s})$, $\mathbf{t} = \mathbf{t}(s)$, $\hat{\mathbf{t}} = \mathbf{t}(\hat{s})$. This formulation accounts, to first order, for non-local hydrodynamic interactions between the links, and is a reasonable approximation when the links interact weakly. When two links get too close to one another and approach self-intersection, the hydrodynamic interaction is no longer accurately modeled and the formulation becomes singular. Note that when the swimmer is infinitely slender, the first term in $1/\ln \kappa$ dominates the expansion. In this limit, slenderbody theory reduces to resistive force theory, and the local hydrodynamic force per unit length $\mathbf{f}(s)$ at location s is linearly proportional to local velocity $\mathbf{U}(s)$, the constant of

proportionality being given by the drag coefficients. Furthermore in this limit, the ratio of the drag coefficients in the normal and tangential directions is equal to two as can be inferred from the tensor $[\mathbf{t}\mathbf{t} - 2\mathbf{I}]$. In all results presented here, the interaction term in $1/(\ln \kappa)^2$ is always preserved.

The force distribution \mathbf{f} and interaction term \mathbf{J} given by equations (3.2) and (3.3) are integrated over each separate link to find the resultant hydrodynamic forces (F_i^x, F_i^y) and moments τ_i acting on each link. All moments are computed about the center of the middle link.

$$\begin{aligned} (F_i^x, F_i^y) &= \int_{2L_i} (\mathbf{f}(s) \cdot \hat{\mathbf{x}}, \mathbf{f}(s) \cdot \hat{\mathbf{y}}) ds \\ \tau_i &= \int_{2L_i} (\mathbf{R} - \mathbf{R}_2) \times \mathbf{f}(s) ds . \end{aligned} \quad (3.4)$$

For all integrals, the velocity $\mathbf{U}(s)$ at location s along the swimmer can be expressed as a function of the components of the velocity vectors \mathbf{V}_i . We symbolically define a force vector $\mathbf{F}_i = (F_i^x, F_i^y, \tau_i)$ for each link, see figure 3-1; after integration, equations (3.4) take the form:

$$\mathbf{F}_i = \sum_{j=1}^3 \mathbf{A}_i^j \mathbf{V}_j . \quad (3.5)$$

The coefficients of the matrix \mathbf{A}_i^j are obtained by integration of equations (3.2) and (3.3) (see appendix A for more detail on the derivation of the coefficients). As expected from the linearity of Stokes equations, the force vectors of each links are linear functions of the velocity vectors. Furthermore, the force acting on a given link depends on the motion of all the three links, as expected for a slenderbody formulation accounting for non-local interactions.

The physics of slenderbodies at low Reynolds number

Using this slenderbody formulation, one can find the drag coefficients for a slender rod of slenderness $1/\kappa$ and length $2L$ by simply integrating equations (3.2,3.3) analytically

for a straight filament. Let \mathbf{t} , \mathbf{n} , \mathbf{U} and \mathbf{F} be the tangential vector, normal vector, velocity at the center of the link and total hydrodynamic force acting on the rod respectively. The force \mathbf{F} on the rod is linear in \mathbf{U} and can be written as

$$\mathbf{F} = c^{\parallel}(\mathbf{U} \cdot \mathbf{t})\mathbf{t} + c^{\perp}(\mathbf{U} \cdot \mathbf{n})\mathbf{n} , \quad (3.6)$$

with the following expressions for the drag coefficients

$$c^{\parallel} = -\frac{4\pi\mu L}{\ln(\frac{2}{\kappa}) - \frac{3}{2}} , \quad (3.7)$$

$$c^{\perp} = -\frac{8\pi\mu L}{\ln(\frac{2}{\kappa}) - \frac{1}{2}} . \quad (3.8)$$

Note that the drag coefficient in the normal direction is larger than the coefficient in the tangential direction. The ratio $r_K = c^{\parallel}/c^{\perp}$ approaches 0.5 in the limit of infinitely slender bodies, which is historically the value used by Gray in Hancock in their original investigation of flagellar hydrodynamic using resistive force theory [65]. It is important to see that this drag anisotropy lies at the origin of propulsion for slenderbodies. In fact it can be shown that for a locally isotropic drag, deforming slenderbodies are unable to generate any net motion. A detailed discussion of this as well as a rigorous mathematical proof can be found in [10].

3.2.3 Equations of motion

As discussed in chapter 2, the motion of the swimmer is governed by conservation of linear and angular momentum. In the low Reynolds number case, this simply implies that the motion of the swimmer is force- and torque-free. With the notation introduced earlier, these equilibrium equations can be written as

$$\sum_{i=1}^3 \mathbf{F}_i = \sum_{i=1}^3 \left(\sum_{j=1}^3 \mathbf{A}_i^j \mathbf{V}_j \right) = \mathbf{0} . \quad (3.9)$$

Equations (3.1) and (3.9) form a system of nine equations in the nine unknowns $(\mathbf{V}_1, \mathbf{V}_2, \mathbf{V}_3)$, which can be written as a system of coupled first order differential equa-

tions in $(\mathbf{X}_1, \mathbf{X}_2, \mathbf{X}_3)$ which is integrated in time using a fourth order Runge–Kutta scheme as discussed in section 2.3.3.

Finally, the rate of work Φ exerted by the swimmer on the viscous fluid as it deforms can be evaluated during the stroke as

$$\Phi = \int_0^{2L} \mathbf{f}(s) \cdot \mathbf{U}(s) ds = \sum_{i=0}^3 \mathbf{F}_i \cdot \mathbf{V}_i . \quad (3.10)$$

The square root of Φ is then integrated in time as required by equation (2.12), in order to compute the minimal achievable work for a given stroke kinematics.

3.2.4 Optimization of the three-link swimmer

Parameterization of the stroke

As we have just seen in section 3.2.1, the deformation of the three link swimmer is entirely determined by the time variations of the two angles φ_1 and φ_2 between the middle link and the two side links. Hence, all instantaneous configurations of the three-link swimmer can be represented by a single point in the two dimensional (φ_1, φ_2) -space. A “stroke” is a periodic deformation of the swimmer, which is entirely determined by the periodic sequence of configurations (φ_1, φ_2) . It can therefore be represented by a single closed curve in the two dimensional (φ_1, φ_2) -space. For example, the original stroke suggested by E.M. Purcell [121], in which only one arm moves at a time, can be represented as a square in the (φ_1, φ_2) -space. This stroke will be referred to as the “Purcell stroke” (see figure 3-3) and is the only sequence considered in the study by Becker *et al* [10]. The problem of finding optimal stroke kinematics for the three-link swimmer can therefore be understood as finding a closed curve in the (φ_1, φ_2) -space, which maximizes a given objective function. Without loss of generality, all strokes can be parameterized and represented by two periodic functions $\varphi_1(t)$ and $\varphi_2(t)$ of period T , which we seek to determine in this study.

A given stroke needs to be represented by a finite set of parameters in order to use the nonlinear optimization procedure described in section 2.3.4. Since we wish to

find two periodic functions $\varphi_1(t)$ and $\varphi_2(t)$, an obvious choice of discrete parameters to represent the stroke are the Fourier coefficients in the development of $\varphi_1(t)$ and $\varphi_2(t)$ in a Fourier series. For regular and differentiable functions, the amplitude of the Fourier coefficients decays rapidly to zero and thus our optimization procedure can be based on finding the optimal first k coefficients of the series such that:

$$\varphi_1(t) = a_0^{\varphi_1} + \sum_{n=1}^k \left(a_n^{\varphi_1} \cos\left(\frac{2\pi nt}{T}\right) + b_n^{\varphi_1} \sin\left(\frac{2\pi nt}{T}\right) \right), \quad (3.11)$$

$$\varphi_2(t) = a_0^{\varphi_2} + \sum_{n=1}^k \left(a_n^{\varphi_2} \cos\left(\frac{2\pi nt}{T}\right) + b_n^{\varphi_2} \sin\left(\frac{2\pi nt}{T}\right) \right). \quad (3.12)$$

In addition to the stroke kinematics, the geometry of the swimmer can be simultaneously optimized as well. This simply requires that we add the geometric parameter η to the list of optimization parameters.

Constraints for singular strokes

As noted before, our formulation for the hydrodynamics around the swimmer breaks down and becomes singular when the links approach one another too closely. Hence in the following, we constrain the maximum attainable angle between two neighboring links by imposing the two following constraints

$$\begin{aligned} |\varphi_1(t)| &\leq \frac{3\pi}{4}, \\ |\varphi_2(t)| &\leq \frac{3\pi}{4}. \end{aligned} \quad (3.13)$$

These constraints become rather important as the value of the slenderness $1/\kappa$ is decreased and the interaction term becomes significant. In this case, singularities occurring for strokes close to self-intersection are large enough to significantly affect our model for the hydrodynamics and alter the objective function landscape. In this case, the optimization algorithm eventually fails (as it tends to converge toward singularities).

Alternatively, this problem can be resolved by regularizing the singularities di-

rectly in the hydrodynamic formulation. This approach has been pursued as well and will be described in detail later in this chapter when we investigate large amplitude strokes.

Objective function

We now define more precisely the objective functions used in this analysis. Here, we investigate stroke patterns of the three link swimmer for both swimming efficiency and distance traveled during the stroke. These two functions are precisely the ones considered by Becker *et al.* [10].

Let T be the period of the stroke, ℓ_0 the distance traveled by the swimmer during one stroke, and W_{\min} the minimal work associated with the stroke. The first objective function considered is the distance traveled by the swimmer ℓ_0 . The second objective function is the swimming efficiency \mathcal{E} defined in section 2.3.4. The “equivalent swimmer” required in the definition of \mathcal{E} is in this case the fully straighten three link swimmer for which $\varphi_1 = 0$ and $\varphi_2 = 0$. Hence the swimming efficiency can be written

$$\mathcal{E} = \frac{c^{\parallel} U_0 \ell_0}{W_{\min}} . \quad (3.14)$$

With this definition, \mathcal{E} represents the ratio of the work required to translate the straightened three-link swimmer along its axis at velocity U_0 for a distance of ℓ_0 over the total work exerted by the swimmer during the stroke.

Zero net rotation strokes

We end this description of the methods by returning to the discussion of non-zero net rotation strokes initiated in section 2.3.4. Since the stroke kinematics are optimized over only one period, there is no guarantee that the optimal stroke will in fact only result in a net translation of the swimmer, with no net rotation. This condition can be imposed using two different methods.

The first approach to this problem is to impose the zero net rotation condition via a simple penalty scheme. In this case, the efficiency is simply weighted with a

prefactor function of the rotation angle $\Delta\theta = \theta_0(T) - \theta_0(0)$, which decreases the efficiency as the rotation angle increases. The efficiency takes the form

$$\mathcal{E} = c^{\parallel} (1 - \beta (\Delta\theta)^2) \frac{U_0 \ell_0}{W_{\min}}, \quad (3.15)$$

where β is a scalar. A typical range of values used for this scalar is $\beta = 100 - -1000$. However, this value has very little impact on the optimal strokes that were ultimately discovered.

Additionally, certain symmetries in the stroke itself can be implicitly assumed and ensure that the swimmer does not rotate over one stroke. Such symmetries will be discussed in the next section.

3.3 Optimal strokes for the three-link swimmer

3.3.1 Limit of infinitely slender swimmers

General comments on the symmetry and structure of optimal strokes

Several general observations can be made regarding optimal stroke sequences. First, because of the linearity and time independence of Stokes equations, we expect optimal strokes to be symmetric with respect to reflections across the axes $\varphi_1 = \varphi_2$ and $\varphi_1 = -\varphi_2$. This can be seen by considering a geometrical configuration where $\varphi_1 = \varphi_2$. In this case, the axis of direction \mathbf{n}_2 going through the center of the middle link is a symmetry axis of the swimmer (see diagrams on figure 3-3). Starting from this configuration, sweeping the right arm down and moving forward in time is indistinguishable from sweeping the left arm down and moving backwards in time. The optimal stroke should be invariant if played backwards in time (time independency) and reflected about the body's line of symmetry (linearity). Hence $\varphi_1 = \varphi_2$ is an axis of symmetry. The second axis of symmetry can be deduced in a comparable way, as the arms of the swimmer are also interchangeable in a configuration such that $\varphi_1 = -\varphi_2$. This can be readily seen since for $\varphi_1 = -\varphi_2$ the center of the middle link

is a symmetry center of the swimmer (see diagrams on figure 3-3). It should be noted that this is not the case for the two axis defined by $\varphi_1 = 0$ and $\varphi_2 = 0$. Along these two axes, the configuration of the swimmer does not show any apparent symmetries and the arms can be uniquely identified by their positions relative to the body. In this case, symmetry arguments do not apply and the stroke pattern is not expected to be symmetric relative to reflections across the two axes defined by $\varphi_1 = 0$ and $\varphi_2 = 0$.

These symmetries allow us to restrict our computations to one quarter of the optimal curve in a frame $(\hat{\varphi}_1, \hat{\varphi}_2)$ that has been rotated from the original (φ_1, φ_2) frame by $\pi/4$, such that $\hat{\varphi}_1 = \frac{\sqrt{2}}{2}(\varphi_1 + \varphi_2)$ and $\hat{\varphi}_2 = \frac{\sqrt{2}}{2}(-\varphi_1 + \varphi_2)$. With this definition, $\hat{\varphi}_1$ corresponds to the axis $\varphi_1 = \varphi_2$ and $\hat{\varphi}_2$ to the axis $\varphi_1 = -\varphi_2$. The symmetries impose the following constraints on $\hat{\varphi}_1$ and $\hat{\varphi}_2$

$$\begin{aligned}\hat{\varphi}_1(t) &= \hat{\varphi}_1(-t) , \\ \hat{\varphi}_1(t) &= -\hat{\varphi}_1\left(\frac{T}{2} - t\right) , \\ \hat{\varphi}_2(t) &= -\hat{\varphi}_2(-t) , \\ \hat{\varphi}_2(t) &= \hat{\varphi}_2\left(\frac{T}{2} - t\right) .\end{aligned}$$

These constraints can be taken into account without loss of generality by assuming the following expressions for $\hat{\varphi}_1$ and $\hat{\varphi}_2$:

$$\begin{aligned}\hat{\varphi}_1(t) &= \sum_{p=0}^k a_{2p+1}^{\hat{\varphi}_1} \cos\left(\frac{2\pi}{T}(2p+1)t\right) , \\ \hat{\varphi}_2(t) &= \sum_{p=0}^k b_{2p+1}^{\hat{\varphi}_2} \sin\left(\frac{2\pi}{T}(2p+1)t\right) .\end{aligned}\tag{3.16}$$

These expressions for the Fourier expansions enable us to consider a factor of four times fewer deformation parameters as that required by the original Fourier development given by equations (3.11).

Furthermore, because at all time t , $\hat{\varphi}_1(t+T/2) = -\hat{\varphi}_1(t)$ and $\hat{\varphi}_2(t+T/2) = -\hat{\varphi}_2(t)$,

these axes of symmetry imply that there is no net rotation over one complete stroke cycle, preventing the optimal swimmer from going in circles. This can be understood with the following simple argument. The first half of the stroke between $t = 0$ and $t = T/2$ might lead to a certain rotation characterized by a change in angle θ_0 . However, during the second half of the stroke between $t = T/2$ and $t = T$ deformation is equal and opposite, and by linearity of Stokes equations, will lead to the exact same rotation but in the opposite direction. Hence for such deformations of the swimmer, there will be zero net rotation at the end of the stroke and the penalty scheme introduced in section 3.2.4 is no longer necessary.

Finally, two additional observations can be made regarding the amplitude of optimal stroke sequences. For small amplitude strokes, the distance traveled ℓ_0 , the average speed U_0 , and the mechanical work Φ , all go to zero. An expansion of the efficiency, \mathcal{E} , shows that it too decays to zero for small φ_1 and φ_2 . Thus regardless of which of the two optimality criteria we choose, small strokes are never desirable. For larger amplitudes, U_0 is bounded while it can be shown that Φ increases quadratically with amplitude; so again, large amplitude strokes are suboptimal. Thus optimal stroke patterns are expected to exist and to be found within a finite ring in the (φ_1, φ_2) -space centered at the origin.

Optimal stroke kinematics

We first consider the case of an infinitely slender swimmer, $1/\kappa \rightarrow \infty$, and search for stroke patterns that optimize swimming efficiency and distance traveled. In this study, we extensively explore the space of all acceptable three-link strokes by starting the optimization procedure from a wide variety of initial guesses, as represented in figure 3-2. We seek at first to find optimal strokes using the most general decomposition in Fourier coefficients given by equations (3.11). Using this general parameterization, initial guesses are taken to be circles of radius r^φ in the (φ_1, φ_2) -space with the center located at point (x^φ, y^φ) , such that $a_0^{\varphi_1} = x^\varphi$, $a_0^{\varphi_2} = y^\varphi$, $a_1^{\varphi_1} = r^\varphi$ and $b_1^{\varphi_2} = r^\varphi$. For all initial guesses, the center and radius of the circle are chosen to satisfy the constraints of equation (3.13). Initial guesses used in this investigation include circles with the

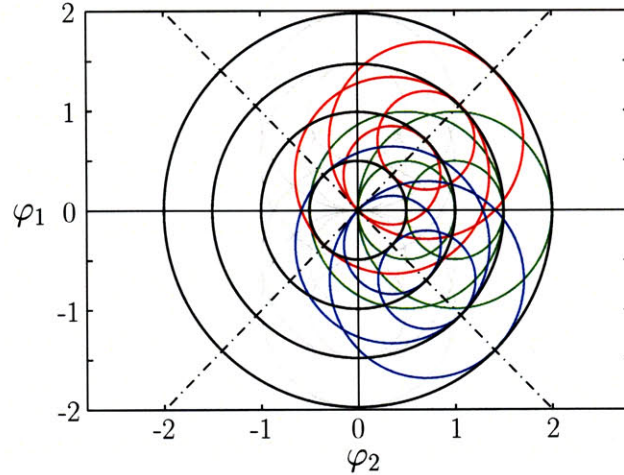


Figure 3-2: Representation in the (φ_1, φ_2) -phase plane of initial stroke sequences used in the optimization of the three-link swimmer.

following characteristics: $x^\varphi = y^\varphi = 0$, $x^\varphi = -y^\varphi$, $x^\varphi = y^\varphi$, $x^\varphi = 0$ and $y^\varphi = 0$ (see figure 3-2). Note that for the three last conditions listed above, the corresponding strokes do not satisfy the zero net rotation condition at the end of the stroke as they do not have the symmetries discussed previously.

For each objective function, the optimization procedure rapidly converges to a unique solution regardless of the initial guess. Hence, it appears that the phase space is well-behaved and that there are well defined optimal stroke kinematics for a three-link swimmer moving at low Reynolds number. Optimal stroke sequences are shown in figure 3-3. The black ovoid is the optimal stroke for swimming efficiency and the medium gray peanut shaped stroke is optimized for distance traveled. An important observation is that, as expected, both optimal strokes have the two axis of symmetry $\varphi_1 = \varphi_2$ and $\varphi_1 = -\varphi_2$ discussed above.

It bears emphasis, that these strokes were found using the general Fourier decomposition from equations (3.11), which does not impose any symmetries on the solution. In fact, the procedure converges to these symmetrical optima even for initial guesses with no symmetries, for which there is a non zero net rotation (see figure 3-2). This justifies our later use of the simplified Fourier development given by equation (3.16),

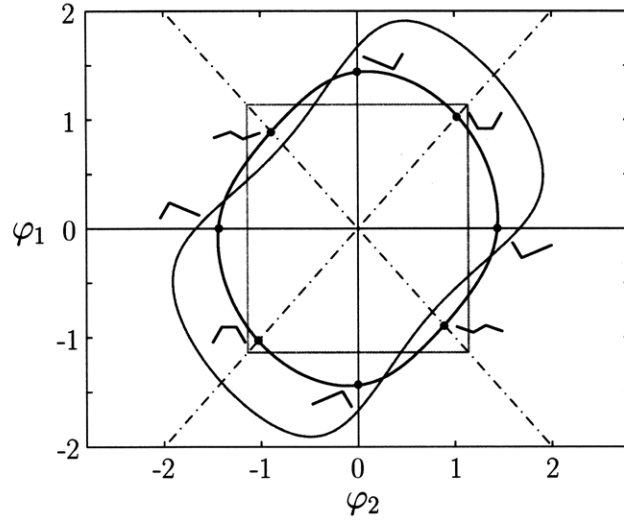


Figure 3-3: Stroke sequences of three-link swimmers in the (φ_1, φ_2) -phase plane for: (black line) optimal efficiency, (medium gray line) optimal velocity and (light gray line) the optimal “Purcell stroke” which corresponds to the square. Small swimmer diagrams correspond to successive configurations of the swimmer during the stroke. The swimmer moves to the left when the trajectory is followed counterclockwise and to the right otherwise.

which enables us to compute significantly more terms in the Fourier development of optimal strokes.

In this discussion, Stokes equations have been made nondimensional using the length scale $L_{\text{ref}} = L_1$ and the time scale T_{ref} . The optimal distance stroke corresponds to a dimensionless distance traveled of 0.623 with an efficiency of 0.0093. In comparison, the maximum distance attained with the Purcell stroke is 0.483 with a corresponding efficiency of 0.0063. This represents an increase of about 29 %. The gain is even more striking when considering the efficiency criterion. The maximum efficiency reached by the optimized three-link swimmer is 0.0130 (see Figure 3-3) for a link ratio of $\eta = 0.933$ and a corresponding dimensionless distance traveled of 0.492; in contrast, the best efficiency achieved with the Purcell stroke is 0.0077 with $\eta = 0.809$ (and a distance of 0.420) as computed by Becker *et al.* in [10]. The optimal efficiency 0.0130 value reflects the expected order of magnitude for low Reynolds number swimmers. In comparison, the maximum efficiency achieved by an undulating slender rod

propagating a sinusoidal wave is 0.0736, as calculated by Hancock [69]. The increase in efficiency between the Purcell stroke proposed in [10] and the optimal stroke is of 69 %, which is significant and testifies to the relevance of optimizing kinematics in low Reynolds number swimming. This large increase in efficiency is due to the added degrees of freedom allowed by the general description of stroke kinematics, which enables the optimization procedure to converge to stroke patterns able to dissipate less energy against viscosity. For such strokes, the increase in efficiency is significant because, in the low Reynolds number regime, the hydrodynamics is completely dominated by viscosity.

3.3.2 Effect of finite slenderness

The effect of finite slenderness on the optimal efficiency is investigated here. In this study, the slenderness is imposed and the stroke kinematics which maximizes the efficiency is computed using the same procedure as in the infinite slenderness case. Slendernesses ranging from $1/\kappa = 10^2$ to 10^{15} were investigated. For this range of slenderness, there is no qualitative change in the structure of the stroke, which remained close to the stroke depicted in figure 3-3. The value of the maximal efficiency however increases significantly with the slenderness, asymptotically approaching the infinite slenderness limit for small values of κ (see figure 3-4). This suggests that, from a purely hydrodynamical standpoint, the three-link swimmer should be as slender as possible in order to be as efficient as possible. This could have been foreseen from our basic understanding of the mechanism underlying swimming of slenderbodies at low Reynolds number. As discussed above, the anisotropy in drag is what drives the propulsion at low Reynolds number. While the ratio of drag coefficients is of 2 for infinitely slender rods, it decreases significantly as the slenderness decreases (see equations (3.7)). Hence for moderately slender rods the anisotropy in drag decreases, which leads to less efficient swimming.

While slenderness is always desirable from the hydrodynamic stand point, it has a mechanical cost in terms of the material properties required to guarantee acceptable stiffness and robustness of an extremely slender swimmer. Hence, there seems to be

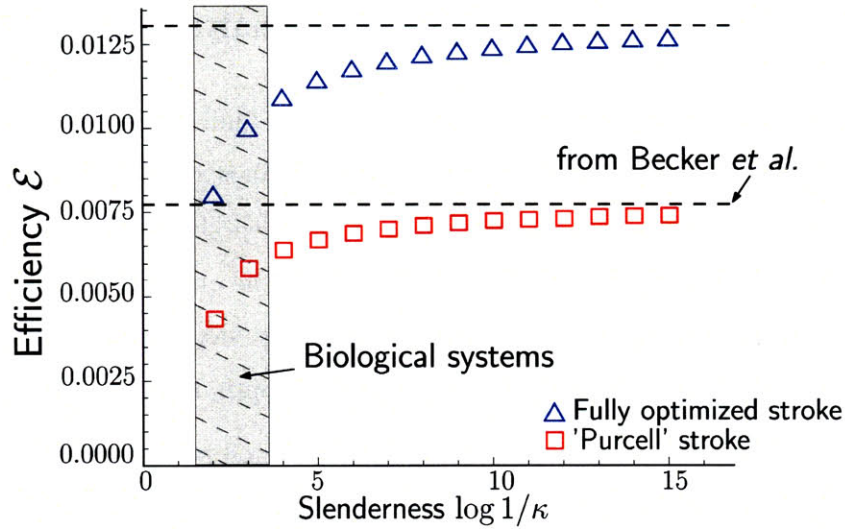


Figure 3-4: Efficiency of the three-link swimmer as a function of slenderness.

a tradeoff between the slenderness which would allow for highly efficient strokes and the slenderness which can be obtained in cases of practical interest.

It is therefore interesting to note that most of the increase in efficiency is obtained for slenderness less than 10^3 . In fact, the maximal efficiency for a swimmer of slenderness $1/\kappa = 10^3$ is within 80% of the efficiency of the infinitely slender swimmer. This suggests that most of the gain in efficiency can be obtained for slenderness on the order of 10^3 . While comparisons with biological systems should always be made cautiously, it is intriguing to note that slendernesses of that order of magnitude are in fact observed in the majority of microorganisms. The radius of a eukariotic flagellum is about $0.15 \mu\text{m}$ and can be over $100 \mu\text{m}$ in length [17], which corresponds to a slenderness on the order of 10^3 . Such organisms are obviously more complex than our rather crude three-link device, however both are subject to the same constraints imposed by low Reynolds number hydrodynamics. This observation may therefore be helpful in developing a better understanding of the basic hydrodynamical constraints acting on a slender swimmer.

3.3.3 Convergence and optimality analysis

The problem of finding optimal strokes for the three-link swimmer reduces to that of finding two periodic functions, which is itself equivalent to finding an optimal closed curve in the (φ_1, φ_2) -space. As the space of all acceptable strokes can be relatively easily represented, we will attempt to characterize the quality of the optimum found and make a few general observations regarding optimality for three-link swimmers. The scope of this short analysis is limited to strokes optimized for swimming efficiency.

We first investigate the smoothness of the optimal parameterization. Using the simplified Fourier series (equation (3.16)) which implicitly assumes certain symmetries, we compute the optimal stroke using $2k + 1 = 21$ harmonics. Once the optimization procedure has fully converged, the values of all the coefficients in the series are plotted as a function of the index of the corresponding harmonic, see figure 3-5(a). The semi-log plot shows that the amplitude of the coefficients in the Fourier development decays to zero exponentially, which is the signature of an infinitely smooth and differentiable function. For such functions, only the first few harmonics are necessary to determine the dominant behavior of the function, as the amplitude of higher harmonics rapidly decays to zero.

We further investigate how many terms are necessary in the Fourier series to achieve a desired accuracy. The optimal stroke for swimming efficiency is now fully computed by including an increasing number of harmonics in the development. For each of these strokes, the normalized error in the optimal efficiency is computed, assuming the stroke computed with the maximum number of $2k + 1 = 21$ harmonics is the exact solution. Figure 3-5(b) shows the rapid decay ($\sim 1/n^5$) of the error in the efficiency. In fact the efficiency of the stroke, computed with only the first harmonic in the expansion, is already within 1 % of that of the optimal solution.

The two previous observations strongly suggest that the first harmonic – corresponding to the two coefficients $a_1^{\varphi_1}$ and $b_1^{\varphi_2}$ in equation (3.16) – dominates the behavior of the stroke and determines its main characteristics. This allows us to project the space of all acceptable strokes onto the two dimensional $(a_1^{\varphi_1}, b_1^{\varphi_2})$ -space,

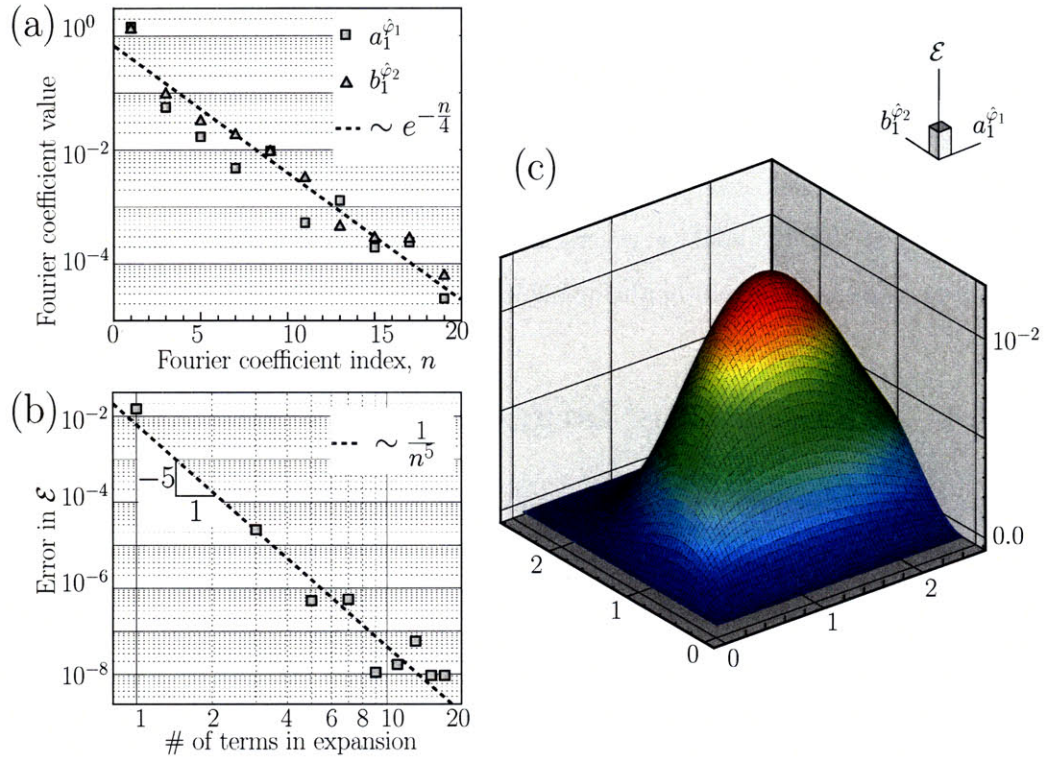


Figure 3-5: (a): Semi-log plot showing exponential decay of the amplitude of the Fourier coefficients. (b): Log-log plot of the normalized error in the efficiency as a function of the number of terms in the Fourier series used to find the optimal stroke. (c): Efficiency as a function of the two dominant terms in the Fourier expansion.

in order to gain insight about optimality of three-link strokes. Figure 3-5(c) shows the efficiency \mathcal{E} of strokes computed using only the first harmonic in the Fourier expansion. The swimming efficiency \mathcal{E} is a quasi-convex function of the two variables $a_1^{\hat{\phi}_1}$ and $b_1^{\hat{\phi}_2}$, which has a unique global maximum in this reduced space. Although the optimization procedure only guarantees convergence to a local maximum, this strongly suggests that the global optimum or at least a very strong optimum has been achieved. This is also suggested from our investigation of the space of acceptable optimal strokes, for which the optimization procedure systematically converged to the this same stroke, regardless of the initial guess, see section 3.3.1. Finally, this analysis shows that the problem of optimizing locomotion is well-defined and well-behaved at low Reynolds numbers and suggests that a locomotion optimization of more complex swimmers might be achievable.

3.4 Investigating large amplitude strokes

We end this chapter on the optimization of three-link swimmer locomotion by giving some insight into what ensues when the constraint on the stroke amplitude (equation (3.13)) is relaxed and the swimmer is allowed to undergo large amplitude strokes. This work is the result of an original correspondence with O. Raz and J.E. Avron, which can also be found in [126] and [153].

3.4.1 Large amplitude strokes of O. Raz and J.E. Avron

For infinitely slender swimmers, the existence of highly efficient large amplitude strokes has been suggested in [10]. This study only investigated the Purcell stroke and optimized the stroke amplitude only. In this case, two optima were found: the first (against which our previous results are compared) has an efficiency of 0.0077 for a stroke angle of 1.13 rad and the second has an efficiency of 0.0155 (already higher than the stroke we present) for a stroke angle of 2.98 rad. The rationale for comparing our results with the lower efficiency stroke corresponding to a smaller stroke amplitude will become clear in the following discussion.

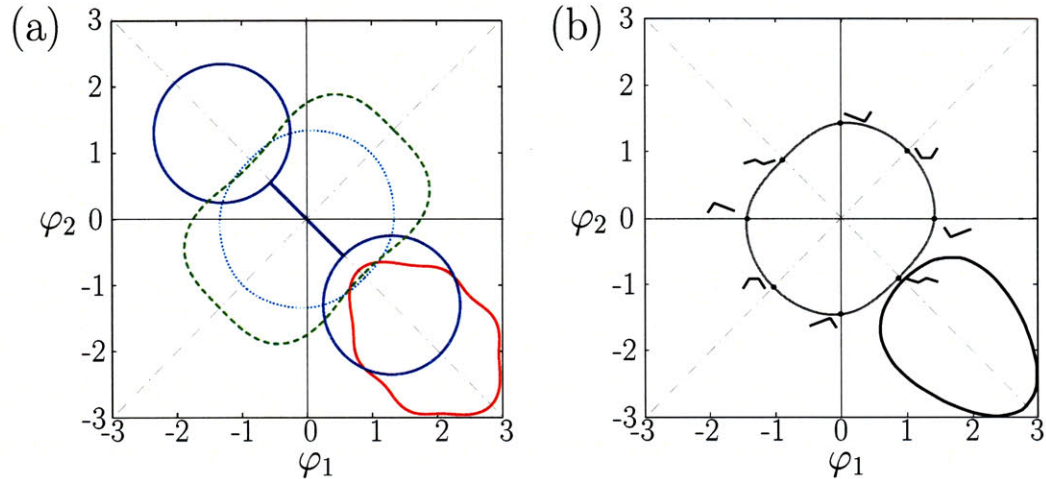


Figure 3-6: (a): Three-link swimmer strokes from O. Raz and J.E. Avron. The plot is reproduced from [126] with its original caption: “The φ_1 and φ_2 are the exterior angles made by the center link and the two arms. The approximate rectangle (green) represents the distance optimizer of the moderate strokes of Tam and Hosoi [153]. The (blue) dumbbell is a large stroke that outperforms the moderate stroke. The approximate (light-blue) circle in the center represents the efficiency optimizer of the moderate strokes found by Tam and Hosoi [153]. The off-center (red) wobble oval is a large stroke with higher efficiency”. (b): Optimal large amplitude stroke for swimming efficiency.

In their own investigation on optimal stroke patterns for Purcell’s three-link swimmer, O. Raz and J.E. Avron allow for large amplitude strokes (φ_1 and φ_2 up to values close to π) and propose two new stroke patterns that have been optimized for efficiency and distance traveled for an infinitely slender swimmer. The new stroke patterns better our optimized results for efficiency and distance traveled from section 3.3.1 by approximately 50 % and 10 % respectively and hence are mathematically superior. These strokes are represented in figure 3-6(a). However, some care must be taken as such mathematical results may not necessarily be relevant to biological or engineering systems which often conceal subtle constraints.

It should be noted that both the efficiency stroke suggested by O. Raz and J.E. Avron [126] and the large amplitude peak in the study of Becker *et al.* [10] are suspect as they arise at very large amplitudes, where the stroke angle becomes close to π and for which the arm and body pass quite close to one another. In this large amplitude regime, hydrodynamic interactions between links become non-negligible

for any realistic values of κ and resistive force theory should not be used to model the hydrodynamics. In fact, an early investigation of the efficient large amplitude Purcell stroke suggested by Becker *et al.* [10] showed that when taking into account the far field hydrodynamic interaction, the efficiency is well below the asymptotic value for any physically achievable slenderness $1/\kappa$, which is why we discarded such strokes in the first place and only compared our results to the first efficiency peak in [10].

The present short investigation of high amplitude strokes focuses primarily on strokes optimized for swimming efficiency. First we will revisit our model in order to include large amplitude efficient strokes and we will see how these compare to the optimal stroke found in section 3.3.1 as the slenderness $1/\kappa$ is decreased to realistic values. Finally, we will briefly comment on inherent problems associated with strokes optimized for distance traveled.

3.4.2 Efficient large amplitude strokes

In the following, the upper bound imposed on the angles φ_1 and φ_2 (equations (3.13)) is relaxed from $3\pi/4$ to 3. This new bounding value is the same as the one used by O. Raz and J.E. Avron in their investigation of efficient strokes, and it allows for large amplitude strokes as $\pi \sim 3$.

Regularization of slenderbody theory

The singularity associated with slenderbody theory has been discussed earlier in sections 3.2.2 and 3.2.4. When investigating high amplitude strokes, our formulation breaks because the optimization procedure is attracted towards nearby singular configurations, which occur when two links get extremely close together, almost overlapping. Those singularities are exclusively due to the slenderbody formulation and are not representative of any underlying phenomena arising from the physics of the fluid. In fact, it is well known that when two cylinders get very close to one another, the hydrodynamic interaction becomes dominated by a lubrication layer. The interaction between two neighboring links through a lubrication layer will cause considerable

viscous dissipation but no locomotion. Therefore, strokes approaching such configurations are never expected to be efficient for locomotion and we do not expect to find any optimal stroke in this regime. The failure of the optimization procedure is solely due to an inaccurate representation of the strong lubrication interactions, which only come into play when the links are within a few radii r of one another.

In this analysis, we regularize the singularities, by superposing an artificial lubrication term to the far field hydrodynamic term given by slenderbody theory (see appendix A for more detail on the artificial lubrication used here). This artificial term is constructed such that it retains all the physics of the real lubrication layer, albeit without solving it exactly. The lubrication force between two parallel cylinders approaching each other is known to scale as $\delta^{-\frac{3}{2}}$, where δ is the gap distance. Therefore, the lubrication interaction is only significant when the centerlines of two links are within a few radii r of one another. Furthermore, the lubrication forces exerted by one link on the other are equal and opposite in sign. Therefore, the lubrication interaction does not alter the equilibrium equations and the motion of the swimmer. However, it does affect the viscous dissipation term when two links get too close. Alternatively, the artificial lubrication term used in this study can be understood as a penalty scheme, which represents the relevant physical effects of lubrication: its effect is limited to stroke patterns that approach self-intersection, it does not alter the motion ℓ_0 of the swimmer, it strongly increases the viscous dissipation and thus W_{\min} for stroke patterns approaching self-intersection and therefore significantly decreases the efficiency for such strokes.

In conclusion, the addition of the artificial lubrication term enables us to explore large amplitude strokes as it prevents the optimization procedure from being attracted by singularities. However one must be careful to verify that this artificial term does not introduce any non-physical phenomenon which could be exploited to find non-physical optima. Hence, once the optimally efficient stroke is found and the value of the optimal efficiency is known, the stroke is computed a second time without the addition of the lubrication term. In all our computation, the values for the efficiency of the optimal stroke computed with and without the lubrication term are found

to be similar. This confirms that, even though the amplitude of the stroke is large with angles approaching the upper bound value of $\varphi_1, \varphi_2 \leq 3$ the swimmer remains sufficiently far from self-intersecting configurations at all times. Thus, the lubrication term (which is only significant when the links are within a few radii of one another) does not artificially alter the value of the efficiency of the optima.

Effect of finite slenderness on large amplitude strokes

We first consider infinitely slender swimmers and investigate the (φ_1, φ_2) -space with the relaxed constraints by following the same procedure described in section 3.3.1. When large amplitude strokes are permitted, we find two locally optimal strokes for swimming efficiency. The first one has been discussed in the previous section 3.3.1. It is centered in the middle of the (φ_1, φ_2) -space and will be referred to as the optimal medium amplitude stroke. The second one is located in the lower right quadrant, as suggested by O. Raz and J.E. Avron [126] and will be referred to as the optimal large amplitude stroke. The optimum, selected by the optimization procedure, merely depends on where in the (φ_1, φ_2) -space the initial circle is centered.

The stroke proposed by Raz and Avron is represented in figure 3-6(a) in the lower right quadrant. It has an asymptotic efficiency of 0.0199, which is 1.53 times higher than our original stroke, and reaches a large stroke angle of 3 rad. Figure 3-6(b) represents the two locally optimal strokes found by our procedure. The optimal large amplitude stroke is qualitatively similar to the one suggested by Raz and Avron, and it reaches a slightly better efficiency of 0.0210, which is 1.62 times higher than the optimal medium amplitude stroke.

We now quantify the effect of finite slenderness on the efficiency of large amplitude strokes. This is done in much the same way as in our previous investigation of the effects of finite slenderness. Again, we examine slenderness ranging from $1/\kappa = 10^2$ to 10^{15} . For each slenderness, we look for strokes with an optimal efficiency. Figure 3-6 reports the values of the optimal efficiency for the two local optima as functions of the slenderness. As before, the kinematics are fully optimized for each value of slenderness. It can be seen that the drop in efficiency for the optimal large amplitude

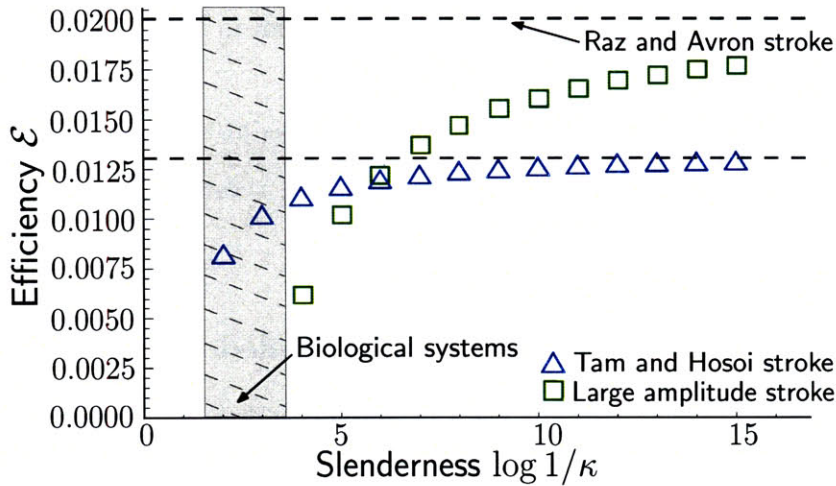


Figure 3-7: Efficiency of our optimized stroke and that of Raz and Avron as a function of $1/\kappa$.

stroke is much more severe than for the other one, as slenderness is decreased. This was predictable since for large amplitude kinematics, the interactions between links are accentuated and the arms and body of the three link swimmer push viscous fluid against one another. This leads to a drop in efficiency for swimmers of finite slenderness in which the hydrodynamic interaction becomes important. It bears emphasis, that this drop in efficiency is not a result of the artificial lubrication term introduced for the purpose of this analysis. In fact for this range of slenderness, the efficiency of the optimal large amplitude stroke was recomputed without the lubrication term and was found to be within 1 % of the value obtained with the lubrication term.

In figure 3-7, we show that for values of $\kappa \gtrsim 10^{-6}$, the optimal medium amplitude stroke outperforms the optimal large amplitude stroke. To put these numbers in perspective, eukaryotic flagella have a diameter of roughly 250-400 nm, owing to their common “9+2” microtubule structure [2]. Typical flagella lengths are on the order of 10 μm , although they may be as long as 200 μm , hence the biologically observed κ 's range from $10^{-2} - 10^{-3}$. A flagellum of prescribed radius on the order of 250-400 nm would require macroscopic flagellar lengths on the order of 20cm to achieve an aspect ratio of $\kappa \sim 10^{-6}$, which is 1000X longer than those observed in nature. Alternatively, for a microscopic flagellum of length on the order of 100 μm , an

aspect ratio of $\kappa \sim 10^{-6}$ would require the flagellum to have an unrealistic atomistic radius size of 1\AA .

Thus, while optimal large amplitude strokes exist for the three link swimmer in the non-physical limit of infinitely slender swimmers, these strokes become suboptimal for any realistic value of the slenderness $1/\kappa$.

3.4.3 Optimizing the distance traveled over one stroke

We end this chapter with a re-evaluation of the relevance of using the traveled distance ℓ_0 as an optimizer for low Reynolds number locomotion. This discussion is related to the stroke proposed by O. Raz and L.E. Avron [126] (see figure 3-6(a)), which outperforms our peanut shaped stroke (see figure 3-3) in terms of distance traveled over one stroke. The dumbbell stroke travels over a distance of 0.710, with a reference length equal to $L_{\text{ref}} = L_1$. This represents an increase of factor 1.14 compared to our peanut shaped stroke.

The problem of stronger hydrodynamic interactions for large amplitude strokes is no longer relevant for strokes, which are optimized for ℓ_0 only. However, the dumbbell solution invites another subtle question illustrated by the following analogy. Imagine a competition in which two athletes attempt to swim the furthest in one stroke. The first swimmer executes one perfect freestyle stroke. The second executes almost one complete cycle of freestyle, then flips over onto his back and does an almost complete backstroke before flipping back onto his stomach, doubling the distance of the first swimmer. Intuitively, we regard this trick as a clever cheat as the second swimmer has performed *two* strokes rather than one. This is precisely the scenario that the dumbbell describes: the three-link swimmer completes almost one full cycle (corresponding to one lobe of the dumbbell) then flips over in a reversible manner (linear connecting region), and repeats the cycle upside-down (the other lobe) and virtually doubles the distance traveled. Since the “linear connecting region” reflects reciprocal deformations, no net translation is associated with these segments and hence, the swimmer can freely take advantage of the cycle at the tip. Pushing this trick further, one could imagine a whole class of these “strokes” that are likely to beat

even the dumbbell. Consider a curve that consists of multiple path segments radiating from the origin of the (φ_1, φ_2) -space like the spokes of a wheel. Each “spoke” would carry an almost closed loop at its tip, and the distance traveled would be artificially increased.

Our working definition of a stroke is: a periodic deformation of the swimmer. In this regard, the dumbbell stroke should be regarded as legitimate as it is a periodic deformation of the swimmer. Furthermore, this definition of a stroke carries the same ambiguity as the definition of the period of a function. For example, the “cosine” function is 2π periodic, but it is also 4π periodic. Similarly, consider one period of a stroke. Going sequentially twice through the same stroke could also be seen as one stroke, in which case the distance traveled over one stroke is virtually increased by a factor of two. Therefore, the analysis of Raz and Avron exposes the limitation of our working definition for a stroke and points out an interesting and open mathematical question namely: What is a “stroke”?

Interestingly, this difficulty is unique to strokes that optimize distance and does not arise in the efficiency calculation. Even though the “spokes” do not cost the swimmer anything in distance traveled, they do cost energy. As these radial segments have an energetic price but no translational gain, it will always be more efficient to restrict the swimmer to the cycle at the tip than to perform the complicated (and energetically costly) flipping maneuver and repeat the cycle upside-down.

Perhaps an even more interesting remark, would be to question the relevance of using the distance traveled over one stroke as an optimizer all together. As discussed in section 2.3.4, the swimming efficiency is a measure of how fast and how energetically efficient a given stroke is. The distance traveled over one period on the other hand is a poorly defined optimizer. Therefore in the next two chapters, we will only investigate optimally efficient strokes, and will no longer use the distance traveled over one stroke as a useful metric.

Chapter 4

Optimal unflagellated swimmers

4.1 Introduction

Studying swimming properties of unflagellates is relevant both for its technological and biological implications: technological implications because engineering such microswimmers is feasible with today's technology [52] and biological implications because many simple eukaryotic organisms are unflagellates. An in-depth investigation of swimming unflagellates is of interest in different areas of biology and the pioneering work of Gray and Hancock [64, 65] has been followed by an increasing number of studies.

The eukaryotic flagellum described in chapter 2 has been extensively studied by molecular biologists. Such simple unicellular organisms do not have complex nervous feedback systems to control and regulate locomotion, yet they exhibit incredible degrees of coordination and control over the waveform of the flagella. The mechanical and chemical mechanisms underlying the coordination and regulation of flagellar beating remain poorly understood. Despite this shortcoming, flagellar waveforms of sperm cells have been recorded experimentally and investigated [75, 85, 92]. Also, computational simulation reproducing the molecular structure of the eukaryotic flagellum to various degrees of accuracy have been used to investigate simple mechanical mechanisms able to regulate and propagate waves along the flagellum [38, 40, 103]. The work of C. Brokaw is particularly significant in this regard [19–23, 84]. All of

these studies essentially focus on the waveform of the stroke.

Also, many biologists have investigated the adaptive significance of the morphology and morphometry of sperm cells. Sperm cells are highly specialized cells, which are subjected to high levels of competition within-males and for some species between-males. The relative sizes of the different parts of sperm cells (namely head, midpiece and flagellum) and their functional significance have been the subject of many studies [3, 18, 27, 43, 57–59, 96, 108, 119, 136, 146].

Living organisms and their behavior are complex and therefore challenging to understand, model and predict. While, any such attempt requires caution, sperm cells may be one of the few biological systems, where such effort may be rewarded. The function of sperm cells to transport genetic material to the egg as well as the use of a flagellum to locomote are sufficiently well-defined to make these cell amenable to mathematical models. Also, the high level of cell specialization together with the intense level of competition experienced by sperm cells seem to justify the optimization of the swimming function through computational simulations and the subsequent comparison with biological observations.

Previous studies have looked at optimal propulsion within a class of prescribed traveling waves [51, 74, 118]. In this chapter we investigate optimal unconstrained stroke kinematics, designs and morphologies of unflagellated swimmers. The methodology presented in chapter 2 and successfully applied to the study of the three-link swimmer in chapter 3, is extended to more complex geometries.

4.2 Methods

In this section, we describe our model for flagellated swimmers. While in general the method is similar to the one developed for the three-link swimmer (see chapter 3), the hydrodynamics and the kinematics of the swimmer need to be described in more detail.

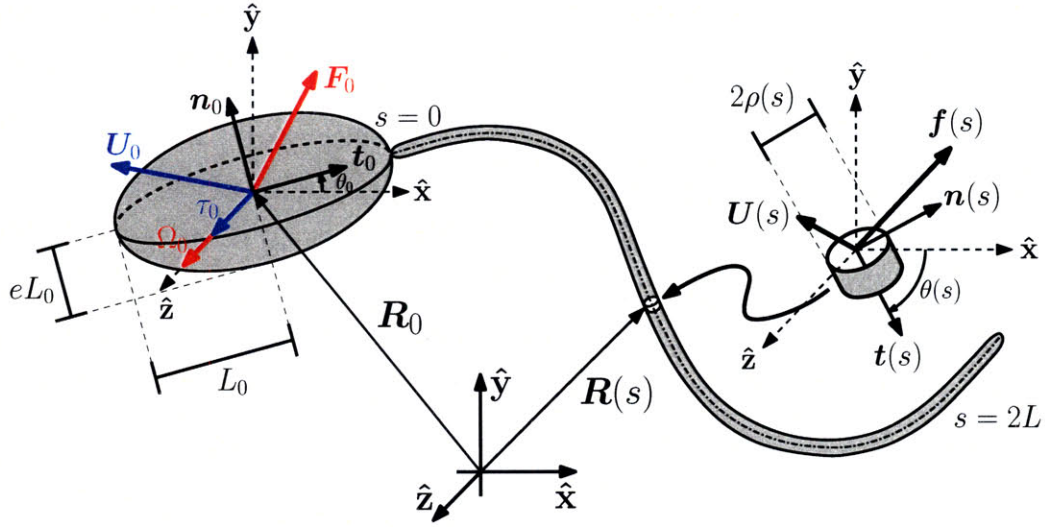


Figure 4-1: Schematic of a uniflagellated swimmer. The slice and corresponding notation on the right refer to the local velocity, tangent vector and drag force per unit length. Note that for the forces and velocities on the head \mathbf{F}_0 and \mathbf{U}_0 lie in the $\hat{\mathbf{x}} - \hat{\mathbf{y}}$ plane while τ_0 and Ω_0 point out of the page in the $\hat{\mathbf{z}}$ direction.

4.2.1 Geometry and deformation of the swimmer

Flagellated swimmers are modeled here as a spheroidal rigid head attached to a deformable flagellum (see figure 4-1). As with the study of the three-link swimmer in chapter 3, the motion of the swimmer is constrained to be planar.

The head is a prolate spheroid with semi-major axis L_0 and eccentricity e . The position of the spheroid is given at any time by both the position vector $\mathbf{R}_0(t) = (x_0(t), y_0(t))$ of the center O and the angle $\theta_0(t)$ between the $\hat{\mathbf{x}}$ -axis and the unit vector along the major axis of the spheroid $\mathbf{t}_0(t)$ (see figure 4-1). The unit vector normal to the major axis $\mathbf{n}_0(t)$ is defined by $\mathbf{n}_0(t) = \hat{\mathbf{z}} \times \mathbf{t}_0(t)$. The position vector $\mathbf{R}_0(t)$ of O together with the orientation $\theta_0(t)$ of the major axis constitute the reference location of the swimmer, as defined in section 2.3.1.

The flagellum is modeled as a slender fiber of length $2L$, characteristic radius r and aspect ratio $\kappa = r/2L$. Let s be the arc-length measured along the centerline of the flagellum and $\rho(s) = r\sqrt{\frac{(2L-s)s}{L^2}}$, $\gamma(t, s)$, $\mathbf{R}(t, s)$, $\mathbf{t}(t, s)$, $\mathbf{n}(t, s)$ and $\theta(t, s)$ be the radius*, curvature, position vector, tangential and normal unit vectors and angle

*An ellipsoidal shape for the slender flagellum is required by our model for the hydrodynamics

between the $\hat{\mathbf{x}}$ -axis and the tangential vector $\mathbf{t}(t, s)$ at time t and location s along the centerline (see figure 4-1). The flagellum is connected to the head at $s = 0$ such that the tangential unit vector at $s = 0$ has the same direction as the major axis of the head $\mathbf{t}(t, s = 0) = \mathbf{t}_0(t)$. With these boundary conditions, the location, shape and deformation of the flagellum are completely determined by the curvature $\gamma(t, s)$. The position vector $\mathbf{R}(t, s)$ along the flagellum can be deduced by integration of the Serret–Frenet equations along the centerline

$$\begin{aligned} \frac{\partial \mathbf{t}(t, s)}{\partial s} - \gamma(t, s) \hat{\mathbf{z}} \times \mathbf{t}(t, s) &= \mathbf{0} , \\ \frac{\partial \mathbf{R}(t, s)}{\partial s} &= \mathbf{t}(t, s), \end{aligned} \quad (4.1)$$

subject to the following conditions at $s = 0$

$$\mathbf{t}(t, 0) = \mathbf{t}_0(t) , \quad (4.2)$$

$$\mathbf{R}(t, 0) = \mathbf{R}_0(t) + L_0 \mathbf{t}_0(t) . \quad (4.3)$$

The velocity distribution along the centerline is written as the superposition of a rigid body motion and a deformation

$$\mathbf{U}(t, s) = \mathbf{U}^{\text{rig}}(t, s) + \mathbf{U}^{\text{def}}(t, s). \quad (4.4)$$

The rigid body motion of the swimmer \mathbf{U}^{rig} can be computed from the time derivatives of $\mathbf{R}_0(t)$ and $\theta_0(t)$ as given by equations (2.1). The deformation of the flagellum at each time t is known from the prescribed time variations of the curvature along the centerline. Hence \mathbf{U}^{def} is given at any time t by the integration of the time derivatives

around the flagellum, which we will later describe. This is due to the presence of terms like $\ln \frac{s(2L-s)}{\rho(s)^2}$ in the asymptotic expansion used to derive the slenderbody theory used in the present work. For a more detailed discussion see [61].

of the Serret–Frenet equations along the centerline

$$\begin{aligned} \frac{\partial \dot{\mathbf{t}}(t, s)}{\partial s} - \dot{\gamma}(t, s) \hat{\mathbf{z}} \times \mathbf{t}(t, s) - \gamma(t, s) \hat{\mathbf{z}} \times \dot{\mathbf{t}}(t, s) &= \mathbf{0} , \\ \frac{\partial \mathbf{U}^{\text{def}}(t, s)}{\partial s} &= \dot{\mathbf{t}}(t, s), \end{aligned} \quad (4.5)$$

subject to the following conditions at $s = 0$

$$\dot{\mathbf{t}}(t, 0) = \mathbf{0} , \quad (4.6)$$

$$\mathbf{U}^{\text{def}}(t, 0) = \mathbf{0}. \quad (4.7)$$

For readability, the dependency on time t will no longer appear explicitly and the dependency on the arc-length s will only appear, when required to avoid confusion. Whenever possible, the following notational simplifications will be used: $\mathbf{R}_0 = \mathbf{R}_0(t)$, $\mathbf{U}_0 = \mathbf{U}_0(t)$, $\mathbf{t}_0 = \mathbf{t}_0(t)$, $\mathbf{n}_0 = \mathbf{n}_0(t)$, $\theta_0 = \theta_0(t)$, $\mathbf{R} = \mathbf{R}(t, s)$, $\mathbf{U} = \mathbf{U}(t, s)$, $\mathbf{t} = \mathbf{t}(t, s)$, $\mathbf{n} = \mathbf{n}(t, s)$, $\theta = \theta(t, s)$, $\hat{\mathbf{R}} = \mathbf{R}(t, \hat{s})$, $\hat{\mathbf{t}} = \mathbf{t}(t, \hat{s})$, $\hat{\mathbf{n}} = \mathbf{n}(t, \hat{s})$.

4.2.2 Hydrodynamics around the swimmer

In order to accurately model the dynamic interactions between the swimmer and the surrounding fluid, we need to solve Stokes equations in an unbounded fluid domain. In place of the Stokes equations, one can derive an equivalent integral representation defined over the boundary of the fluid domain [1,91]. Hence at low Reynolds number, the flow field is best computed using a boundary element method.

In our case, an accurate numerical representation of the geometry of the swimmer would require an unfeasibly large number of boundary elements in the discretization of the surface, owing to the typically large aspect ratio, $1/\kappa \approx 10^3$ of the flagellum. Hence a full treatment of the hydrodynamics using boundary elements would be numerically costly and cannot be integrated into the optimization framework. In this study, the hydrodynamic equations are solved using a simpler singularity method, in which the system of fundamental solutions (or Green’s functions) is no longer distributed over the entire boundary of the fluid domain (i.e.: the surface of the

swimmer) but rather over the centerline of the swimmer. This essentially reduces the integral equation over the surface of the swimmer to a reduced integral equation, which is less accurate but can be solve more efficiently.

In the following, we first introduce the most commonly used fundamental solutions (or Green's functions) to the Stokes equations. We then describe the systems of singularities required to model both the flagellum and the head of the swimmer. Finally, we discuss how the interactions between the flagellum and the head can be taken into account.

Fundamental singular solutions to Stokes Equations

Consider the inhomogeneous Stokes equation

$$-\nabla p + \mu \nabla^2 \mathbf{u} = -\mathbf{f} \delta(\mathbf{x}) , \quad (4.8)$$

$$\nabla \cdot \mathbf{u} = 0 , \quad (4.9)$$

where \mathbf{f} is a force and $\delta(\mathbf{x})$ is the three-dimensional delta function. The solution to the system of equation (4.8) can be written

$$\mathbf{u}_S(\mathbf{x}; \mathbf{f}) = \mathcal{S}(\mathbf{x}) \cdot \mathbf{f} , \quad (4.10)$$

where $\mathbf{u}_S(\mathbf{x}; \mathbf{f})$ represents the flow velocity at the location \mathbf{x} due to point force \mathbf{f} (or Stokeslet of strength \mathbf{f}) located at the origin and $\mathcal{S}(\mathbf{x})$ is the Stokeslet tensor

$$\mathcal{S}(\mathbf{x}) = \frac{1}{8\pi\mu} \left(\frac{\mathbf{I}}{|\mathbf{x}|} + \frac{\mathbf{x}\mathbf{x}}{|\mathbf{x}|^3} \right) . \quad (4.11)$$

Higher order solutions can be obtained by differentiating the Stokeslet. One such solution is the potential doublet

$$\mathbf{u}_D(\mathbf{x}; \mathbf{g}) = -\frac{1}{2} \nabla^2 \mathbf{u}_S(\mathbf{x}; \mathbf{g}) = \mathcal{D}(\mathbf{x}) \cdot \mathbf{g} , \quad (4.12)$$

where $\mathbf{u}_D(\mathbf{x}; \mathbf{g})$ represents the flow velocity at the location \mathbf{x} due to a potential

doublet of strength \mathbf{g} located at the origin and the potential doublet tensor $\mathcal{D}(\mathbf{x})$ is defined by

$$\mathcal{D}(\mathbf{x}) = \frac{1}{8\pi\mu} \left(\frac{\mathbf{I}}{|\mathbf{x}|^3} - 3 \frac{\mathbf{x}\mathbf{x}}{|\mathbf{x}|^5} \right). \quad (4.13)$$

A potential doublet does not impose any net force on the fluid.

The last fundamental solution introduced here is the rotlet

$$\mathbf{u}_{\mathcal{R}}(\mathbf{x}; \boldsymbol{\tau}) = -\frac{1}{2} \nabla \times \mathbf{u}_{\mathcal{S}}(\mathbf{x}; \boldsymbol{\tau}) = \mathcal{R}(\mathbf{x}) \cdot \boldsymbol{\tau}, \quad (4.14)$$

where $\mathbf{u}_{\mathcal{R}}(\mathbf{x}; \boldsymbol{\tau})$ represents the flow velocity at the location \mathbf{x} due to a point torque $\boldsymbol{\tau}$ (or rotlet of strength $\boldsymbol{\tau}$) located at the origin and the rotlet tensor $\mathcal{R}(\mathbf{x})$ is defined by

$$\mathcal{R}(\mathbf{x}) \cdot \boldsymbol{\tau} = \frac{1}{8\pi\mu} \left(\boldsymbol{\tau} \times \frac{\mathbf{x}}{|\mathbf{x}|^3} \right). \quad (4.15)$$

A more extensive overview of fundamental solutions of Stokes equations can be found in [9, 33].

Hydrodynamics around the head

The head of the swimmer is modeled as a moving prolate spheroid in an otherwise unbounded and quiescent flow. The rigid motion of the head is described by the translational velocity $\mathbf{U}_0 = \dot{\mathbf{R}}_0$ and the rotational velocity $\Omega_0 = \dot{\theta}_0$ at the center O . Integration of the hydrodynamic stress acting on the surface of the head yields the total force \mathbf{F}_0 and torque τ_0 exerted by the fluid on the spheroidal head (see figure 4-1).

An exact analytical solution for the flow around a prolate spheroid can be derived via a singularity method, by distributing fundamental solutions between the two foci of the spheroid. The derivation of this solution can be found in [33]. The fundamental solutions necessary to enforce the no-slip boundary condition at the surface of a translating spheroid is a constant distribution of stokeslets and a parabolic distribution of potential doublets between the two foci on the major axis. For a rotating spheroid, a parabolic distribution of rotlets between the two foci are necessary, as well as higher

order fundamental solutions (see [33]).

Integrating the distribution of stokeslets and rotlets between the two foci yields the expressions for the force \mathbf{F}_0 and torque τ_0 acting on the head as a function of the translational and rotational velocities \mathbf{U}_0 and Ω_0

$$\begin{aligned} \mathbf{F}_0 \cdot \mathbf{t}_0 &= c_0^{\parallel} \mathbf{U}_0 \cdot \mathbf{t}_0 = -\frac{16\pi e^3 L_0 \mu}{-2e + (1 + e^2) \ln(\frac{1+e}{1-e})} \mathbf{U}_0 \cdot \mathbf{t}_0, \\ \mathbf{F}_0 \cdot \mathbf{n}_0 &= c_0^{\perp} \mathbf{U}_0 \cdot \mathbf{n}_0 = -\frac{32\pi e^3 L_0 \mu}{2e + (3e^2 - 1) \ln(\frac{1+e}{1-e})} \mathbf{U}_0 \cdot \mathbf{n}_0, \\ \tau_0 &= c_0^{\circ} \Omega_0 = -\frac{32\pi e^3 (2 - e^2) L_0^3 \mu}{3(-2e + (1 + e^2) \ln(\frac{1+e}{1-e}))} \Omega_0. \end{aligned} \quad (4.16)$$

Furthermore, the fluid velocity $\mathbf{u}_0(\mathbf{x})$ induced by the head at a point \mathbf{x} in the flow can be found by integrating the contribution to the flow from the distribution of singularities between the two foci. The fluid velocity at \mathbf{x} due to the head is given by:

$$\begin{aligned} \mathbf{u}_0(\mathbf{x}) &= -\frac{1}{2} \int_{-1}^{+1} \left(\mathcal{S}(\Delta) + \frac{e^2 L_0^2}{2} (1 - \xi^2) \mathcal{D}(\Delta) \right) \mathbf{F}_0 d\xi \\ &\quad - \frac{3}{4} \int_{-1}^{+1} (1 - \xi^2) \mathcal{R}(\Delta) \tau_0 \hat{\mathbf{z}} d\xi + \int_{-1}^{+1} \mathcal{H}_e(\Delta) \tau_0 \hat{\mathbf{z}} d\xi, \end{aligned} \quad (4.17)$$

where $\Delta = \mathbf{x} - (\mathbf{R}_0 + c\xi \mathbf{t}_0)$ and \mathcal{H}_e is a tensor that arises due to the contribution of higher order fundamental solutions, and is given by the following expression:

$$\begin{aligned} \mathcal{H}_e(\Delta) \tau_0 \hat{\mathbf{z}} &= -\frac{9(1 - e^2)}{32\pi\mu(1 + e^2)} \left(\frac{L_0^2 e^2}{4} (1 - \xi^2)^2 \frac{(\Delta \cdot \mathbf{t}_0) \mathbf{n}_0 + (\Delta \cdot \mathbf{n}_0) \mathbf{t}_0}{|\Delta|^5} \right. \\ &\quad \left. + (1 - \xi^2) \left[1 - \frac{5L_0^2 e^2 (1 - \xi^2)}{4|\Delta|^2} \right] \frac{(\Delta \cdot \mathbf{t}_0)(\Delta \cdot \mathbf{n}_0) \Delta}{|\Delta|^5} \right) \tau_0. \end{aligned} \quad (4.18)$$

Note that for $e = 1$, equation (4.17) reduces to the well-known expression for the creep flow around a sphere, which can be simply modeled as the superposition of a stokeslet, a potential doublet and a rotlet at the center of the sphere.

Hydrodynamics around the flagellum

The flagellum can be modeled as a slenderbody in an unbounded quiescent flow. The flow around slender bodies is the subject of slenderbody theory, which has been thoroughly investigated [8, 41, 42, 83, 89, 157]. In this study, the viscous interactions between the flagellum and the surrounding fluid are modeled using non-local slenderbody theory [89].

In this formulation, fundamental solutions (stokeslets, potential doublets and rotlets) are distributed along the centerline of the slenderbody. Asymptotic matching between the inner expansion of the flow along the centerline and the outer expansion yields an integral equation for the flow around the centerline accurate to order $\mathcal{O}(\kappa)$. No-slip boundary conditions at the surface of the slenderbody can be satisfied by imposing the strength of the distribution of potential doublets to be $r^2/2$ times the strength of the distribution of stokeslets and taking a zero distribution of rotlets. This derivation yields the following integral equation for the velocity along the centerline of the body

$$\mathbf{U} = \mathcal{L}(s) \mathbf{f}(s) - \int_0^{2L} \left[\mathcal{S}(\mathbf{R} - \hat{\mathbf{R}}) \mathbf{f}(\hat{s}) - \left(\frac{\mathbf{I} + \hat{\mathbf{t}}\hat{\mathbf{t}}}{|s - \hat{s}|} \right) \mathbf{f}(s) \right] d\hat{s} \quad (4.19)$$

where $\mathbf{U} = \dot{\mathbf{R}}$ is the velocity at the centerline and $\mathbf{f}(s)$ is the distribution of forces per unit length acting on the flagellum, which is equal and opposite to the distribution of stokeslet per unit length acting on the fluid. $\mathcal{L}(s)$ is a local linear operator, which can be expressed as

$$\mathcal{L}(s) = \frac{1}{8\pi\mu} \left(\ln(\kappa^2 \exp(1)) [\mathbf{I} + 2\mathbf{t}\mathbf{t}] - 2[\mathbf{I} - \mathbf{t}\mathbf{t}] \right). \quad (4.20)$$

Because the motion of the flagellum is constrained to remain planar, $\mathbf{f}(s)$ only has components in the $(\hat{\mathbf{x}}, \hat{\mathbf{y}})$ -plane. This equation has been derived for a slenderbody of radius $\rho(s) = r\sqrt{\frac{(2L-s)s}{L^2}}$. For a complete derivation of this equation see [62].

As with the flow around the head, the fluid velocity $\mathbf{u}_f(\mathbf{x})$ induced by the flagellum at a point \mathbf{x} in the flow can be found by integrating the contribution to the flow due

to the distribution of forces $\mathbf{f}(s)$. Hence, the fluid velocity at \mathbf{x} is given by:

$$\mathbf{u}_f(\mathbf{x}) = - \int_0^{2L} \mathcal{S}(\mathbf{x} - \mathbf{R}) \mathbf{f}(s) ds. \quad (4.21)$$

Hydrodynamic interactions

Hydrodynamic interactions between multiple moving bodies is a dominant aspect of low Reynolds number fluid dynamics. The viscous flow due to a stokeslet for example only decays as $1/r$ (see equation (4.11)) and therefore the motion of one body is expected to depend on the motion of the other bodies. In our case, this is particularly worrisome as the head and the flagellum are attached to one another and cannot be treated separately as moving in an unbounded quiescent flow.

In the present study, hydrodynamic interactions are taken into account by using Faxén's laws, which relate the hydrodynamic forces acting on a body to both the motion of the body and the no longer quiescent ambient flow \mathbf{u}_∞ . Faxén's laws for the head, which is modeled as a prolate spheroid, can be found in [70] and to the first order, they take the following form

$$\begin{aligned} \mathbf{U}_0 &= \left(\frac{1}{c_0^\parallel} \mathbf{t}_0 \mathbf{t}_0 + \frac{1}{c_0^\perp} \mathbf{n}_0 \mathbf{n}_0 \right) \mathbf{F}_0 + \mathbf{u}_\infty(\mathbf{R}_0) + \frac{1}{3!} (D^2 \mathbf{u}_\infty)_{\mathbf{R}_0} + \mathcal{O}(L_0^4), \\ \Omega_0 \hat{\mathbf{z}} &= \frac{1}{c_0^\ominus} \tau_0 \hat{\mathbf{z}} + \frac{1}{L_0^2 (2 - e^2)} (\square \times \mathbf{u}_\infty)_{\mathbf{R}_0} + \mathcal{O}(L_0^4). \end{aligned} \quad (4.22)$$

Here D^2 and \square are the differential operators given by

$$D^2 = L_0^2 \left(\frac{\partial^2}{\partial x^2} + e^2 \frac{\partial^2}{\partial y^2} + e^2 \frac{\partial^2}{\partial y^2} \right), \quad (4.23)$$

$$\square = L_0^2 \left(\hat{\mathbf{x}} \frac{\partial}{\partial x} + e^2 \hat{\mathbf{y}} \frac{\partial}{\partial y} + e^2 \hat{\mathbf{z}} \frac{\partial}{\partial y} \right), \quad (4.24)$$

where \mathbf{t}_0 is assumed to be colinear with $\hat{\mathbf{x}}$ and \mathbf{n}_0 is assumed to be colinear with $\hat{\mathbf{y}}$ to simplify of notation. As expected, Faxén's laws reduce to the previously derived equations (4.16) for a quiescent flow when $\mathbf{u}_\infty = \mathbf{0}$. For the slender flagellum, Faxén's

laws simply take the form:

$$\mathbf{U} = \mathcal{L}(s) \mathbf{f}(s) - \int_0^{2L} \left[\mathcal{S}(\mathbf{R} - \hat{\mathbf{R}}) \mathbf{f}(\hat{s}) - \left(\frac{\mathbf{I} + \hat{\mathbf{t}}\hat{\mathbf{t}}}{|s - \hat{s}|} \right) \mathbf{f}(s) \right] d\hat{s} + \mathbf{u}_\infty(\mathbf{R}). \quad (4.25)$$

Hydrodynamic interactions between the spheroidal head and the slender flagellum are taken into account by considering that the ambient flow around the head is the flow induced by the flagellum \mathbf{u}_f given by equation (4.21). Similarly the ambient flow around the flagellum is considered to be the flow induced by the head \mathbf{u}_0 given by equation (4.17).

4.2.3 Governing equations

Dynamics of the swimmer

The expressions for the flow induced by the flagellum \mathbf{u}_f (equation (4.21)) and by the head \mathbf{u}_0 (equation (4.17)) are substituted respectively into equations (4.22) and (4.25) as the ambient flow. This substitution yields a system of equations governing the hydrodynamics around the swimmer:

$$\begin{aligned} \mathbf{U} = & \mathcal{L}(s) \mathbf{f}(s) - \int_0^{2L} \left[\mathcal{S}(\mathbf{R} - \hat{\mathbf{R}}) \mathbf{f}(\hat{s}) - \left(\frac{\mathbf{I} + \hat{\mathbf{t}}\hat{\mathbf{t}}}{|s - \hat{s}|} \right) \mathbf{f}(s) \right] d\hat{s} \\ & - \frac{1}{2} \int_{-1}^{+1} \left(\mathcal{S}(\Delta) + \frac{e^2 L_0^2}{2} (1 - \xi^2) \mathcal{D}(\Delta) \right) \mathbf{F}_0 d\xi \\ & - \frac{3}{4} \int_{-1}^{+1} (1 - \xi^2) \mathcal{R}(\Delta) \tau_0 \hat{\mathbf{z}} d\xi + \int_{-1}^{+1} \mathcal{H}_e(\Delta) \tau_0 \hat{\mathbf{z}} d\xi, \end{aligned} \quad (4.26)$$

$$\begin{aligned} \mathbf{U}_0 = & \left(\frac{1}{c_0^\parallel} \mathbf{t}_0 \mathbf{t}_0 + \frac{1}{c_0^\perp} \mathbf{n}_0 \mathbf{n}_0 \right) \mathbf{F}_0 - \int_0^{2L} \mathcal{S}(\Lambda) \mathbf{f}(s) ds \\ & - \frac{(1 - e^2) L_0^2}{48\pi\mu} \int_0^{2L} \left(\left[\frac{-1}{|\Lambda|^3} + \frac{3(\Lambda \cdot \mathbf{t}_0)^2}{|\Lambda|^5} \right] \mathbf{I} - \frac{6\Lambda \cdot \mathbf{t}_0}{|\Lambda|^5} (\mathbf{t}_0 \Lambda + \Lambda \mathbf{t}_0) \right. \\ & \left. + \frac{2\mathbf{t}_0 \mathbf{t}_0}{|\Lambda|^3} + \left[\frac{-3}{|\Lambda|^5} + \frac{15(\Lambda \cdot \mathbf{t}_0)^2}{|\Lambda|^7} \right] \Lambda \Lambda \right) \mathbf{f}(s) ds, \end{aligned} \quad (4.27)$$

$$\begin{aligned} \Omega_0 = & \frac{1}{c_0^\ominus} \tau_0 + \frac{1}{8\pi(2 - e^2)\mu} \int_0^{2L} \left((1 + e^2) \frac{\hat{\mathbf{z}} \times \Lambda}{|\Lambda|^3} \right. \\ & \left. + 3(1 - e^2)(\Lambda \cdot \mathbf{t}_0)(\Lambda \cdot \mathbf{n}_0) \frac{\Lambda}{|\Lambda|^5} \right) \cdot \mathbf{f}(s) ds, \end{aligned} \quad (4.28)$$

where $\Delta = \mathbf{R} - (\mathbf{R}_0 + c\xi\mathbf{t}_0)$ and $\Lambda = \mathbf{R}_0 - \mathbf{R}$.

This system of equations is closed by imposing that the swimmer remains in equilibrium at each time. The force and torque equilibrium equations are given by:

$$\mathbf{F}_0 + \int_0^{2L} \mathbf{f}(s)ds = \mathbf{0} , \quad (4.29)$$

$$\tau_0 \hat{\mathbf{z}} + \int_0^{2L} (\mathbf{R} - \mathbf{R}_0) \times \mathbf{f}(s)ds = \mathbf{0} . \quad (4.30)$$

The velocity decomposition in equation (4.4) is introduced in the integral equation (4.26) and equations (4.26)–(4.30) yield a system of equations which can be solved for \mathbf{U}_0 , Ω_0 , \mathbf{F}_0 , τ_0 and the distribution of hydrodynamic force \mathbf{f} , given the deformation \mathbf{U}^{def} .

Rate of work

Using the previously defined notation, the rate of work exerted against viscous forces given by equation (2.7) takes a simple form for uniflagellates:

$$\Phi = \mathbf{F}_0 \cdot \mathbf{U}_0 + \tau_0 \cdot \Omega_0 + \int_{s=0}^{2L} \mathbf{f}(s) \cdot \mathbf{U}(s)ds \quad (4.31)$$

4.2.4 Numerical approach

The integral equations (4.26)–(4.30) governing the motion of the swimmer are solved numerically and the numerical approach is briefly described here.

Spatial discretization

A first order geometrical representation of the flagellum is obtained by discretizing the inextensible slender rod into a regular grid of N inextensible linear elements. Each element has a half length of $ds = \frac{L}{N}$ and can be defined as the segment $[s_i, s_{i+1}]$, where $s_i = 2ids$ is the arc-length of the location of the node between segment $i - 1$ and segment i for $i = 0, \dots, N$. The location of the center of each segment is given by the position vector $\mathbf{R}_i = (x_i, y_i)$ and the corresponding arc-length $\sigma_i = (2i - 1)ds$ for

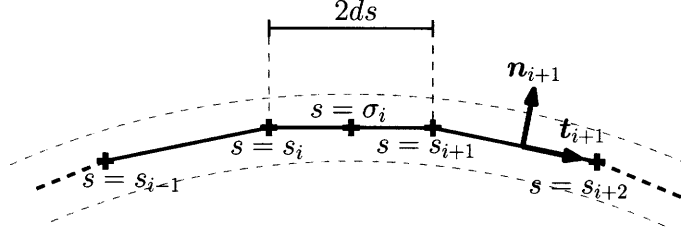


Figure 4-2: Spatial discretization of the flagellum

$i = 1, \dots, N$. A representation of this spatial discretization can be found in figure 4-2. We can further define \mathbf{t}_i , \mathbf{n}_i and θ_i as the tangential vector, normal vector and angle between the $\hat{\mathbf{x}}$ -axis and \mathbf{t}_i at arc-length σ_i , such that $\mathbf{t}_i = (\cos \theta_i, \sin \theta_i)$. The position vector \mathbf{R}_0 and orientation $\mathbf{t}_0 = (\cos \theta_0, \sin \theta_0)$ of the head are known.

For this discretization, the position vector \mathbf{R}_i at σ_i can be easily computed from numerical integration of the Serret–Frenet equations (4.1),

$$\begin{aligned} \theta_{i+1} &= \theta_i + 2 ds \gamma(s_i) , \\ \mathbf{R}_{i+1} &= \mathbf{R}_i + ds (\mathbf{t}_{i+1} + \mathbf{t}_i), \end{aligned} \quad (4.32)$$

with the conditions at $s = 0$

$$\begin{aligned} \theta_1 &= \theta_0 + 2 ds \gamma(s_0) , \\ \mathbf{R}_1 &= \mathbf{R}_0 + ds \mathbf{t}_1 + L_0 \mathbf{t}_0. \end{aligned} \quad (4.33)$$

Let \mathbf{U}_i represent the velocity at the center σ_i of the i -th element. The velocity \mathbf{U}_i can be written $\mathbf{U}_i = \mathbf{U}_i^{\text{rig}} + \mathbf{U}_i^{\text{def}}$ and represented numerically. The rigid body motion only depends on the motion of the head (\mathbf{U}_0, Ω_0) and simply takes the form

$$\mathbf{U}_i^{\text{rig}} = \mathbf{U}_0 + \Omega_0 \hat{\mathbf{z}} \times (\mathbf{R}_i - \mathbf{R}_0) . \quad (4.34)$$

The deformation velocity is fully defined by the time variations of the curvature and can be computed by numerical integration of the time derivatives of the Serret–Frenet

equations

$$\begin{aligned}\dot{\theta}_{i+1} &= \dot{\theta}_i + 2 ds \dot{\gamma}(s_i) , \\ \dot{\mathbf{U}}_{i+1}^{\text{def}} &= \dot{\mathbf{U}}_i^{\text{def}} + ds (\dot{\theta}_{i+1} \mathbf{n}_{i+1} + \dot{\theta}_i \mathbf{n}_i),\end{aligned}\quad (4.35)$$

with the conditions at $s = 0$

$$\begin{aligned}\dot{\theta}_1 &= 2ds \dot{\gamma}(s_0) , \\ \dot{\mathbf{R}}_1 &= ds \dot{\theta}_1 \mathbf{t}_1 .\end{aligned}\quad (4.36)$$

Finally, let \mathbf{f}_i be the hydrodynamic force per unit length at the center σ_i of the i -th element. We assume that the distribution of force is constant over each segment and define $\mathbf{F}_i = 2\mathbf{f}_i ds$ the total hydrodynamic force on the i -th segment.

Numerical resolution

With this discretization, the system of equations governing the motion of the swimmer can be solved numerically. The integral equation (4.26) is solved using a simple collocation scheme, resulting in a point matching solution at the collocation points σ_i . Equation (4.26) can then be written in discrete form:

$$\mathcal{A}_i \begin{pmatrix} \mathbf{U}_0 \\ \Omega_0 \end{pmatrix} - \mathcal{L}_i \mathbf{F}_i + \sum_{j=1}^N (\mathcal{M}_{ij} \mathbf{F}_j - \mathcal{N}_{ij} \mathbf{F}_i) - \mathcal{V}_{i0} \mathbf{F}_0 - \mathcal{W}_{i0} \tau_0 = -\mathbf{U}_i^{\text{def}} , \quad (4.37)$$

where \mathcal{A}_i is a 2×3 matrix, \mathcal{L}_i , \mathcal{M}_{ij} , \mathcal{N}_{ij} , \mathcal{V}_{i0} are 2×2 matrices and \mathcal{W}_{i0} is a 2×1 matrix. Expression for these matrices can be found in appendix B.

Similarly, equations (4.27,4.28) can be discretized

$$\mathbf{U}_0 - \mathcal{L}_0 \mathbf{F}_0 + \sum_{j=1}^N \mathcal{M}_{0j} \mathbf{F}_j = \mathbf{0}, \quad (4.38)$$

$$\Omega_0 - \vartheta_0 \tau_0 + \sum_{j=1}^N \eta_{0j} \mathbf{F}_j = 0, \quad (4.39)$$

where \mathcal{L}_0 is a 2×2 matrix, \mathcal{M}_{0j} a 2×2 matrix, ϑ_0 a 1×1 and η_{0j} a 1×2 .

Additionally, the equilibrium equations (4.29,4.30) can be written

$$\begin{pmatrix} \mathbf{F}_0 \\ \tau_0 \end{pmatrix} + \sum_{j=1}^N \mathcal{A}_j^T \mathbf{F}_j = \mathbf{0}. \quad (4.40)$$

Finally, the rate of work given by equation (4.31) can be evaluated numerically as:

$$\Phi = \mathbf{F}_0 \cdot \mathbf{U}_0 + \tau_0 \cdot \Omega_0 + \sum_{j=1}^N \mathbf{F}_j \cdot \mathbf{U}_j. \quad (4.41)$$

Equations (4.37–4.40) form a linear system of $2N+6$ equations in $2N+6$ unknowns ($\mathbf{U}_0, \Omega_0, \mathbf{F}_0, \tau_0, \mathbf{F}_1, \dots, \mathbf{F}_N$), which can be inverted and solved. The position (\mathbf{R}_0, θ_0) of the swimmer during the stroke is computed by time integration of the rigid body motion (\mathbf{U}_0, Ω_0) using the procedure described in section 2.3.3. The square root of the rate of work Φ is also integrated in time, as required by the computation of the minimal work W_{\min} given by equation (2.12). The motion of the swimmer is computed for one entire stroke period T , after which the total distance travelled $\ell_0 = |\mathbf{R}_0(T) - \mathbf{R}_0(0)|$, the average velocity $U_0 = \frac{\ell_0}{T}$ and the minimal work W_{\min} can be computed.

4.2.5 Optimization procedure

Stroke parameterization

As discussed in section 2.3.4, the nonlinear optimization approach requires a parameterization of the stroke kinematics through a finite set of parameters. The deformation of the swimmer is fully described by the curvature function $\gamma(s, t)$ for arc-lengths ranging from $s = 0$ to $s = 2L$ and times between $t = 0$ and $t = T$. As the deformation of the swimmer is periodic, we further know that the curvature distribution along the tail $\gamma(s, 0)$ at time $t = 0$ is the same as the distribution $\gamma(s, T)$ at time $t = T$.

Therefore, we seek to describe a function of two variables with a finite number of deformation parameters. This parameterization should be able to represent all

possible strokes and thus be as general as possible. In this study, we extend the Fourier based representation developed in the case of the three-link swimmer, which proved to be satisfactorily efficient and versatile. At each point along the flagellum, the curvature is a periodic function, which can be written as a Fourier series and represented by its Fourier coefficients. Given the spatial discretization of the flagellum introduced earlier, we would ideally represent the curvature at each node of arc-length s_i by a set of corresponding Fourier coefficients. However, because the number N of segments in the spatial discretization of the flagellum typically ranges from 50 to 200, this leads to an excessive number of deformation parameters.

In order to avoid the computational limitations concomitant with an extremely large number of deformation parameters, we define a coarser discretization for the curvature made of a regular grid of N_γ elements, where N_γ typically ranges from 5 to 20. The curvature is imposed at the nodes of this coarse grid defined by their arc-length $\mathbf{s}_p = p \frac{2L}{N_\gamma}$ for $p = 0, 1, \dots, N_\gamma$. At each of these nodes, the curvature is expanded in a Fourier series

$$\gamma(\mathbf{s}_p, t) = a_0^{s_p} + \sum_{n=1}^{\infty} \left(a_n^{s_p} \cos\left(\frac{2\pi}{T}nt\right) + b_n^{s_p} \sin\left(\frac{2\pi}{T}nt\right) \right). \quad (4.42)$$

The curvature $\gamma(s_i, t)$ at each of the N nodes s_i for $i = 0, 1, \dots, N-1$ is deduced from a cubic spline interpolation of the values at the $N_\gamma + 1$ nodes \mathbf{s}_p . This interpolation guarantees that the curvature is twice continuously differentiable. If we only retain the first k terms in the Fourier development, the curvature can be parameterized by a set of $(2k + 1)(N_\gamma + 1)$ Fourier coefficients, which form the vector of deformation parameters.

Swimming efficiency

We now define the exact expression for the swimming efficiency, used in this analysis. The parameter which remains to be determined is the drag coefficient α of the equivalent swimmer. Recall from chapter 2 that the efficiency represents the fraction of the total energy expense effectively used towards a given objective. This definition

applied to uniflagellates introduces the idea of a *payload*.

On the one hand, if the swimmer has no head and the objective is to move the flagellum only, the entire flagellum can be considered to be the *payload*. Consider a stroke for which the swimmer moves a distance ℓ_0 at an average speed of U_0 . The numerator in the efficiency then represents the work required to move the straightened flagellum over the same distance ℓ_0 at the same average speed U_0 . The coefficient α is thus taken to be equal to the drag coefficient of a slender rod of length $2L$, which we have already seen in the study of the three-link swimmer. Thus, the swimming efficiency takes the same form as in the three-link case:

$$\mathcal{E} = \frac{c^{\parallel} U_0 \ell_0}{W_{\min}}. \quad (4.43)$$

On the other hand, if the swimmer has a head and the objective is to move the material included inside the head only, the head can be considered to be a *payload*. In this case, the flagellum can be considered to be a *deadload*. Similarly to the case of a single flagellum, the numerator in the efficiency then represents the work required to move only the payload over the same distance ℓ_0 at the same average speed U_0 . Here, the coefficient α in the expression of the efficiency corresponds to the drag coefficient of the equivalent payload and is taken to be equal to the drag coefficient of a sphere of same volume. The volume included inside the head is equal to $V = \frac{4}{3}\pi e^2 L_0^3$ and we thus define the equivalent radius of the head L_0^{eq} as the radius of the sphere of same volume $L_0^{\text{eq}} = e^{2/3} L_0$. With this definition, the drag coefficient α_0 of the equivalent head takes the form $\alpha_0 = 6\pi\mu L_0^{\text{eq}}$ and the swimming efficiency can be written:

$$\mathcal{E} = \frac{\alpha_0 U_0 \ell_0}{W_{\min}}. \quad (4.44)$$

This general expression for the efficiency of uniflagellates allows us to compare swimmers, whose heads include an identical volume but have different shapes.

Zero net rotation strokes

Similarly to the three-link study, the zero net rotation condition can be imposed via two different methods. The first approach is general and does not restrict the space of allowed strokes. In this case, we impose the condition through the same penalty scheme introduced in section 3.2.4. In this case, the efficiency is weighted with a prefactor, which decreases the efficiency for a non-zero net rotation at the end of the stroke.

The second approach is to impose the zero net rotation condition by adding a symmetry constraint directly on the stroke itself. This simply means that the curvature along the tail at time $t + \frac{T}{2}$ is always opposite to the curvature at time t :

$$\gamma(t + \frac{T}{2}, s) = -\gamma(t, s) \text{ for all } t \in [0, \frac{T}{2}] \text{ and } s \in [0, 2L]. \quad (4.45)$$

It can be readily seen that such strokes will always lead to a zero net rotation at the end of a stroke, for the same reason developed in the context of the three-link swimmer in section 3.3.1. This condition is easily translated into the discretization of the curvature required by the stroke parameterization, by imposing

$$\begin{aligned} a_{2p}^{s_n} &= 0 \text{ for } p = 0, 1, 2, 3, \dots \text{ and } n = 1, 2, \dots, N_\gamma \\ b_{2p}^{s_n} &= 0 \text{ for } p = 1, 2, 3, \dots \text{ and } n = 1, 2, \dots, N_\gamma. \end{aligned} \quad (4.46)$$

This approach constraints the space of possible strokes, but divides the number of design variables by a factor of two, which represents a considerable gain.

For all geometries investigated here, optimal strokes were found to be symmetrical. There were no significant differences between optimal strokes computed using the two different methods of imposing the zero net rotation condition. The second method which implicitly assumes the stroke to be symmetric leads to shorter computation times and was therefore used in all of the following computations.

4.3 Validation of the model

We now seek to use our model for low Reynolds number locomotion of unflagellated swimmers and the related optimization approach in order to find stroke kinematics that optimize swimming efficiency. The first problem under investigation is that of a single-tail swimmer, which has no head and is only made of a deformable flagellum. In this case, the expression for the swimming efficiency is given by equation (4.43). This problem is particularly interesting because it has been previously investigated analytically and consequently provides a valuable testbed for our locomotion model and optimization procedure. We will first briefly describe the analytical solution to this problem which we will then compare to the results given by our model.

4.3.1 Analytical optimal for a single-tail swimmer

A detailed derivation of the analytical solution of the optimal stroke for a single-tail swimmer can be found in *Mathematical Biofluidynamics* by J. Lighthill [99]. The outline of this derivation is presented here, along with a summary of all assumptions.

Consider a single-tail swimmer of length $2L$. The stroke is explicitly assumed to consist of a periodic traveling wave propagating along the flagellum. Let λ be the wavelength measured in the $\hat{\mathbf{x}}$ -direction, and Λ the wavelength measured along the curved body of the swimmer. Notations relevant to this particular problem are illustrated in figure 4-3, while all other notation remains the same as that introduced in section 4.2.1. The geometric parameter $\omega = \lambda/\Lambda$ characterizes the apparent contraction in the length of the swimmer, due to the waveform. The period of the stroke T is the time required for the waveform to propagate a distance λ in the frame of reference attached to the swimmer. The distance traveled by the swimmer over one period is ℓ_0 . We further define the swimming velocity of the swimmer $U_0 = \ell_0/T$, as well as the wave velocity in the frame of reference attached to the swimmer $V_0 = \lambda/T$.

In the global frame of reference, the single tail is explicitly assumed to only move along the periodic waveform propagating in the $\hat{\mathbf{x}}$ -direction at velocity $V_0 - U_0$ and to swim at a constant velocity of U_0 . The velocity V_0 is prescribed and characterizes how

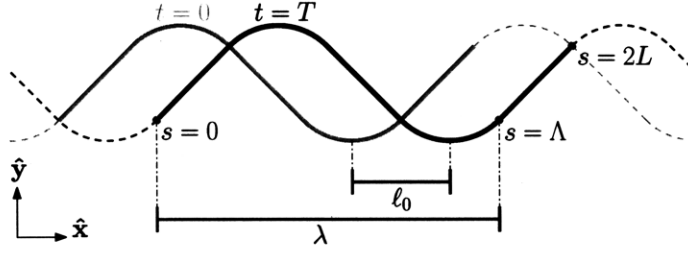


Figure 4-3: Schematic of single-tail swimmer with notation used in the analytical derivation of optimal stroke kinematics.

fast the swimmer deforms. The swimming velocity U_0 is unknown, but the complete motion of the swimmer is known as a function of U_0 and V_0 . While these assumption for the motion of the swimmer are accurate for an infinitely long swimmer, for which the waveform is repeated an infinite number of times, they are not exactly correct for a swimmer of finite length, for which the swimmer might have some “up and down” motion along the \hat{y} -axis during the stroke.

In this analysis, the hydrodynamic forces acting on the swimmer are modeled using resistive force theory. Hence the force per unit length $\mathbf{f}(s)$ acting on the fiber only depends on the local velocity $\mathbf{U}(s)$ and the drag coefficients in the tangential and normal directions, which are further assumed to be respectively equal to c^{\parallel} and c^{\perp} . The local velocity $\mathbf{U}(s)$ can be fully expressed in terms of s , U_0 and V_0 which yields an expression for the hydrodynamic force per unit length as well. The swimming velocity U_0 can be found by integrating the hydrodynamic force over the length of the tail and imposing the equilibrium condition given by equation (4.29). This swimming velocity yields the following expression

$$\frac{U_0}{V_0} = \frac{(1-v)(1-r_K)}{1-v-vr_K}, \quad (4.47)$$

where $r_K = \frac{c^{\parallel}}{c^{\perp}}$ is the ratio of drag coefficients and $v = \frac{1}{T} \int_0^{2L} \cos(\theta(s))^2 ds$ is a geometric parameter characterizing the waveform.

Additionally, the work exerted against viscous forces can be easily calculated from equation (4.31). Finally, an expression for the swimming efficiency \mathcal{E} — which depends

on ω , v and r_K — in equation (4.43) can be found. From a simple minimization argument, one can deduce that the swimming efficiency is minimized when $\omega^2 = v$ and the cosine of the tangential vector $\mathbf{t}(s) \cdot \hat{\mathbf{x}} = \cos \theta(s)$ is constant all along the tail except for a set of measure zero. This implies that the waveform has the shape of a “saw-tooth”, or a triangular wave, made of connected linear segments, which make an angle of constant cosine with the swimming direction, see figure 4-5(a). The value for the optimal efficiency \mathcal{E} , the swimming velocity U_0 and the angle Ψ_0 between the tangential unit vector to the centerline take a simple analytical form:

$$\begin{aligned}\mathcal{E} &= (1 - \sqrt{r_K})^2 , \\ U_0 &= (1 - \sqrt{r_K}) V_0 , \\ \Psi_0 &= \cos^{-1} \sqrt{\frac{1}{1 + \sqrt{r_K}}} .\end{aligned}$$

As discussed earlier, in the limit of infinitely slender swimmers for which resistive force theory can be used, the ratio of drag coefficient r_K is equal to 0.5 for which $\mathcal{E} = 0.0858$, $U_0 = 0.293 V_0$ and $\Psi_0 = 40.06^\circ$.

4.3.2 Comparison between analytical and numerical optimal

Our model for the swimmer together with the optimization approach is now applied to the same problem of finding optimal strokes for a single-tail swimmer. One should keep in mind that the formulation developed in section 4.2 is much more general than the optimization problem solved analytically in the previous section. The “saw-tooth”-wave is the optimal stroke, among strokes which propagate a periodic waveform along the tail. Our model for the swimmer allows for propagating waves, but is by no means limited to this class of strokes. It is general enough to represent any possible 2D deformation of the swimmer.

In order to investigate the space of all possible strokes, the optimization procedure is started from a variety of different initial guesses, as was done for the three-link swimmer. In this case, strokes can no longer be simply visualize as closed curves in

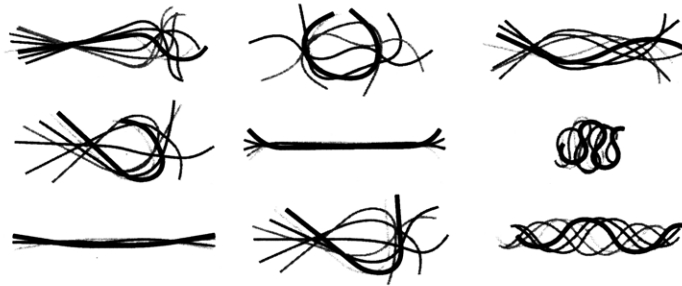


Figure 4-4: Representation of typical initial guesses for the optimization of the single-tail swimmer.

a two-dimensional space, and the search could not be done as systematically as in the three-link swimmer case. Figure 4-4 represents a sample of initial guesses, which is representative of the diversity of strokes used as initial guesses. Most of them do not resemble traveling waves, some exhibit large deformations other only very small deflections around the straightened position. Finally some of them are non-symmetric in time as defined in section 4.2.5

For all of the initial strokes depicted in figure 4-4 and all the initial guesses that are not represented here, the optimization procedure converged to the same optimal stroke. This solution is represented in figure 4-5(b). The optimal stroke found by the optimization routine is in fact a periodic traveling wave propagating along the single tail, whose waveform approaches the “saw-tooth” solution. The edges of the waveform are rounded due to limitations in the spatial discretization of the slender rod. Nevertheless, the waveform can be seen to approach the characteristic form of a sequence of connected straight linear segments. Figure 4-5(c) is a superposition of snapshots of the curvature distribution along the tail. It is made of narrow peaks of high curvature (where the centerline changes direction with a small radius of curvature) connected by region of curvature close to zero (characteristic of straight segments). This curvature distribution converges to that of a “saw-tooth” which is a superposition of delta functions and is zero everywhere except at the discontinuities. Similarly, figure 4-5(d) represents the angle $\theta(s)$ along the tail. The angle distribution of the computed solution approaches the characteristic “square-wave” shape of the analytical solution. The values for the swimming efficiency, the swimming velocity

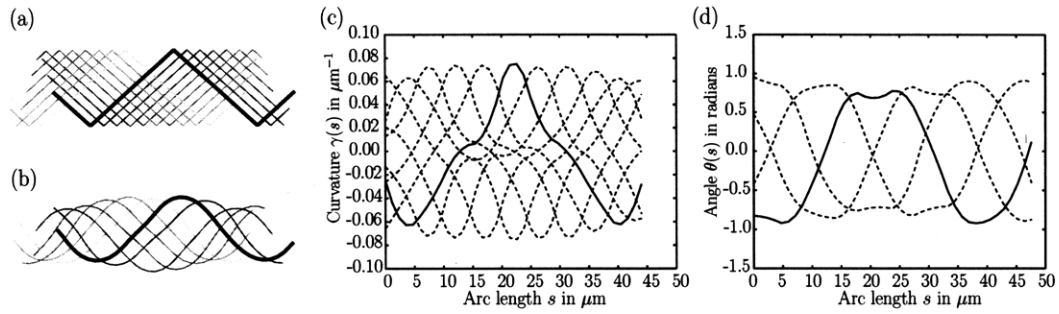


Figure 4-5: (a) Analytical solution for an optimal single-tail swimmer of periodic waveform. (b) Computed optimal single-tail swimmer. (c-d) Timeshots of the curvature distribution γ and angle θ as a function of the arc-length for the computed optimal kinematics of a single-tail swimmer.

and the characteristic angle of the waveform are very similar to those of the analytical optimal saw-tooth. These values are reported in table 4.1 and can be compared to the analytical results.

Two observations can be made following this study. Firstly, our representation of locomotion and the associated optimization for flagellated swimmers are validated by the results of this study. For all initial trial strokes, the optimization procedure converged towards a well defined solution, which also was the case in the three-link study. Furthermore, the solution found corresponds to a stroke, which has been shown to be optimal among all strokes propagating periodic waves along a single tail. These observations confirm the versatility, consistency and robustness of our method. Secondly, we were not able to find any stroke with a swimming efficiency higher than the previously suggested “saw-tooth”-stroke, as the procedure converged to the same solution regardless of the initial guess. Recall that a broad array of initial guesses were tested: mostly non-traveling-wave-like strokes of small and large amplitudes, traveling-wave-like strokes of various waveforms, and asymmetrical strokes. This strongly suggests that the “saw-tooth” stroke, while it cannot be rigorously proven to be a global optimum, is at least a much more general optimum than previously demonstrated.

	\mathcal{E}	U_0/V_0	Ψ_0
Analytical solution	0.0858	0.293	40.06°
Computed solution	0.0829	0.264	41.00°

Table 4.1: Analytical and computed characteristic values of the “saw-tooth” optimal wave.

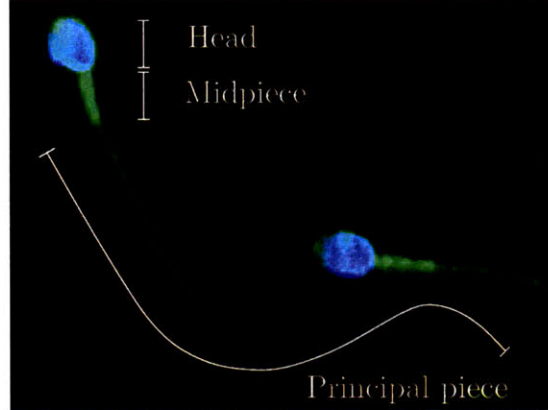


Figure 4-6: Fluorescence microscopy image of human spermatozoa adapted from Neuhaus *et al.* [113] representing the different parts of a sperm cell.

4.4 Optimal stroke kinematics for unflagellates

In this section, we investigate efficient unflagellated swimmers and focus on their stroke kinematics. Unflagellated swimmers, which are modeled in this study, resemble sperm cells (see figure 4-1). It should be noted however, that the geometry of our model swimmer is a rather simplified version of real sperm. Natural sperm cells can be divided in three sections: the head, the midpiece and the tail, which is sometimes called the principal piece (see figure 4-6). The midpiece is the region at the base of the flagellum, which is thicker than the flagellum and connects the tail to the head. One major omission in our geometrical model is the absence of the midpiece. In this analysis, we will always refer to the principal piece plus the midpiece as the tail of the swimmer.

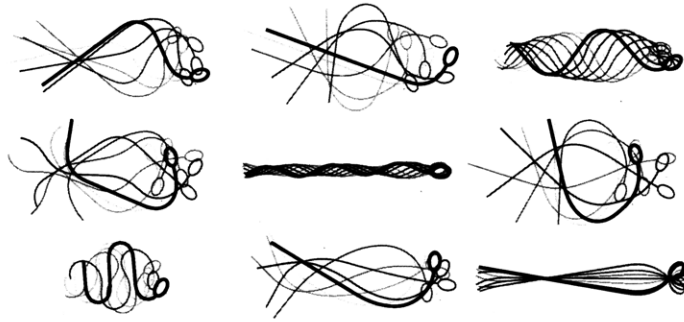


Figure 4-7: Representation of typical initial strokes for the optimization of unflagellated swimmers.

4.4.1 Description of the optimal stroke kinematics

Our model swimmer is prototypical for a sperm cell of a primate and has the following dimensions: head length $2L_0 = 4.5 \mu\text{m}$, head width $2eL_0 = 3.0 \mu\text{m}$, tail (principal piece plus midpiece) length $2L = 50 \mu\text{m}$ and tail radius $r = 0.150 \mu\text{m}$. Optimal strokes are found following the same optimization procedure used previously, starting from a variety of initial guesses. Figure 4-7 represents a sample of the initial guesses used in this study. Most of them do not have the structure of a traveling wave. The optimization procedure was started from both very small amplitude strokes as well as large amplitude strokes.

The main result from this optimization search is that propagation of a waveform from the base of the head down the tail of the swimmer is an optimal stroke. In fact, as with the single-tail swimmer, the optimization always converges to a traveling wave solution, regardless of the initial stroke. No other strokes were found to be optimal, even locally. The optimal stroke for the model swimmer is represented in figure 4-9(d). The resemblance between the optimal computed stroke kinematics and beating patterns exhibited by sperm cells is both striking and intriguing. Also, our investigation suggests that in general organisms, which propel by propagating waves along their tails, are indeed using an optimal swimming mode in terms of the swimming efficiency, regardless on the specifics of the waveform.

While an in-depth quantitative analysis of the computed waveform and comparison with biological data is difficult to achieve, several general comments can be

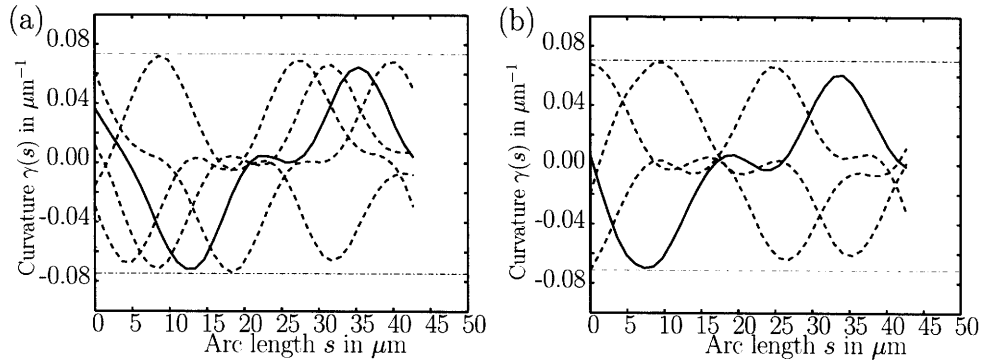


Figure 4-8: (a) Timeshots of the curvature distribution γ as a function of the arc-length for the optimal stroke of a unflagellated swimmer with a head of eccentricity of 0.67. (b) Same for a head of eccentricity 0.2.

made. Global characteristics of the optimal stroke, which was found, are in agreement with previous studies, which investigated only prescribed sinusoidal traveling waves [74, 118]. The number of waveforms for the optimal kinematics is about one and the ratio of the amplitude of the wave to the wavelength is also about one, which is in agreement with [74]. The time variations of curvature along the length of the tail for the optimal stroke of our model unflagellate are represented in figure 4-8(a). As for the single-tail swimmer, figure 4-8(a) shows that the waveform is due to a local region of high curvature, which propagates down the tail. It is interesting to further note that in this case the amplitude or maximum curvature decreases as the wave propagates, although only slightly. This can also be seen in the representation of the stroke, figure 4-9, where the bent region of the tail closer to the head has a slightly larger curvature than the bent region at the free end to the tail. This decrease in amplitude will be further investigated as we look at the influence of the shape of the head on the optimal waveform in the next section.

4.4.2 Influence of head shape on optimal stroke kinematics

One parameter, which significantly affects the structure of the optimal stroke and its associated swimming efficiency is the shape of the head. In this study, the only parameters describing the shape of the head is the eccentricity of the head. When

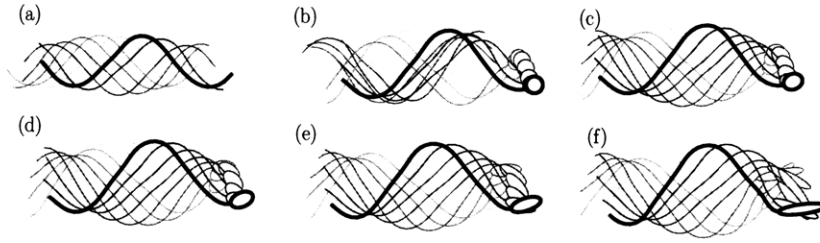


Figure 4-9: Representation of optimal stroke kinematics for: (a) single-tail swimmer, (b) unflagellated swimmer with eccentricity for the head of $e = 1.0$, (c) $e = 0.8$, (d) $e = 0.6$, (e) $e = 0.4$, (f) $e = 0.2$.

the eccentricity is equal to $e = 1$, the head is a sphere and it becomes a more slender ellipsoid as the eccentricity e is decreased to zero. Here we vary e and analyze its effect on the waveform and the efficiency. As e is varied, the volume inside the head is kept constant in order to still compare efficiencies of equivalent swimmers, which can carry the same volume of payload. For values of the eccentricity ranging from $e = 1.0$ to $e = 0.1$, the volume inside the head is kept equal to that of the model swimmer in section 4.4.1 ($\sim 21.20 \mu\text{m}^3$) and the optimal stroke is computed started from a small amplitude initial guess.

In the case of a spherical head, the optimal waveform is similar to the propagating periodic wave exhibited by the single-tail swimmer. As the eccentricity is decreased, the waveform seems to lose its periodicity and the amplitude of the bend in the curved section of the tail decreases as the wave propagates towards the free end of the tail. Figure 4-9(a-f) shows representations of the optimal strokes found for unflagellate swimmers with heads of a varying eccentricity. This change of waveform as the wave propagates can be seen in figure 4-8. Furthermore, the decrease in curvature as the wave travels is more pronounced for a head of eccentricity $e = 0.2$ (figure 4-8(b)) than for a head of eccentricity $e = 0.67$ (figure 4-8(a)).

This “loss” of curvature can be more easily represented by considering what will be called the total curvature Γ . We define the total curvature Γ associated with a bending section of the central line as the integral along the centerline of the curvature over this bending section. This integral simply corresponds to the angle Γ representing the change in the direction of the centerline due to the bending section. Figure 4-10

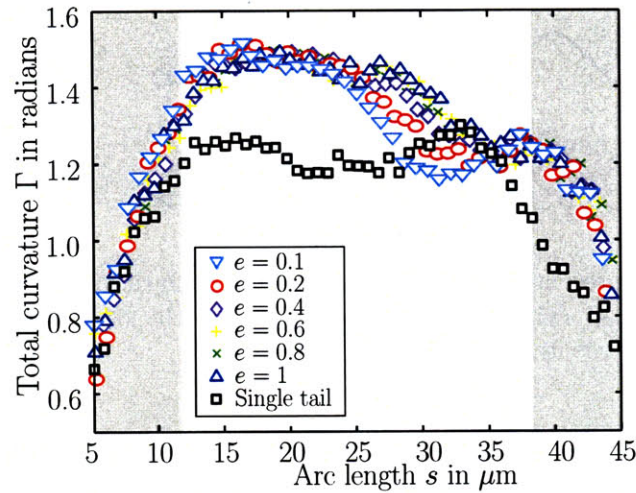


Figure 4-10: Variation of the total curvature Γ as the wave propagates down the flagellum for: the single-tail swimmer, unflagellated swimmers with eccentricity for the head of $e = 1.0$, $e = 0.8$, $e = 0.6$, $e = 0.4$ and $e = 0.2$. Shaded area represent regions for which end effects cannot be neglected in the computation of the total curvature.

represents the change of total curvature Γ as the bending section propagates along the tail. In order to compute these variations, we simply consider a particular section of the waveform as the centerline starts to bend at the base of the head. Once the bending region has fully developed, it can be easily followed by tracking the peak in the curvature plot (see figure 4-8). The value of Γ can be computed as reported in figure 4-10, as the peak in curvature travels down the tail.

In the case of the single-tail swimmer, the waveform remains periodical and the value of the total curvature remains roughly constant as the wave travels along the tail (see figure 4-10). Note that as a given wave forms and later ends at the extremities of the tail, the total curvature Γ first increases around $s = 0$ to a given value and later decreases close to $s = 2L$ and we therefore only rely on intermediate values of s for which Γ represents a fully developed traveling wave. As the eccentricity of the head is decreased, the total curvature Γ first reaches a maximum value as it forms at the base of the head but then decreases in amplitude as it travels towards the other end of the tail. Figure 4-10 clearly pictures this trend, which becomes more severe as the eccentricity decreases.

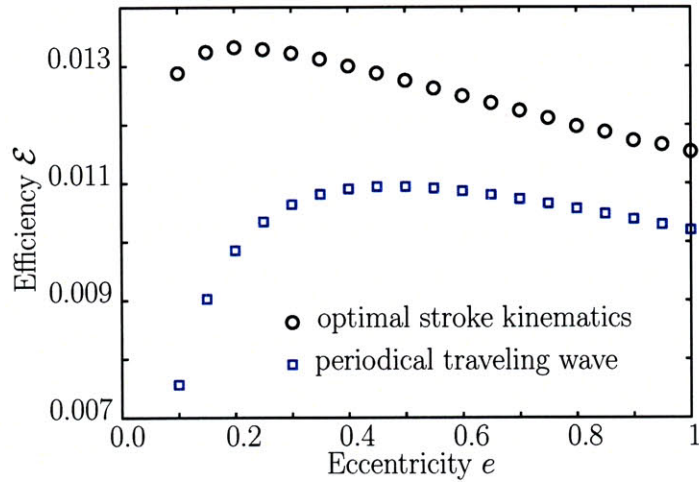


Figure 4-11: (circles): Efficiency of optimal unflagellated swimmers as a function of the eccentricity of the head. (squares): Efficiency for a unflagellated swimmer with eccentricity e whose stroke is the optimal traveling wave of the single-tail swimmer.

While for a biological swimmer, a decrease in curvature as the wave propagates could be due to many internal mechanisms such as diffusion of the active region of the flagellum, it is interesting to note that it also leads to optimal strokes. In fact, this alteration of the waveform leads to a significant increase in efficiency. Figure 4-11 reports the value of the efficiency corresponding to the optimal stroke. This plot also indicates for each eccentricity, the efficiency of a swimmer which propels itself using the simple periodic traveling wave that has been optimized for the single-tail swimmer. Hence, it should be noted that the gain in efficiency given by the optimal stroke compared to a suboptimal traveling wave becomes more and more significant as the eccentricity decreases and the optimal waveform becomes less and less periodic. As the eccentricity is decreased, the efficiency of the optimal swimmer increases and reaches an absolute maximum for $e \approx 0.20$. Hence in order to move a given volume of payload, the optimal eccentricity should be much lower than those typically observed in microorganisms.

It may come as a surprise that the optimal eccentricity is so low. In fact, one could have argued that the optimal eccentricity should correspond to a minimal drag of the head in the axial direction. We thus compare the drag coefficients on a head of

constant volume for different values of the eccentricity e . These drag coefficients can be easily estimated by using the expressions given in equation(4.16) and imposing the constant volume constraint. This calculation is straightforward and the total normalized drag coefficient of the head in the axial direction $c_0^{\parallel}L_0$ is found to reach an absolute minimum of value 0.95 for an eccentricity of $e = 0.52$, where the drag coefficient has been normalized by its value for a sphere of same volume. The minimal drag eccentricity is much larger than the value of $e \approx 0.20$, which we obtained for our optimal swimmer. In fact the normalized drag coefficient for our optimal swimmer is much larger as well and takes the value of 1.05.

Nevertheless, this result should not be too surprising and can be well understood by going back to the basic mechanism underlying low Reynolds locomotion, namely the drag anisotropy, which we discussed previously in section 3.3.1 in the context of the three-link swimmer. The drag coefficient in the axial direction is larger for $e = 0.20$ than for $e = 0.52$ but the ratio of the normal and tangential drag coefficients is also larger in this case. This increase in drag anisotropy, which is at the root of low Reynolds number locomotion, can be exploited in order to generate more efficient strokes. In fact, the change in the waveform as e is decreased is an illustration of how a stroke can be altered in order to take advantage of the drag anisotropy to increase the efficiency. It is therefore worth mentioning that in general increasing the drag anisotropy of the head can lead to significant increases in terms of swimming efficiency. In this regard, one could eventually investigate optimal head shapes for low Reynolds number swimming, as there seems to be a trade off between minimizing the drag coefficient c_0^{\parallel} in the axial direction and maximizing the ratio between the normal and the axial coefficient $c_0^{\perp}/c_0^{\parallel}$. For spheroidal heads, this trade off leads to an optimal eccentricity of $e = 0.2$, for which the axial drag coefficient c_0^{\parallel} is larger than its minimal value reached for $e = 0.52$ but smaller than the value for an eccentricity going to zero as c_0^{\parallel} diverges to infinity in that case. Similarly, the ratio of drag coefficients for the optimal eccentricity $e = 0.2$ is higher than for $e = 0.52$ but smaller than its value of $c_0^{\perp}/c_0^{\parallel} \approx 2$ for an eccentricity e going to zero

While the biological significance of the optimal eccentricity of $e = 0.20$ seems

doubtful as most sperm head do not exhibit such large elongation, it is still interesting to point out that previous studies on sperm competition have found a positive correlation between the elongation of the head and the swimming speed of the organism [108]. In this experimental study, spermatozoa with elongated head were found to swim faster, which could be due to both a decrease in the tangential drag coefficient as well as the increase in drag anisotropy.

4.5 Optimal morphology for uniflagellates

While a systematic analysis of optimal stroke kinematics is difficult to achieve, because it is difficult to numerically parameterize and quantify a stroke, an investigation of optimal geometries for swimmers can be done much more easily, as the geometry of the swimmer can be naturally represented by a few parameters. Furthermore, while the availability of precise experimentally recorded data on microorganism stroke kinematics is only limited, quantitative measurements on sperm morphology have been thoroughly performed and the results are well documented. For these reasons, we now turn our attention to the geometry of the swimmer and investigate optimal morphologies and more specifically whether there exists an optimal ratio of tail to head length. To address this question, we make the simplifying assumption that the head is a sphere and no longer consider the effect of the head eccentricity.

4.5.1 Optimal ratio of tail length to head length

Intuitively, one would expect an optimal tail length to exist for a given head size. This is because, when the length of the tail goes to zero the swimmer becomes a rigid sphere and can no longer propel itself. In this case, the swimming efficiency goes to zero. Similarly when the length of the tail goes to infinity, most of the swimmer becomes *deadload* and a growing fraction of the work done against viscosity goes into moving the tail itself and not the head, which is the equivalent swimmer corresponding to the payload. Hence we expect the efficiency to decay to zero when the length of the tail goes to infinity. Therefore, the efficiency should reach a maximum value for a finite

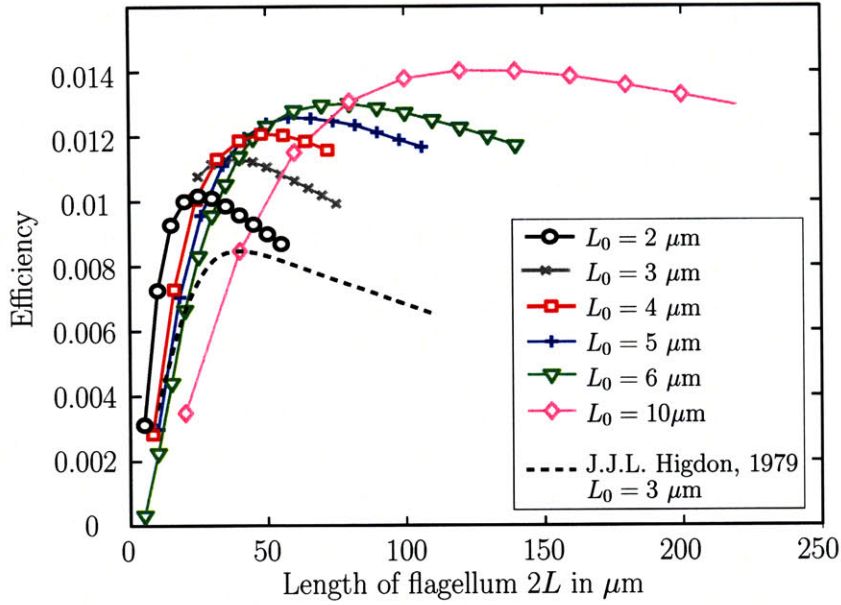


Figure 4-12: Efficiency as a function of the length $2L$ of the flagellum for various sizes of the head L_0 . The black dashed line corresponds to results from J.J.L. Higdon [74] after the data has been renormalized.

tail length somewhere between these two limit cases.

In order to investigate this question further, we first fix the radius of the head L_0 . We then impose the length of the tail L before performing a complete optimization of the stroke kinematics, following the same procedure used so far. The value of the efficiency corresponding to this specific geometry is stored. We then perform this optimization for a large number of tail lengths L . Figure 4-12 represents the efficiency of the optimal stroke kinematics as a function of the tail length L . This analysis is repeated for different values of the head size: $L_0 = 2, 3, 4, 5, 6$ and $10 \mu\text{m}$. For all these head sizes, the efficiency plots are represented in the same figure 4-12. For each head size, a maximum efficiency is reached for a specific value of the tail length, thus demonstrating that optimal tail lengths exist. The results presented here are consistent with those of a previous study by J.J.L. Higdon [74], who investigated sinusoidal planar waves only. For a fixed head size, the length of the tail was increased and the swimming efficiency of the sinusoidal wave reported. The results from this investigation are renormalized to match the dimensions of our own study and reproduced in

figure 4-12. The same trend can be observed in this earlier study (see figure 4-12). Also, a comparison with our results further reveals the relevance of fully optimizing the kinematics. Higdon's study presents results for a swimmer whose head is a sphere of diameter $2L_0 = 3 \mu\text{m}$ (after renormalization). The optimal length of the tail is found to be $36 \mu\text{m}$ and is the same as the one we found for a swimmer of the same head size. However, the maximum efficiency of the sinusoidal wave, which is reported in [74] is of 0.00846, while we found a maximum efficiency of 0.01129, representing an increase of 33 % in efficiency.

For each head radius L_0 , the tail length can be made nondimensional by rescaling it with the head size and each efficiency curve, corresponding to a given head radius, can be renormalized by the maximal efficiency reached at the optimal length. After rescaling, all efficiency curves are found to collapse and the value of the relative tail length, for which the maximum efficiency is attained, is found to be approximately $L/L_0 \approx 12$ (see figure 4-14). Hence, regardless of the size of the head L_0 the optimal length of the tail for any unflagellated swimmer is equal to $12L_0$. This constitute a rather simple criterion for optimal morphology, which can be tested against biological data.

Even though a clear optima is found, it should be noted that the peak in efficiency is very broad (see figure 4-14). In fact, the efficiency is within 90 % of the maximum value for a swimmer, whose tail length ranges between $8L_0$ and $24L_0$ and is still within 80 % for a tail lengths between $6L_0$ and $33L_0$.

4.5.2 Comparison with reported data on sperm morphology

Finally we compare this simple morphological criterion for optimal swimming with published biological data on sperm morphometry measured experimentally. Such comparisons always require caution as biological organisms are often subject to numerous environmental constraints which can affect the organism's behavior and are not taken into account in this model. However, several studies on sperm morphometry have in fact reported a positive correlation between the size of the head and the length of the tail [43, 57]. Since the function of sperm cells is indeed to transport

material from one point to the other, it is interesting to investigate how this positive correlation compares to what we have found to be an optimum from a purely mechanical point of view. Our interest is therefore not so much into whether sperm cells of a particular species satisfy a morphological criterion, rather whether there is an average trend in the morphology of microswimmers which corresponds to the criterion found in the tail to head length ratio for optimally efficient swimmers. Recall from our earlier discussion about the efficiency section 2.3.4, that the swimmers are optimized for their swimming efficiency and hence for their swimming velocity.

To this end, we focus our attention on all species in the entire class of mammals, and investigate whether such a trend exists in mammals. Data on sperm morphometry is collected from two major sources [3, 43]. For any given species, data is only taken into account if both the value of the head length and the value of the tail length is known. In cases for which the lengths of the head, the midpiece and the principal piece are known, the length of the tail is taken to be equal to the sum of the length of the midpiece and principal pieces as discussed in section 4.4. Whenever data is found in multiple sources, we report the average value. In all such cases, the values from the different sources were found to be in good agreement. Data was collected for a total of 302 species representing 5.6 % of the known 5416 mammalian species [165]. Thirteen orders are represented in the dataset, which covers 45 % of all 29 mammalian orders. All of the largest mammalian orders are present in the dataset, as these 13 orders include 88 % of all mammalian species. A summary of the sample of species, for which data on the sperm morphometry is known, is given in table 4.2.

All the different mammalian species are represented as points in the two dimensional $(2L, 2L_0)$ -space (see figure 4-13). Each order is represented with a different symbol. We also report in figure 4-13 the line corresponding to the optimal tail to head length ratio as well as the bounds in the $(2L, 2L_0)$ -space for which the swimming efficiency for a given L_0 is within 90 % and 80 % of the optimal value. It can be readily seen that most of the species have tail to head length ratio within 80 % of the optimal value. It bears emphasis, that the agreement between the optimal morphology and the morphology of spermatozoa observed experimentally are in good

	species in dataset / total species	data coverage
Class Mammalia	302/ 5416	5.6 %
Order Artiodactyla	66/240	27.5 %
Order Carnivora	22/286	7.7 %
Order Cetacea	1/84	1.2 %
Order Cingulata	1/21	4.8 %
Order Chiroptera	29/1116	2.6 %
Order Dasyuromorphia	2/71	2.8 %
Order Diprotodontia	15/143	10.5 %
Order Lagomorpha	1/92	1.1 %
Order Peramelemorphia	3/21	14.3 %
Order Perissodactyla	3/17	17.6 %
Order Primates	47/376	12.5 %
Order Proboscidea	1/3	33.3 %
Order Rodentia	111/2277	4.9 %

Table 4.2: Extend of data set coverage for mammals.

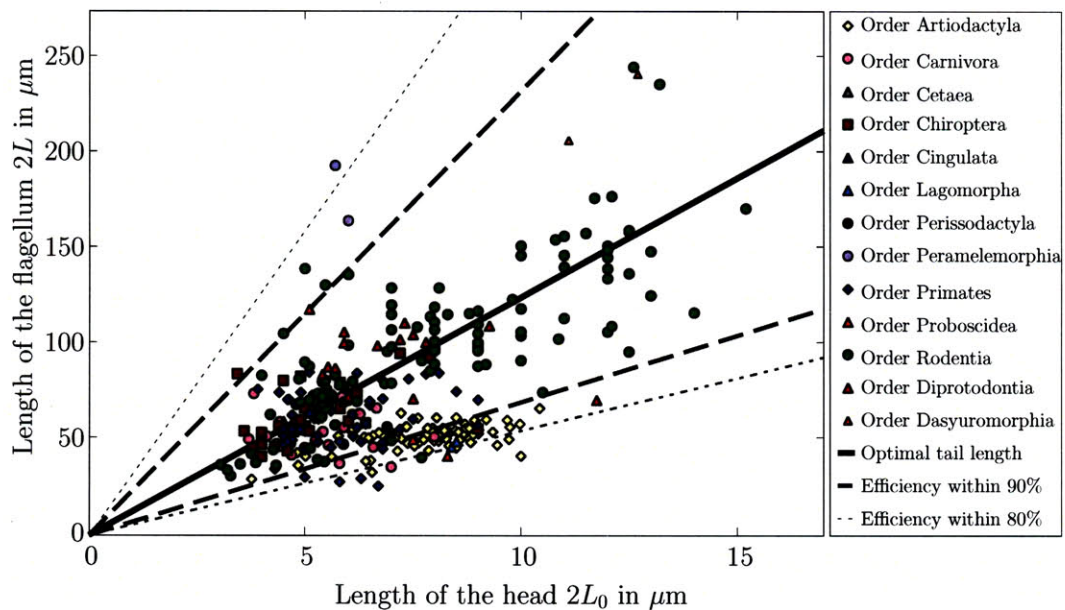


Figure 4-13: Optimal length of the flagellum $2L$ as a function of the size of the head L_0 (black line). Symbols represents data measured experimentally on 302 species of mammalian sperm.

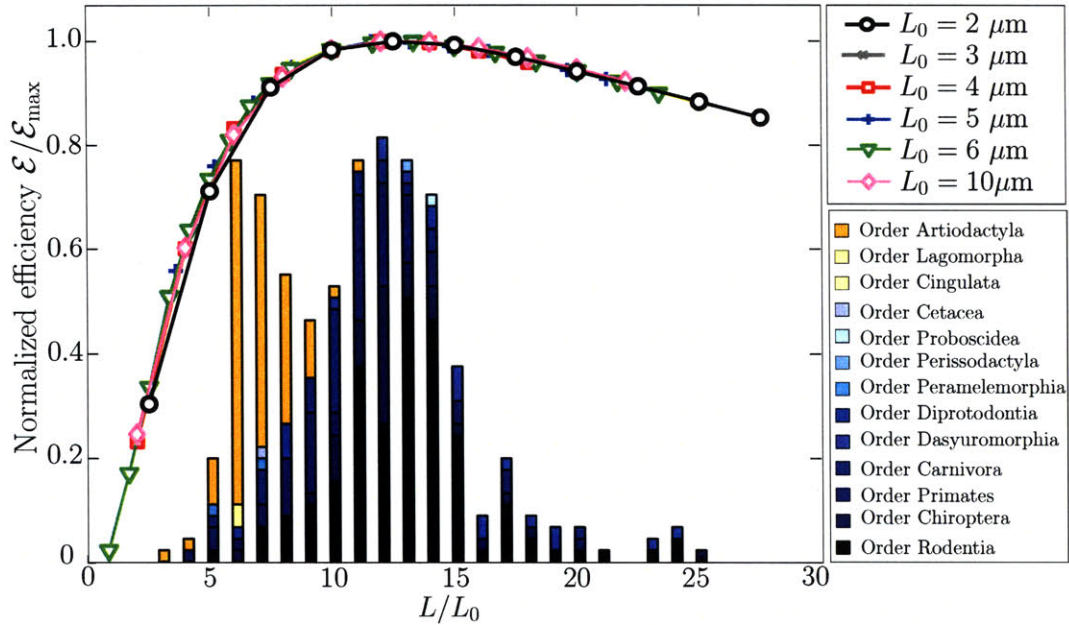


Figure 4-14: Efficiency normalized with the maximum efficiency as a function of the tail to head size ratio L/L_0 . Histogram represents the relative number of species found to have a given tail to head length ratio L/L_0 in the data set of 302 species.

agreement despite obvious simplifications in our model. Recall that we made the simplifying assumption that the head of the swimmer is spherical, whereas in reality the elongation of the head varies. Also we modeled the tails of all swimmers as simple slenderbodies of radius $r = 0.150 \mu\text{m}$, while in reality they are made of a thicker mid-piece and a principal piece. Furthermore, while all sperm tails have the structure of the eukaryotic flagellum, which usually has a radius around $r = 0.150 \mu\text{m}$, the radius of sperm tails for some species have been reported to deviate substantially from this average value. The sperm cell flagellum of a small mammal called bandicoot has a radius of up to $0.800 \mu\text{m}$ [36], which is significantly higher than the usual. Interestingly, bandicoots correspond to two species within the order Peramelemorphia, which are observed to deviate from our optimal criterion. It is of course unclear whether or not this increased radius is related to the fact that the tail is much longer than otherwise suggested by the optimal morphology criterion. It is however a good reminder that variation in many morphological parameters is not taken into account in our model.

We can further represent the distribution of the 302 species, for which data was

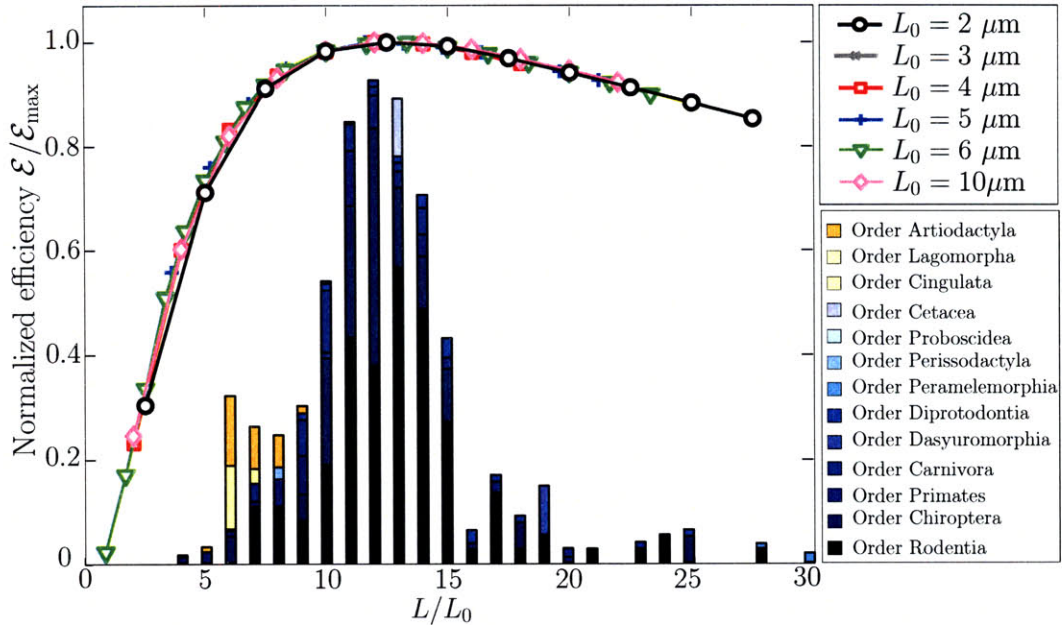


Figure 4-15: Efficiency normalized with the maximum efficiency as a function of the tail to head length ratio L/L_0 . Histogram represents the relative number of species found to have a given flagellum length to head size ratio L/L_0 . In this case the data has been rescaled depending on the number of recorded mammalian species in each order to correct for oversampling of a given order.

collected, as a function of their tail to head ratio. Figure 4-14 represents the efficiency curves which we previously found as well as a histogram representing the tail to head ratio of the 302 species. Figure 4-14 again shows that most of the 302 species have tail to head length ratios which have an efficiency within 80 % of the optimal value. It can be further noted that for most of the orders, the distribution is centered around the optimal value of $L/L_0 \approx 12$. This is true for many orders, for which we have a large amount of data available: order Rodentia (rodents), order Chiroptera (bats), order Primates, order Carnivora. However it can be seen that this is not the case for all orders. For the order Artiodactyla (bovines are in this order for example), the distribution of tail to head lengths of the sperm cells is centered about $L/L_0 = 6 - 7$. While such swimmers can still reach efficiencies within 80 % of the maximal efficiency, their morphology is significantly different from the optimal one.

In order to get an idea of what the distribution of tail to head length ratio would

be if all mammalian species were represented, one can extrapolate the distributions found for each order separately, by renormalizing them with the inverse of the data coverage percentage from table 4.2. This is equivalent to giving each order a relative weight corresponding to the number of species in the order. It is in fact relevant to do so, as we are more interested in a general trend rather than the specific morphology of the spermatozoa for a given species. In this regard, we can anticipate that the order Artiodactyla is oversampled in our dataset, as almost 27.5 % of the species are represented, while only 5.9 % of all rodents are represented.

This global distribution is represented in figure 4-15 and gives a general picture of the distribution of sperm morphologies across all mammalian species. In this case, the distribution coincides even more strikingly with the optima derived in our analysis. This agreement validates our analysis and suggests that the swimming efficiency as defined by equation (4.44) may be a relevant parameter to consider, when studying swimming microorganisms. Our results also suggest that in general, the morphology of mammalian sperm cells allows them to be efficient swimmers.

Chapter 5

Optimizing biflagellates

5.1 Introduction

In the previous chapter, we examined several aspects of the swimming properties of unflagellates, namely details of the stroke kinematics and the morphology of the swimmer. We found that, in general, traveling waves are optimal for the locomotion of unflagellates and also that a morphological optimum exists for the tail to head length ratio, which is observed to be relevant to mammalian spermatozoa. These observations however are only related to unflagellates and do not apply to the many organisms which have several flagella and have been observed to use a variety of stroke patterns. In fact, the drawing of J. Lighthill reproduced in figure 2-1 is a beautiful illustration and a good reminder of the diversity, which prevails at the micron scale.

Unicellular organisms range in size over several orders of magnitudes, from less than a micrometer to several hundreds of micrometers. It is interesting to notice that larger cells tend to have more flagella: sperm cells are a few microns long and have one flagellum, green algae *chlamydomonas* are a few tens of microns long and have two flagella, ciliates such as paramecia are a few hundreds of microns long and have a very large number of flagella, which are then called cilia. When multiple flagella are present at the surface of the cell, interesting questions arise related to beating synchronization and the role of hydrodynamics in coordination and collective behavior [66].

In this chapter, we will focus our attention on biflagellated swimmers using a direct extension of the model developed in our previous study. A prototypical biflagellated organism is the green algae *chlamydomonas*, which has a cell body of about $10\ \mu\text{m}$ in length and two $10\ \mu\text{m}$ long flagella. Locomotion and stroke patterns of *chlamydomonas* have been investigated experimentally by U. Ruffer and W. Nultsch [131–135]. The complex beating patterns of *chlamydomonas* have been found to vary significantly in response to various stimuli. However at the level at which we are interested in modeling locomotion of biflagellates, *chlamydomonas* can be considered to primarily exhibit two different strokes. The most common stroke is often called the breaststroke and is reproduced from [131] in figure 5-5(a-b). It has the same effective-recovery structure as the stroke of cilia, and is quite different from an undulatory traveling wave. Another stroke, which is observed in response to a shock of light [134] or an electric stimulation [168] is an undulatory stroke, which resembles the beat patterns observed in uniflagellates as discussed in the previous chapter. An illustration of this stroke is reproduced from [134] in figure 5-3(a-b).

We propose to examine optimal stroke patterns for biflagellated organisms and to investigate whether these two different beating modes can be found and explained by considering the hydrodynamics only.

5.2 Modeling of the dynamics of biflagellates

5.2.1 Geometry of the swimmer

Our representation of biflagellated swimmers is directly derived from the model for uniflagellates developed in chapter 4. The cell body is considered to be a rigid sphere of diameter $2L_0 = 10\ \mu\text{m}$, which corresponds to the size of green algae *chlamydomonas*. The position of the head cell is given at each time by the position vector \mathbf{R}_0 and the angle θ_0 , which defines the orientation of the cell body. Here, $\mathbf{t}_0 = (\cos \theta_0, \sin \theta_0)$ is the unit vector in the main axis of the head and $\mathbf{n}_0 = \hat{\mathbf{z}} \times \mathbf{t}_0$ is the unit normal vector (see figure 5-1).

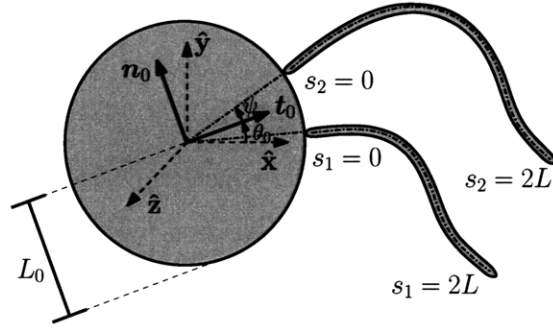


Figure 5-1: Schematic of a biflagellated swimmer and related notation.

The swimmer has two deformable flagella of equal length $2L$ and slenderness $\kappa = r/2L$. The attachment of the two tails is defined by the angle of attachment ψ , which is arbitrarily taken to be equal to $\pi/12$. Each tail is represented by a different subscript $i = 1, 2$. Let s_i be the arc length measured along the centerline of the i^{th} tail, and γ_i , \mathbf{t}_i , \mathbf{n}_i , \mathbf{R}_i and θ_i be the curvature, tangential unit vector, normal unit vector, position vector and angle between $\hat{\mathbf{x}}$ and \mathbf{t}_i along the centerline of the i^{th} tail. Each tail is attached to the head at $s_i = 0$ and such that

$$\begin{aligned}\mathbf{R}_i(s_i = 0) &= \mathbf{R}_0 + L_0(\cos \psi \mathbf{t}_0 \pm \sin \psi \mathbf{n}_0), \\ \mathbf{t}_i(s_i = 0) &= \cos \psi \mathbf{t}_0 \pm \sin \psi \mathbf{n}_0.\end{aligned}$$

The position vector and deformation velocity along the tails can be obtained by integration of the Serret–Frenet equations along the centerline of each tail, as described in section 4.2.1.

5.2.2 Dynamics of the swimmer

We use the same hydrodynamic modeling developed for unflagellated swimmers, which is described in section 4.2.2. The system of singularity distributions modeling the flow has the same structure as for the unflagellated case: a distribution of stokeslets and associated potential doublets (of strength $r^2/2$ times the strength of the stokeslet distribution) for each of the two tails, and a point rotlet, stokeslet and associated potential doublet for the spherical head.

The only difference occurs when considering the hydrodynamical interaction term, for which the extra tail has to be taken into account. Recall that interaction between the different parts of the swimmer are due to the ambient flow generated around one part by the motion of the other part, which can be taken into account by use of Faxén’s laws. Hence, we model the interaction by computing on the one hand the ambient flow around the head as the superposition of the flow induced by both tails and on the other hand the ambient flow around each tail as the superposition of the flow induced by the head and the other tail.

Using this model for the hydrodynamics of the swimmer, we impose the equilibrium equations on the entire system as is done for uniflagellates in equations (4.29,4.30). We use the same spatial discretization and the motion of the swimmer is numerically computed and integrated in time using the same method as described in section 4.2.4.

5.2.3 Optimization procedure

The optimization procedure developed for uniflagellates is again directly applied to the case of biflagellates. In this study, we explore two different purposes for locomotion. One of them is swimming, which we have already discussed; the other is feeding. Later in this chapter, we will discuss the hydrodynamic implications of these two locomotion modes and derive two formulations for efficiencies characterizing these two modes.

A few additional remarks specific to the optimization procedure applied to biflagellated swimmers are made in the following.

Geometric constraints on stroke patterns

In this analysis we add an additional geometric constraint on acceptable stroke patterns for biflagellated swimmers. This constraint is imposed in order to avoid intersection between the spherical head and the two flagella. In our previous study of uniflagellates, this constraint was not required, as the head of the swimmer was usually small compared to the flagellum and the optimization procedure never converged

towards strokes in which the tail approached the head of the swimmer. For *chlamydomonas* however, the spherical head of the swimmer has a diameter of $10\ \mu\text{m}$ and the flagella are also $10\ \mu\text{m}$, and hence the tail is relatively short. For such geometries, our procedure sometimes converges towards strokes where one flagellum penetrates the cell head. Recall that only the far field hydrodynamic interaction is taken into account, which does not properly model the hydrodynamics when the flagellum is near the surface of the cell body. Furthermore, our prescription of the flagellar deformation by simply imposing the curvature along the tail does not prevent interpenetration of flagellum and head.

We therefore impose the following geometrical constraint at all times on the deformation of the flagellum:

$$\|\mathbf{R}_i(s_i) - \mathbf{R}_0\| \geq L_0 \quad \text{for all } s_i \in [0, 2L], \text{ and } i = 1, 2.$$

Symmetrical stroke patterns

By adding one flagellum, one can readily anticipate an increase in the complexity of the system's behavior. The stroke kinematics of two separate flagella are now being optimized, which increases the number of deformation parameters by a factor of two. In order to reduce the computational cost required by the optimization procedure, we will in some cases implicitly assume a symmetry in the stroke kinematics, as we did for the unflagellated swimmer in section 4.2.5. Such symmetrical strokes are defined such that at all times the axis \mathbf{t}_0 , which goes through the center of the head is an axis of symmetry of the swimmer. This can also be expressed as follow:

$$\gamma_1(s_1 = s) = -\gamma_2(s_2 = s) \quad \text{for all } s \in [0, 2L].$$

In this case, the problem reduces to finding the general stroke kinematics for one flagellum, while the other can be simply deduced as the mirror image. For biflagellates, such strokes will always be referred to as symmetrical strokes.

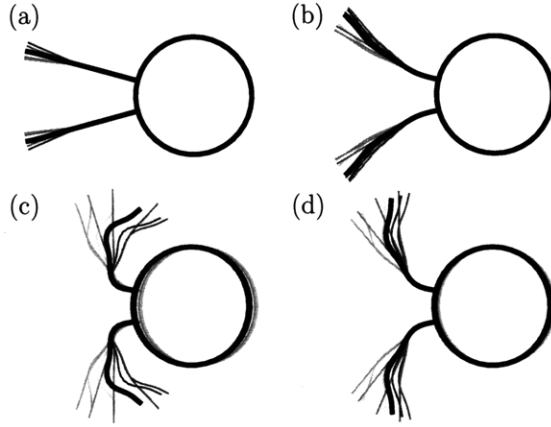


Figure 5-2: Representation of typical initial strokes for the optimization of biflagellated swimmers.

5.3 Optimal biflagellated swimmers

5.3.1 Swimming efficiency for biflagellates

We first study biflagellates in the context of their swimming efficiency, as a direct extension of our previous work on unflagellated swimmers. The expression for the swimming efficiency remains the same and can be simply written as

$$\mathcal{E} = \frac{c_0^{\parallel} U_0 \ell_0}{W_{\min}}. \quad (5.1)$$

In this case, the axial drag coefficient is equal to $c_0^{\parallel} = 6\pi\mu L_0$ since the head is considered to be spherical. The optimization procedure is started from different initial guesses, a sample of which is represented in figure 5-2. Note that these initial guesses vary greatly in amplitude; the strokes represented in figure 5-2(a-b) consist of small amplitude oscillations around the straight configuration for the flagella, while those represented in figure 5-2(c-d) exhibit large amplitude deformations.

Unlike our previous study of unflagellates, the optimization procedure does not always converge to the same solution and the addition of a second flagellum is found to substantially increase the complexity of the optimization problem. For all initial strokes which we originally conjectured, the procedure converged to three different

strokes found to be locally optimal for swimming. These strokes are represented in figure 5-4(a-c).

5.3.2 Optimal strokes

The first locally optimal stroke is represented in figure 5-4(a). It is found for symmetrical initial guesses of small amplitude (see figure 5-2(a)), when the stroke is constrained to remain symmetrical as described in section 5.2.3. Both the time variation of the curvature along the tail and the snapshots of the strokes at different times (figure 5-4(a)) show that this stroke is essentially made of two traveling waves which symmetrically propagate from the base of the head towards the extremity of the tail. The efficiency is found to be equal to $\mathcal{E} = 0.00184$.

The second optimal stroke is reproduced in figure 5-4(b). It is very similar to the previous one and is found for asymmetrical initial guesses of small amplitude (see figure 5-2(b)), when the symmetry in the stroke pattern is no longer enforced. This stroke also consists of two traveling waves that propagate along the tail. In this case, the swimming efficiency takes a slightly lower but comparable value of $\mathcal{E} = 0.00165$. While the first symmetrical traveling wave has not been observed experimentally, the asymmetrical optimal traveling wave closely resembles the undulatory stroke, which is undergone by *chlamydomonas* after a shock. The kinematics of the computed undulatory optimal stroke can be compared to the experimentally recorded stroke, see figure 5-3(b-c) and is found to be qualitatively in good agreement.

The last optimal stroke is found for an initial large amplitude guess with implicitly enforced symmetry. This stroke is represented in figure 5-4(c). Its swimming efficiency is higher than the two previous strokes and takes a value of $\mathcal{E} = 0.00366$. This stroke however has not been observed experimentally and its structure appears to be more complex than the previous two strokes. As can be seen on both the curvature plots and the representations of the swimmer (figure 5-4(c)), two separate sections of high curvatures, which are opposite in sign, simultaneously develop along the tail and propagate. One can conjecture that this stroke may not be observed as no simple self-organized mechanism is able to sustain such complex periodic deformation.

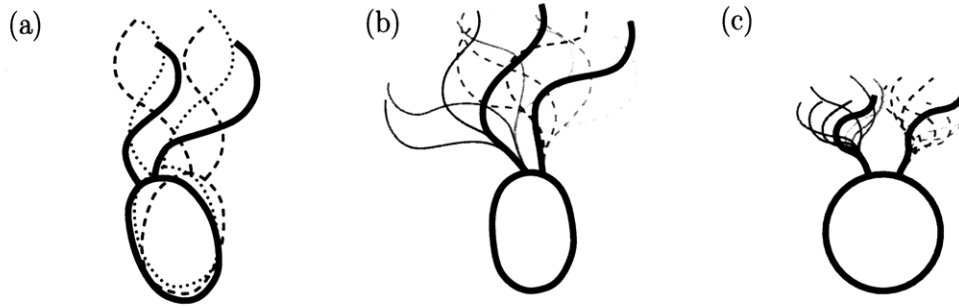


Figure 5-3: Representation of stroke patterns of *chlamydomonas* using high-speed cinematography, reproduced from Ruffer and Nultsch [131, 134]. (a) Free swimming *chlamydomonas* undergoing an undulatory beat [134]. (b) Representation of an undulatory stroke, in the frame of reference linked to the cell [134]. (c) Computed undulatory stroke optimized for swimming efficiency.

It is interesting to note at this point, that none of the presented strokes produces very efficient swimming. The values found for the swimming efficiency should be compared with what has been previously found for uniflagellates. The optimal uniflagellated swimmer with a spherical head of diameter $2L_0 = 10 \mu\text{m}$ and optimal tail length is found to reach a much higher efficiency of 0.01402 (see figure 4-12). In fact, the value of the efficiency for a uniflagellated swimmer, whose tail is $20 \mu\text{m}$ long is 0.00344 which is almost the same as the efficiency of the large amplitude optimal stroke and higher than the efficiency of either the symmetrical or the asymmetrical optimal traveling waves.

Hence from our analysis, *chlamydomonas* does not appear to be a very efficient swimmer, at least not with respect to the swimming efficiency defined in this study. We therefore turn our attention to another aspect of transport at low Reynolds number and investigate optimal strokes related to feeding and enhancement of nutrient uptake. This survey about optimal strokes for swimming is however incomplete. Following the discussion on optimal strokes for feeding, we will later find a final locally optimal stroke for swimming, which will be discussed.

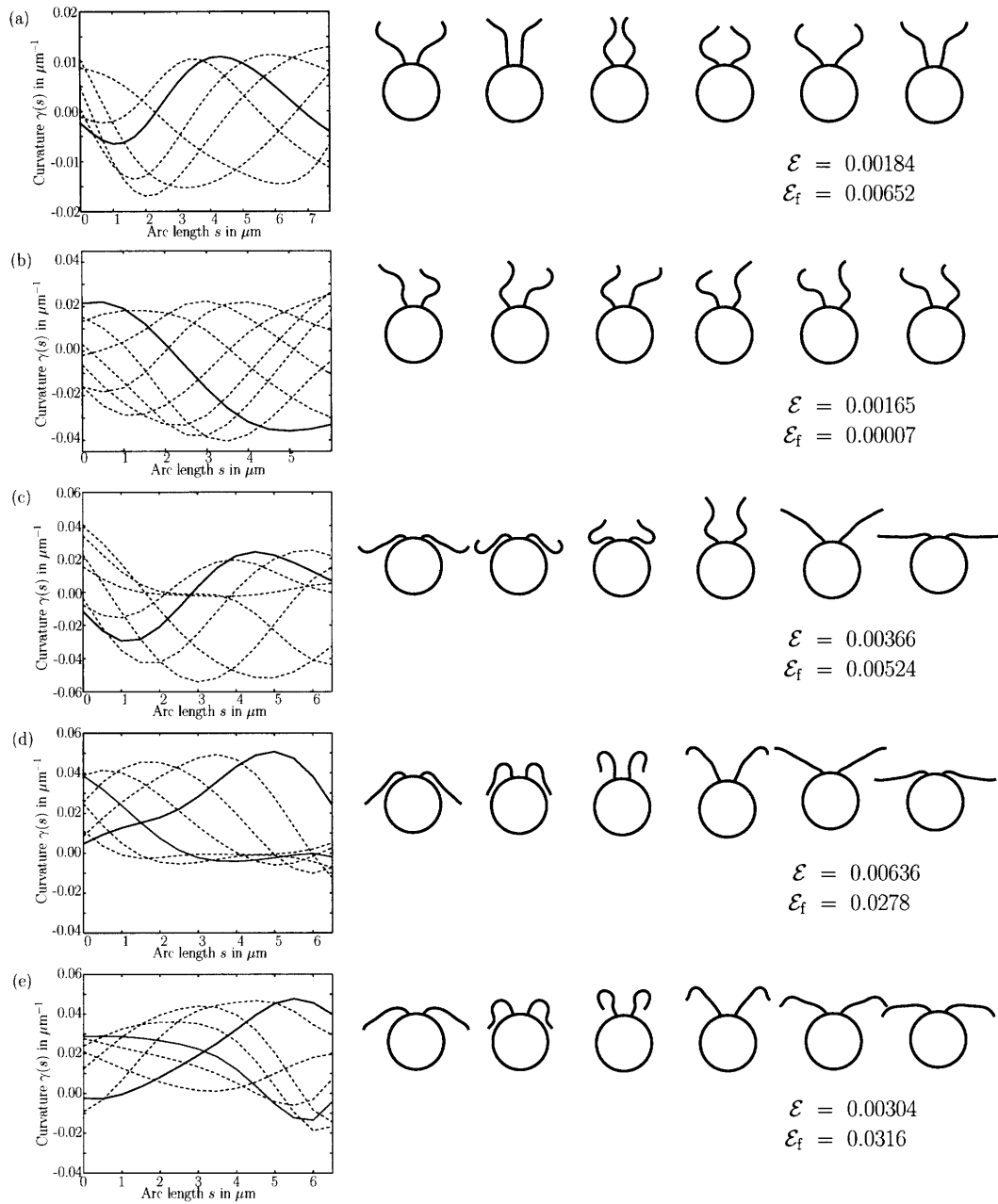


Figure 5-4: Time snapshots of the curvature γ as a function of the arc-length for all optimal strokes found. Each stroke is further represented by a sequence of shapes. (a) Strokes optimized for swimming efficiency with small amplitude symmetric initial guess. (b) Strokes optimized for swimming with small amplitude antisymmetric initial guesses. (c) Strokes optimized for swimming with large amplitude symmetric initial guesses. (d) Strokes optimized for swimming using optimal feeding stroke as the initial guess. (e) Strokes optimized for feeding.

5.4 Optimal biflagellated feeders

5.4.1 Scaling analysis for the transport problem

Previous studies have investigated the generation of feeding currents [32, 73, 105] by propagating periodic waves along flagella. Similar to what we have done in the case of swimming, we now consider in questions related to nutrient uptake and seek to determine the existence of optimal stroke kinematics for feeding purposes. Before going any further in the analysis and modeling of this problem, it is worth getting some insight into the characteristic transport timescales from a scaling analysis, in order to justify the relevance of feeding currents to such organisms.

The generation of advective feeding currents for the enhancement of nutrient uptake is only meaningful if the transport problem is not completely dominated by diffusion. The Péclet number represents the ratio of the characteristic diffusive timescale over the characteristic advective timescale. For this problem, the Péclet number can be written as

$$\text{Pe} = \frac{U_{\text{ref}} L_{\text{ref}}}{D},$$

where U_{ref} is a characteristic velocity for the fluid flow, L_{ref} is a characteristic length scale and D is the diffusivity of the nutrients under consideration. For small Péclet numbers, the diffusive timescale is much smaller than the advective timescale and the transport problem is entirely dominated by diffusion. In this case, nutrient uptake cannot be increased by advection. For a typical swimming biflagellate, the length scale is on the order of $10 \mu\text{m}$, the beat frequency for *chlamydomonas* is on the order of $50 - 100 \text{ s}^{-1}$ and an upper-bound for nutrient diffusivity is given by the diffusivity of CO_2 which is about $10^{-9} \text{ m}^2 \text{ s}^{-1}$. This scaling analysis gives an estimate for the Péclet number of $\text{Pe} \sim 5 - 10$. For larger molecules, we expect the Péclet number to be even higher than for CO_2 . Hence transport is not completely dominated by diffusion and it is relevant to investigate the advective transport of nutrients via the generation of feeding currents.

5.4.2 Feeding efficiency for biflagellates

We therefore seek to define a feeding efficiency, which characterizes how effectively the stroke enhances nutrient uptake. In agreement with our prior definition of the swimming efficiency, the feeding efficiency is defined as the fraction of the total energy expense effectively used to create a flux of nutrients. We thus need to determine the effective flux towards the surface of the cell body, which in general requires the resolution of the full advection-diffusion equation for the concentration of nutrients in the entire flow field. This however would require detailed numerical modeling and significant computations, which would make the optimization procedure significantly more expensive. Because the Péclet number is finite, we instead decouple the advection from the diffusion problem and focus our attention only on the advection of nutrients in order to quantify how well a given stroke is able to advect flow towards the cell body.

Because the problem is unsteady, the estimation of nutrient uptake cannot rely on average flow fields over one stroke period and associated fluxes. Instead, the particle pathlines have to be fully integrated in time. We simplify this problem by considering a finite number of spherical fluid blobs of radius $a = 1 \mu\text{m}^*$. The center of each sphere lies in the (\hat{x}, \hat{y}) -plane at a distance $d = 5 \mu\text{m}^\dagger$ from the surface of the cell body. The blobs are densely packed and equally spaced on a circle of radius $L_0 + d$ centered at the same point as the cell body (see figure 5-7). We follow the motion of each virtual blob by computing the particle pathlines of the center of each blob over one stroke period. We only consider blobs that get closer to the surface of the cell after one stroke to contribute to the effective nutrient flux. The work required to move each blob is simply equal to $5\pi\mu a\ell/\tau$, where ℓ represents the net distance the blob has traveled towards the cell surface over one period τ of the stroke. The drag coefficient for a sphere of fluid of radius a moving in an unbounded fluid of the same viscosity is given by $5\pi\mu a$, see [70]. The feeding efficiency \mathcal{E}_f is defined as the sum of the work

*The radius of the blob a has a value of $1 \mu\text{m}$, which corresponds to the distance from the slender flagellum over which the fluid is still significantly moved by the motion of the flagellum.

†The distance d has been chosen to be about twice the diffusive length for CO_2 over one stroke period τ .

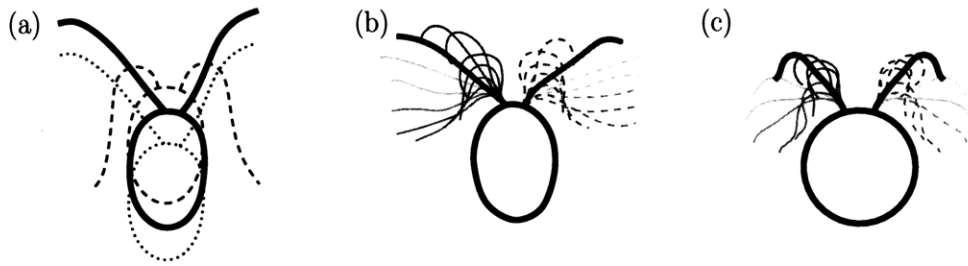


Figure 5-5: Representation of stroke patterns of *chlamydomonas* using high-speed cinematography, reproduced from Ruffer and Nultsch [131, 134]. (a) Free swimming *chlamydomonas* undergoing a breaststroke beat [131]. (b) Representation of a breaststroke, in the frame of reference linked to the cell [131]. (c) Computed breast stroke optimized for the feeding efficiency.

required to move all the equivalent blobs closer to the cell body over the total work exerted by the swimmer against viscosity.

5.4.3 Optimal breaststroke for feeding

Using this definition for the feeding efficiency as the objective function for our optimization procedure, we find one optimal stroke regardless of the initial guess (see figure 5-2). This stroke is represented in figure 5-4(e) and bears close similarities with the breaststroke, which is the most commonly observed stroke for *chlamydomonas*. For a comparison between our computed optimal stroke and experimentally recorded strokes see figure 5-5(b-c). The optimization procedure in this case converges to a breaststroke, which has the same effective-recovery structure as observed in ciliates (see stroke representation in figure 5-4(e)). It is remarkable, that both the undulatory stroke and the breaststroke, which are observed experimentally and have very different structures (traveling wave vs. effective-recovery stroke), are found to be optimal by considering hydrodynamics alone. In terms of the organization of the stroke, the breaststroke is observed to consist of a single peak of curvature traveling from the base of the head towards the end of the tail. The curvature plots in figure 5-4(e) show the propagation of a section of high curvature, with no change or alteration in sign.

The feeding efficiency for the computed breaststroke is 0.0316 and the swimming efficiency is 0.00304. For comparison the feeding efficiencies for the symmetrical

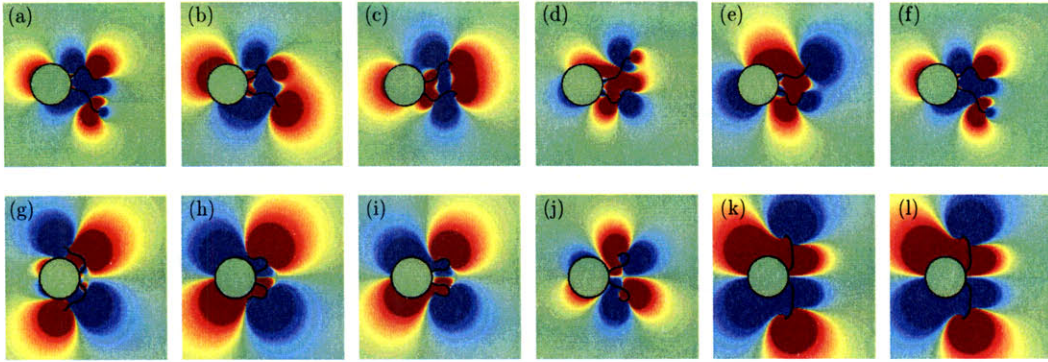


Figure 5-6: (a-f) Vorticity field around a biflagellated swimmer undergoing a breast stroke. (g-l) Vorticity field around a biflagellated swimmer undergoing the undulatory stroke.

propagating wave, asymmetrical propagating wave and the large amplitude stroke optimized for swimming have all much lower values, which are respectively of 0.00652, 0.00007 and 0.00524.

The superiority of the breaststroke in generating feeding currents compared to other strokes can be readily seen when representing the vorticity field around the head of the swimmer. Figure 5-6 represents snapshots of the vorticity field around a biflagellated swimmer undergoing the undulatory stroke (figure 5-6(a-f)) and the breaststroke (figure 5-6(g-l)). The color-scale is identical in all pictures and we can therefore observe that the breaststroke develops much larger scale vortex structures around the head of the swimmer than the undulatory stroke. This larger scale flow results in the generation of more efficient feeding currents. These currents can be further observed by following the trajectories of particles in the flow over during a stroke. Figure 5-7 represents the particle pathlines of points corresponding to the centers of the blobs considered in the calculation of the feeding efficiency. The breaststroke is observed to drag particles close to the cell surface, thus generating feeding currents (figure 5-7(a)). For the undulatory stroke no such currents are observed (see figure 5-7(b)).

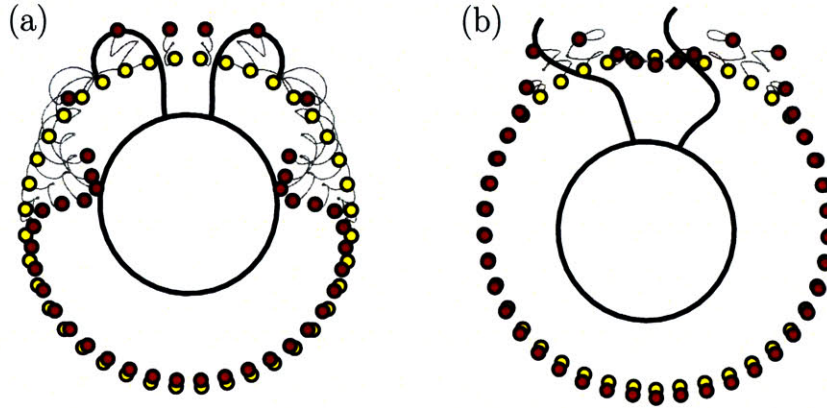


Figure 5-7: Representation of the particle pathlines of material points for two successive strokes of a biflagellate. The swimmer is represented in its geometry and location at the end of the two strokes. Yellow and red marks represent respectively the initial and final position of the particles. Gray lines represent the particle pathlines. (a) Optimal computed breaststroke for feeding efficiency (b) Optimal undulatory stroke for swimming efficiency.

5.4.4 Optimal breaststroke for swimming

Finally, we go back to the initial survey of optimal swimming strokes. While the breaststroke could not be found from any of the initial guesses depicted in figure 5-2, its swimming efficiency of 0.00304 compares well to the efficiency of the large amplitude stroke described in section 5.3.2, which is 0.00366. We therefore pursue our original search for optimal swimming strokes, by taking the breaststroke optimized for feeding as the initial guess. As mentioned at the end of section 5.3.2 we find another optimal breaststroke with a swimming efficiency of 0.00636 and of feeding efficiency 0.0278. This stroke is represented in figure 5-4(f). It has the same structure as the breaststroke optimized for feeding but in this case the two flagella extend further away from the cell body at the end of the recovery stroke and before beginning the effective stroke.

This final remark is in good agreement with experimental observations, as the breaststroke is found to prevail over the undulatory stroke, which is only observed as a shock response. Hence, the breaststroke is found to be efficient for both swimming and feeding, although the swimming efficiency is still well-below what can be achieved by

an optimal uniflagellate. Further more, we argued in section 2.3.4 that the swimming efficiency as defined in this study is in fact a measure of how fast a swimmer can propel itself. In light of this discussion, it is interesting to note that the maximum swimming velocity measured experimentally for the breaststroke and the undulatory stroke are respectively $240 \mu\text{m.s}^{-1}$ [131] and $50 \mu\text{m.s}^{-1}$ [134]. The ratio between these two values is of $240/50 \sim 4.8$, which agrees quantitatively with the ratio of efficiencies found for the optimal swimming breaststroke and the undulatory wave $0.00636/0.00165 \sim 3.8$.

Chapter 6

Marangoni convection in droplets on superhydrophobic surfaces

6.1 Introduction

We now turn to a different problem also related to motion at low Reynolds number and investigate the dynamics of droplets on heated superhydrophobic substrates. This chapter* presents experimental and analytical results, which are independent from the previous studies on low Reynolds locomotion, although also related to questions of mixing and transport.

Non-wettability, effective heat transfer coefficients and other material properties of hydrophobic surfaces are of interest in many industrial applications, such as efficient condensing design and waterproofing textiles. Since [163] noted seventy years ago that the hydrophobicity of a substrate can be enhanced through a combination of chemical modification and surface roughness, multiple studies have observed a substantial increase in static contact angles by integrating these two strategies. More recently the non-wetting properties of these substrates have been further enhanced and contact angles close to 180° have been achieved by introducing nanoscale rough-

*This work was done in collaboration with Volkmar von Armin and Gareth H. McKinley in the Department of Mechanical Engineering at the Massachusetts Institute of Technology and is part of “Heat transfer and Marangoni convection in droplets on super-hydrophobic surfaces”, D. SW. Tam, V. von Armin, G. H. McKinley and A. E. Hosoi, submitted to *J. Fluid Mech.*, 2008

ness [15, 124, 127, 171].

Numerous techniques have been developed over the past decade for fabricating robust superhydrophobic surfaces by combining chemical non-wetting treatments with controllable levels of roughness over a wide range of length scales. General discussions of the principles for preparing such surfaces are given by [125] and by [116]. [115] and co-workers used fractal patterns formed in an alkene wax to produce the first superhydrophobic surfaces with contact angles greater than 160° . Since then surfaces have been prepared using a variety of materials processing techniques including: lithographically patterned silicon posts having a wide range of aspect ratios [93, 95]; silicone arrays patterned using soft lithography [71]; layer-by-layer (LBL) assembled polymeric coatings decorated with nanoparticles [170]; and microporous polymeric silica structures [60] in addition to the vertically aligned carbon nanotube carpets [97] used in the present study. In many of these formulations the surface coating consists of polymeric or ceramic constituents that are poor thermal conductors which limits the efficacy of the surface in heat transfer applications. One of the advantages of the carbon nanotube carpets employed in the present work is the high axial thermal conductivity of the graphene sheets that form the multiwall nanotubes.

The interactions between small liquid droplets and such superhydrophobic surfaces give rise to interesting phenomena in terms of the dynamics of the droplet [25]. The dynamic deformations of a droplet impinging and bouncing on a hydrophobic substrate have been investigated [128, 129]. An other important dynamic behavior is related to the adhesion and motion of droplets at the surface of the substrate. Droplets are observed to reach large velocities as they move on top of the superhydrophobic surface, which raises the question of whether the liquid is sliding or rolling. This could potentially have interesting applications as it could lead to the design of surfaces with apparent slip of liquid.

Furthermore, hydrophobically modified surfaces have interesting heat transfer properties which have primarily been studied in the context of condensation on cooled substrates (see Table 6.1). In most applications, dropwise condensation is preferable to film condensation as the continuous condensed fluid film acts as an insulating layer,

HEAT TRANSFER VIA PHASE CHANGE ON HYDROPHOBIC SURFACES





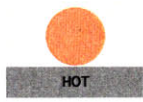

<u>Condensation</u>		<u>Boiling</u>		<u>Spray Cooling</u>	
Dropwise	Film	Nucleate	Film	Droplet	Film
					
[54]	N/A	[86] [156]		Present Study	N/A

Table 6.1: Summary of heat transfer in various geometries from superhydrophobic surfaces. A few representative studies are listed in each regime.

resulting in lower heat transfer coefficients [140]. Thus it is often advantageous to promote dropwise condensation by changing the wettability of the relevant surfaces, making them hydrophobic [54]. Recent studies have taken this one step further; by introducing wettability gradients into the substrate, condensing drops rapidly move towards more hydrophilic regions providing a passive mechanism that can increase the effective heat transfer coefficient by an order of magnitude [45].

The reverse problem of a liquid impinging on a hot surface has been less well-studied in the context of hydrophobic surfaces though numerous articles exist describing the evaporation of a single drop on a partially wetting substrate [49, 107, 137] and extensive studies have been performed on the Leidenfrost effect (see e.g. recent work by [14]). It has also been demonstrated that the effective heat transfer in such droplet systems can be significantly enhanced by adding surfactant to the fluid, decreasing the contact angle, and promoting nucleation within the impinging droplet [81, 123]. One of the few studies that incorporates the effects of hydrophobicity is [111] in which a slowly evaporating droplet on a patterned polymer surface was investigated. Unlike our system, the substrate was not heated and hence the droplet remained in a parameter regime in which Marangoni stresses were negligible.

In addition, a limited number of studies have investigated the effects of surface chemistry on boiling. [160] conducted an experimental study to quantify the effects of surface wettability on the density and distribution of nucleation sites. They confirmed

that increasing wettability both shifts the boiling curve to the right and increases the maximum heat flux, and found that the fraction of cavities that nucleate decreases as the wettability of the surface improves. [86] presents a nice review and brief history of the study of pool boiling. The author then goes on to derive a mathematical model to predict critical heat fluxes which account for the effects of hydrophobicity (through changes in the static contact angle), vapor momentum and gravity. Predictions from this model are then successfully compared with existing experimental data. More recently, [156] performed an experimental study in which the authors applied short microsecond voltage pulses to investigate the effect of surface properties on fast, transient microboiling.

However, the full problem of understanding the heat and mass transfer properties of a single stationary droplet on a heated hydrophobic surface is further complicated by the presence of a mobile free surface. Gradients in temperature along the free surface lead to gradients in surface tension which may in turn drive thermocapillary Marangoni convection [109] within the drop (as illustrated in Figure 6-1). A detailed and extensive literature on thermocapillary driven flows exists and both experimental and theoretical studies are reviewed in [139] and [48] respectively, as well as in [150] which considers thermocapillary motion in droplets and bubbles.

One of the few analyses that has carefully investigated the effects of Marangoni stresses in evaporating sessile drops is the recent study by [76]. In this work, the authors model convection in a droplet on a partially wetting surface using both a lubrication analysis and a full finite element model (FEM). They find that convection rolls are observed — with a down-welling in the center of the droplet — driven by a non-uniform temperature distribution at the surface of the droplet which arises from evaporative cooling. Surprisingly, the lubrication approximation is in good agreement with the FEM even for contact angles as high as 40° .

In this study, we investigate Marangoni convection within a single droplet on a heated superhydrophobic surface. The analysis differs from that of [76] in that our droplet is nearly spherical and hence not amenable to lubrication techniques. Ultimately, by comparing experimental data with analytic predictions, we can extract a

value for the effective heat transfer coefficient of the system. In section 6.2 we describe the experimental setup and procedure. Section 6.3 presents the derivation of the governing equations for the system which are then solved analytically in section 6.4. Finally, section 6.5 presents a quantitative comparison of analytic and experimental results.

6.2 Experimental methods

6.2.1 Background

Several dynamic aspects related to the properties of the carbon nanotube carpeted substrate described in [97] have been investigated. One such study originally focused on the motion of a water droplet released at the surface of an inclined substrate. In this study, Dr. Volkmar Von Armin and Prof. Gareth McKinley intended to determine whether the droplet was rolling or whether it was indeed sliding at the surface of the substrate. In order to do so they visualized the internal motion of the droplet by seeding the water with tracer particles and recorded their motion with high-speed imaging. This led to the observation of a strong flow from the center of the droplet towards the contact point, as tracer particles seemed to be attracted by the contact point. This observation could not be related to either a rolling or a slipping motion. Following these observations, the droplet was then immobilized on the surface of the substrate and the internal dynamics recorded. This follow up experiment is at the center of the present study and is described in more details in the next section.

6.2.2 Experimental setup

A schematic of the experimental setup is shown in Figure 6-2. Monodisperse silica particles 300nm in diameter were added to deionized water at a concentration of 1wt % in order to track convective motions (see Figure 6-3). The droplets were formed at the tip of a thin glass capillary approximately 10 μm in diameter, and were deposited on a

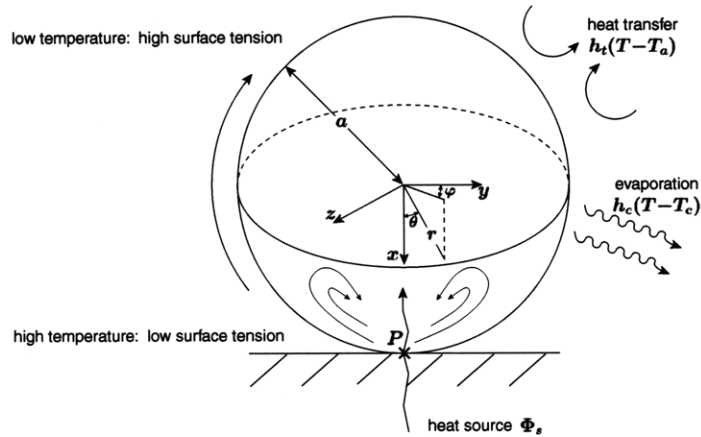


Figure 6-1: Schematic and notation for a droplet on a superhydrophobic surface.

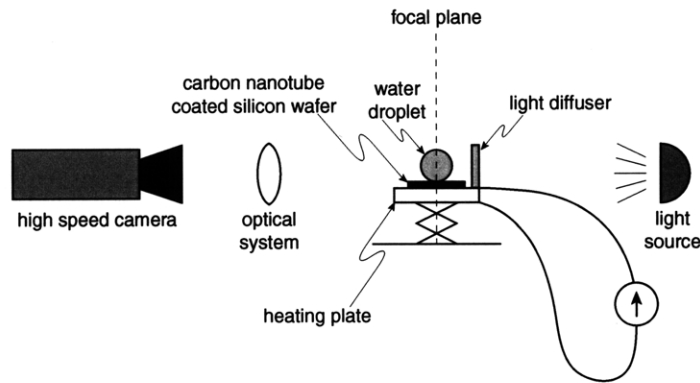


Figure 6-2: Schematic of the experimental setup.

silicon wafer coated with a vertically aligned carpet of carbon nanotubes (for details on the non-wetting properties and manufacture of the superhydrophobic surface see [97]. The radii of the droplets ranged between 0.4 – 0.6 mm and contact angles were near 180° (see Figure 6-3a). The superhydrophobic surface was heated from below via a heating plate with variable input current.

As soon as the liquid droplet is put in contact with the heated surface, the fluid is set in motion and convective structures develop. In order to visualize the temperature and velocity fields, both optical and infrared images of the droplet were taken. Figure 6-3b is a thermal image of the droplet taken with a FLIR Systems ThermoCAM infrared camera. This picture shows contours of constant temperature and reveals a temperature gradient inside the droplet that is roughly oriented towards

the contact point. The maximum temperature variation within the drop ranged from approximately $1 - 20^{\circ}\text{C}$ and the temperature of the substrate did not exceed 50°C .

Particle paths were visualized using a Phantom HSV v5.0 high speed camera at 400 fps in conjunction with a long-distance video microscope system (K2 Infinity). The droplets were illuminated from behind with a diffuse light source, as represented in figure 6-2. The image is focused on the thin glass capillary, which corresponds to the midsection of the droplet. The local velocity field within the droplet was measured by tracking small solid particles within the focal plane at the center of the droplet. Figure 6-3c) is a superposition of images taken with the experimental set up and showing the inner convective motion of the fluid. On this picture, the direction of the flow is given by particles moving downward in the center of the droplet. Particles within the focal plane appear as sharp points – although some residual blurry images of particles that are close to, but out of, the focal plane remain in the image. The characteristic velocity of the inner flow in the experiments was approximately $u_{\text{meas}} \approx 1 \text{ mm s}^{-1}$ and the characteristic time scale for one complete cycle of the convective structures was on the order of 1s. At the surface of the droplet, the fluid appears to be convected upwards, away from the heat source. In the focused midsection of the droplet, particles are accelerated downwards, away from the free surface towards the contact point P (see Figure 6-1 for notation). Also, particles that are initially out of the plane of focus are observed to move towards the focal plane and the contact point P . This suggests an axisymmetric toroidal geometry for the convective structures.

The experimental data was recorded for various values of heat input and drop size. It bears emphasis that for illustration purposes, pictures in figure 6-3(b) and (c) were taken using larger values of heat flux and brighter lightning than those used, when data was collected. In later experiments, the temperature at the heating plate was lowered in order to remain in the stable roll regime, and the light source was dimmed to avoid thermal contamination. Also, the “stem”, which can be seen at the top of the droplet in figure 6-3(c) is the glass capillary that was used to deposit the droplet. This capillary was removed before any data was recorded.

	Symbol	Value
Gravity	g	9.8 m s ⁻²
Density of water	ρ	9.982×10^2 kg m ⁻³
Dynamic viscosity of water	μ	1.002×10^{-3} kg m ⁻¹ s ⁻¹
Kinematic viscosity of water	ν	1.004×10^{-6} m ² s ⁻¹
Specific heat of water	C_p	4.182×10^3 J kg ⁻¹ K ⁻¹
Thermal conductivity of water	k_w	5.9×10^{-1} W m ⁻¹ K ⁻¹
Thermal conductivity of air	k_{air}	2.4×10^{-2} W m ⁻¹ K ⁻¹
Thermal diffusivity of water	κ	1.41×10^{-7} m ² s ⁻¹
Coefficient of thermal expansion	α_t	3.0×10^{-4} K ⁻¹
Change in surface tension due to temperature	$\alpha = \partial\sigma/\partial T$	-0.155×10^{-3} kg s ⁻² K ⁻¹
Latent heat of vaporization	L_v	2.454×10^6 J kg ⁻¹
Saturation temperature at atmospheric pressure	T_s	373 K
Atmospheric temperature	T_a	~ 295 K
Characteristic radius of the droplets	a	$\sim 0.5 \times 10^{-3}$ m
Characteristic convection speed	u_{meas}	$\sim 10^{-3}$ m s ⁻¹

Table 6.2: Characteristic values of relevant physical parameters.

On a clean carbon nanotube surface, the convective structures were observed to reach a steady state and were very stable. However, the observed structures are extremely sensitive to the substrate properties. As particles left by previous experiments accumulated on the substrate, the quality of the surface degraded and the stability of the observed convection rolls declined. After several seconds the structures would become unstable ultimately culminating in an unstructured swirling of the entire droplet. Owing to the extreme sensitivity of the convection pattern to the quality of the substrate, all the experimental data presented herein was taken on a clean, freshly-prepared surface.

6.3 Physical model

Consider a liquid of dynamic viscosity μ , density ρ , thermal conductivity k_w , specific heat C_p , saturation temperature T_s and latent heat of vaporization L_v . We assume that the carbon nanotube surface heats the liquid droplet of radius a at the contact point P on the surface and we neglect any radiative heat transfer. There are at least three possible mechanisms that could drive convection in the droplet: buoyant (buoyancy-driven) convection, Marangoni (surface tension-driven) convection, or

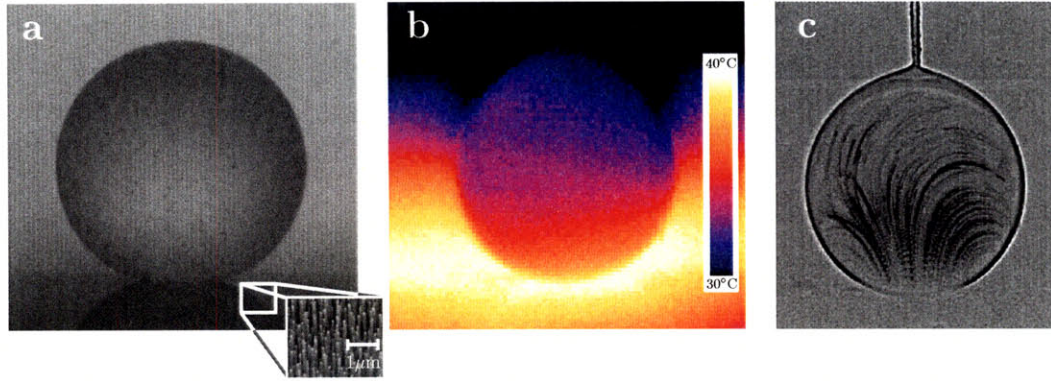


Figure 6-3: (a) Photo of a water droplet (0.5 mm radius) on a superhydrophobic surface seeded with silica tracer particles. The inset shows an SEM image of the surface coated with a carbon nanotube forest. (b) Thermal image of a drop deposited on the heated substrate. (c) Superposition of 20 consecutive snapshots of the water droplet taken at 10ms time intervals.

mass flow arising from spatially non-uniform evaporation, as in the “coffee stain” problem [49].

In our experiments there is clear evidence that the mechanism cannot be buoyancy as the rolls are going in the wrong direction – with a down-welling in the center of the droplet and an upflow at the interface. Furthermore, the Rayleigh number $Ra = \alpha_t g a^3 \Delta T / \nu \kappa$ in our experiment is roughly 50. Critical Rayleigh numbers characterizing the onset of buoyancy-driven instabilities are generally on the order of 10^3 depending on the geometry; for convection between two flat plates, the critical Rayleigh number is 1707, for a sphere under radial gravity it is 3091 [29]. Similarly, the convection in the “coffee stain” study relies on a combination of nonuniform evaporation and the pinning of the contact line. As our experiments are performed on a superhydrophobic surface, the contact line is free to move and we can rule out the coffee ring phenomenon. Finally, in our geometry, the temperature inside the droplet increases locally near the contact point creating a temperature gradient directed towards P . Since the surface tension of water increases as the temperature decreases, this temperature gradient generates a gradient in surface tension at the interface, which drives the fluid upwards at the surface of the droplet generating the experimentally observed vortex.

From simple arguments, it appears that the convection rolls may originate in thermocapillary effect. In order to confirm this hypothesis, we further investigate the time scales of the problem via a scaling analysis.

6.3.1 Scaling analysis

As observed by [141] “because flows actually powered by ... interfacial tension have been overlooked or misconstrued so often, there seems to be a need for simple criteria by which they can be recognized.” We can address this question in our particular geometry and determine under what conditions we expect to observe buoyant instead of Marangoni convection.

From (6.17) we find that the characteristic velocity of Marangoni flows scales like $U_M \sim \alpha\Delta T/\mu$. To find the characteristic velocity associated with buoyant convection, we balance the rate of viscous dissipation in the roll with the rate at which potential energy is gained as the heavier fluid descends:

$$\int \mu \nabla(\mathbf{u})^2 dV \sim \Delta\rho g U_B a^3. \quad (6.1)$$

The integral on the left scales as $\mu(U_B/a)^2 a^3$, hence the characteristic velocity associated with buoyancy-driven convection is $U_B \sim \Delta\rho g a^2/\mu$. This velocity can be also written $U_B \sim \alpha_t \rho g a^2 \Delta T/\mu$ with $\Delta\rho \sim \alpha_t \rho \Delta T$. Which convective instability is actually observed in the system depends on the characteristic time scales. In general, the instability with the fastest growth rate, or shortest characteristic time scale, will be the one that is observed. Thus, if we define a dimensionless number τ_B/τ_M , we expect to observe Marangoni convection if this number is large and buoyancy-driven convection if this number is small. Again, it is simple to distinguish between these two modes in an experiment as the rolls switch directions, rolling inward for Marangoni and outward for buoyancy. Estimating the size of τ_B/τ_M we find:

$$\frac{\tau_B}{\tau_M} \sim \frac{U_M}{U_B} \sim \frac{\alpha\Delta T}{\Delta\rho g a^2} \sim \frac{\alpha}{\alpha_t \rho g a^2} \quad (6.2)$$

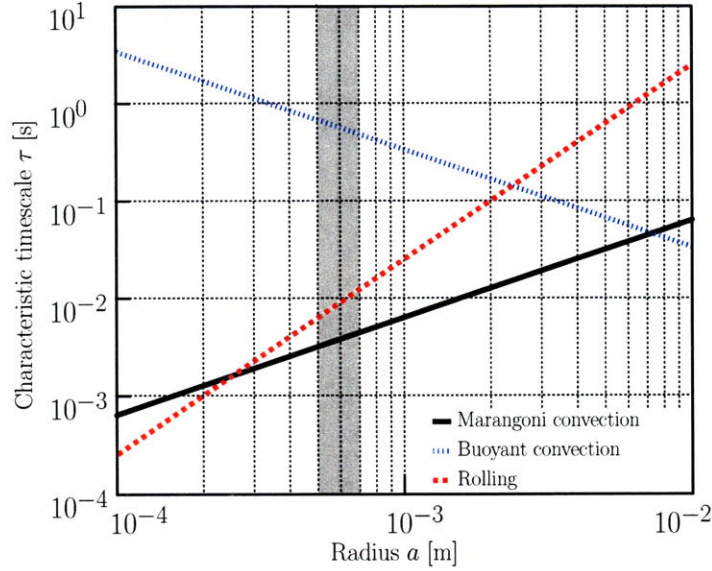


Figure 6-4: Characteristic timescales for various sizes of water droplets. The gray shaded region indicates the range of droplet sizes in our experiments. Material parameters correspond to those of water with $\Delta T = 1^\circ\text{C}$. Note that, as all three curves scale linearly with ΔT , changing the temperature difference does change the radius at which the curves intersect – rather it rescales the vertical axis.

It bears emphasis that this ratio of time scales corresponds to the ratio of the Marangoni number over the Rayleigh number $\tau_B/\tau_M = \text{Ma}/\text{Ra}$, with $\text{Ma} = \alpha a \Delta T / \kappa \mu$ and $\text{Ra} = \alpha_t g a^3 \Delta T / \nu \kappa$. As with convection in thin films, we expect to observe Marangoni convection for small length scales (i.e, in thin films and small drops) and buoyant convection for larger length scales (thicker layers and larger drops) [141]. For water, the transition to buoyancy-driven convection occurs around $a \gtrsim 1$ cm which is considerably larger than the droplets in our experiment.

However, this is not the whole story. Although we are far from the onset of buoyancy-driven convection in our experiment, there is another buoyancy-driven instability that one might expect to observe. Namely, as the fluid is heated from below, and cooled from above, we have the inherently unstable situation of a sphere with its center of mass above its geometric center point — hence, the droplet should roll. For a sphere, this instability should manifest for arbitrarily small Rayleigh numbers. In our experiments, we are saved from this complication because, in the neighborhood of the contact point, the sphere is slightly deformed giving the droplet a stabilizing

base. The extent and effectiveness of this finite size contact region can be calculated following the arguments of [106], and we find that the size of the contact region, ℓ , scales like the inverse Capillary number, ℓ_C , namely:

$$\ell \sim \frac{a^2}{\ell_C} = a^2 \sqrt{\frac{\rho g}{\sigma}}. \quad (6.3)$$

Again, the characteristic velocities and time scales associated with rolling can be computed by balancing the rate of potential energy gained by rolling with the rate of viscous dissipation. In this case, the viscous dissipation is restricted to the deforming contact region (as the rest of the drop is in solid body rotation):

$$\iiint \mu \nabla(\mathbf{u})^2 dV \sim \mu \left(\frac{U_R}{a}\right)^2 \ell^3 \sim \Delta \rho g U_R a^3 \quad (6.4)$$

Hence the characteristic velocity associated with the rolling instability U_R is given by $U_R \sim \Delta \rho g \ell_C^3 / (\mu a)$. Comparing the time scale associated with the onset rolling with that of buoyancy-driven convection, we find:

$$\frac{\tau_R}{\tau_B} \sim \frac{U_B}{U_R} \sim \frac{a^3}{\ell_C^3} = \text{Bo}^{\frac{3}{2}} \quad (6.5)$$

where Bo is the Bond number. Hence, rolling will manifest at small Bond numbers.

All three time scales are summarized in Figure 6-4 where the material parameters have been chosen for water. As one can see from the figure we expect to see transitions between the three types of instabilities as one varies the radius of the droplet. For very small drops, we expect to see rolling ($a \ll .3$ mm). This is consistent with our experimental observations as very tiny droplets either roll off the apparatus or, if they are pinned with a pipette, exhibit large swirling motions on the scale of the droplet. For droplet sizes ranging between (0.3 mm $\ll a \ll 7$ mm), we expect to observe Marangoni convection — namely toroidal convection rolls flowing inward. This is what was observed in the bulk of our experiments. Finally, for very large droplets ($a \gg 7$ mm) we expect to see a transition to buoyancy-driven convection. This parameter range was outside our regime of interest as the “droplets” are considerably

larger than the Capillary length and deviate considerably from the spherical geometry assumed herein. Hence we restricted our experimental data to droplets below this transition.

This scaling analysis confirms the hypothesis that the motion inside the droplet is due to a Marangoni effect and we therefore proceed to analyze the effects of surface tension gradients in our system. In the following subsection, both the momentum and the energy of the fluid are modeled, subject to the relevant boundary conditions.

6.3.2 Governing equations

In this analysis, we consider the small Reynolds number limit and neglect inertial effects within the drop. Thus, the governing equations for the fluid motion are the incompressible Stokes equations:

$$\nabla p = \mu \nabla^2 \mathbf{u}, \quad \nabla \cdot \mathbf{u} = 0 \quad (6.6)$$

where p and \mathbf{u} are the pressure and velocity fields within the droplet respectively.

The governing equation for the heat transfer problem is given by conservation of energy

$$\rho C_p \left(\frac{\partial T}{\partial t} + \mathbf{u} \cdot \nabla T \right) = k_w \nabla^2 T + \phi - \Phi_s \delta(\mathbf{r} - \mathbf{r}_0), \quad (6.7)$$

where ϕ is the viscous dissipation per unit volume and T is the temperature field within the droplet. In equation (6.7), the heat conduction term scales as $k_w \Delta T / a^2 \approx 10^6$ for a characteristic temperature difference inside the droplet of about 10K. On the other hand, the viscous dissipation term scales as $\mu u_{\text{meas}}^2 / a^2 \approx 10^{-3}$ and is therefore negligible relative to conduction. In this simple system, heat exchange takes a number of different forms — convection, conduction, and evaporation — at the boundary as summarized in Figure 6-1. The small region of contact between the hydrophobic surface and the droplet is modeled as a point heat source. We thus include a delta function at the contact point of intensity Φ_s , where Φ_s has units of J s^{-1} and \mathbf{r}_0 is the vector position of the contact point. Alternatively, the three-

dimensional delta function $\delta(\mathbf{r} - \mathbf{r}_0)$ in equation (6.7) can be written as $\delta(\mathbf{r} - \mathbf{r}_0) = \delta(|\mathbf{r} - \mathbf{r}_0|)/4\pi|\mathbf{r} - \mathbf{r}_0|^2$. Section 6.6 investigates the validity of the point heat source assumption on the solution.

Using values from Table 6.2, the characteristic time scales for heat advection and diffusion are given by

$$t_{\text{diff}} = \frac{\rho C_p a^2}{k_w} \approx 1 \text{ s} , \quad t_{\text{adv}} = \frac{a}{u_{\text{meas}}} \approx 1 \text{ s} . \quad (6.8)$$

In our experimental observations, the vortex structure was observed to be stable and unchanged for at least 60s. Thus, the convection rolls can reasonably be assumed to be a steady state phenomenon over the time scale of the experiment (which is at most a few seconds) and we neglect the time dependency in the energy equation.

The Péclet number, Pe , represents the ratio of the diffusive time scale over the advective time scale. A small Péclet number therefore characterizes a diffusion dominated heat transfer. Pe can be written as the product of the Reynolds number, Re , and the Prandtl number, Pr :

$$Pe = Re \cdot Pr . \quad (6.9)$$

Although not rigorously negligible throughout the entire domain in the experiments, the convective effects scale with Re as the Prandtl number is constant for a given fluid; for water, $Pr = \mu C_p / k_w \approx 7.2$. Therefore, the Péclet number is considered small in the following analytical study (to be consistent with the small Reynolds number assumption above), and diffusion is considered to be the major mode of heat transfer inside the droplet. The effects of a finite Péclet number are further explored in section 6.7. Thus the governing heat equation reduces to Poisson's equation for the temperature field:

$$k_w \nabla^2 T = \Phi_s \frac{\delta(|\mathbf{r} - \mathbf{r}_0|)}{4\pi|\mathbf{r} - \mathbf{r}_0|^2} . \quad (6.10)$$

Due to the point heat source approximation, the velocity and temperature field are expected to be singular. Therefore, some care must be taken in defining the Reynolds number as the velocity varies considerably within the droplet owing to

the mathematical singularity at the point of contact where both the temperature field and velocity field diverge. In this small region, neither the Péclet number, Pe , nor the Reynolds number are small. However, elsewhere (in more than 99 % of the volume of the droplet), the flows are slow and inertia is negligible ($Re \ll 1$) in both the experiment and in the analytical solution. If the neighborhood in which Re becomes significant is sufficiently small, we expect the model to capture the experimentally observed structures reasonably well away from the point of contact; however, one cannot expect the model to accurately reflect the behavior of the flow in the neighborhood of the singularity. In reality, this singularity is mitigated by the finite extent of the contact region; estimates on the size of this region are given in section 6.8.

6.3.3 Boundary conditions

At the surface of the droplet both heat transfer, via convection and conduction to the surrounding air, and evaporation tend to cool down the droplet. The convective and conductive heat transfer at the interface between the water droplet and the surrounding air is modeled with Newton's law of cooling [78], which can be written as

$$\phi_t = h_t(T - T_a) , \quad (6.11)$$

where ϕ_t is the total heat flux due to convection and conduction, h_t is the heat transfer coefficient and T_a is the ambient temperature.

The local energy loss due to evaporation can be written as

$$\phi_{\text{evaporation}} = J [C_p(T - T_s) + L_v] , \quad (6.12)$$

where J is the local mass flux due to evaporation. In our case $T - T_s \approx 60\text{K}$, thus $C_p(T - T_s) \approx 10^5 \text{ J kg}^{-1}$ and $L_v \approx 10^6 \text{ J kg}^{-1}$. Therefore, we neglect the first term in equation (6.12) and assume that latent heat of vaporization does not depend on temperature. The local mass flux J depends on a number of variables including the

temperature at the interface T , the pressure at the interface p , the relative humidity of the air H_m , and the local curvature R^{-1} . Over the time scale of the convective structure p , H_m and R^{-1} are all constant, and J can be written as a function of the local temperature T only. For small temperature differences, the mass flux J can be safely approximated as a linear function of T .

Combining the two terms ϕ_t (6.11) and $\phi_{\text{evaporation}}$ (6.12), the energy flux boundary condition at the surface of the droplet takes the form

$$-k_w \nabla T \cdot \mathbf{n} = h(T - T_0) , \quad (6.13)$$

where h is the effective total heat transfer coefficient, \mathbf{n} is the unit vector normal to the interface and T_0 is a reference temperature. Because the equation is linear in the temperature T , the reference temperature, T_0 , can be scaled out of the problem and does enter into our calculation.

The boundary conditions for Stokes equations (6.6) correspond to a stress balance at the surface of the droplet projected in the normal and tangential directions. The normal stress balance is replaced by the assumption that the droplet remains spherical. This assumption is experimentally satisfied because the Bond number, characterizing the ratio of gravity over surface tension, is small ($\text{Bo} = \rho g a^2 / \sigma \ll 1$) and because of the non-wettability of the substrate. The tangential stress balance can be written as follows:

$$\mathbf{t} \cdot \boldsymbol{\pi} \cdot \mathbf{n} = \mathbf{t} \cdot \nabla_s \sigma \quad (6.14)$$

where $\boldsymbol{\pi}$ is the stress tensor, \mathbf{t} is the unit vector tangent to the interface, ∇_s is the gradient along the surface and $\sigma = \sigma(T)$ is the surface tension. Thermocapillary effects arise due to gradients in surface tension, which again may be approximated as linear in temperature such that

$$\sigma = \sigma_a - \alpha \cdot (T - T_a) , \quad (6.15)$$

where σ_a is the surface tension at ambient temperature, T_a , and α is the first derivative

of the surface tension with respect to the temperature at T_a .

6.4 Analytical solution

The assumption that the Péclet number is small decouples the energy conservation equation from the Stokes equations (6.6). Therefore, (6.10) is solved first using the boundary condition (6.13). Equation (6.6) is then solved introducing the previously obtained solution for the temperature field in the boundary condition (6.14).

6.4.1 Nondimensionalization

The problem is nondimensionalized as follows:

$$\tilde{\mathbf{r}} = \mathbf{r}/L_{\text{ref}}, \quad \tilde{\mathbf{u}} = \mathbf{u}/u_{\text{ref}}, \quad \tilde{p} = p/p_{\text{ref}}, \quad \tilde{T} = (T - T_0)/\Delta T_{\text{ref}}, \quad (6.16)$$

using the scales

$$L_{\text{ref}} = a, \quad \Delta T_{\text{ref}} = \Phi_s/4\pi k_w a, \quad u_{\text{ref}} = |\alpha|\Delta T_{\text{ref}}/\mu, \quad p_{\text{ref}} = \mu u_{\text{ref}}/a, \quad (6.17)$$

where ΔT_{ref} is the characteristic temperature variation induced by a point heat source of intensity Φ_s and is obtained directly from the nondimensionalization of equation (6.10), and u_{ref} is the characteristic velocity induced by Marangoni stresses due to the temperature gradient. It should be noted that with this definition, u_{ref} is not expected to be small, as it represents the characteristic velocity at the surface due to the thermocapillary forcing, which we modeled as a singular forcing. Therefore, the velocity in the flow is only expected to be on the order of u_{ref} in the small contact region and should be much smaller in most of the droplet.

The governing equations for velocity, pressure (6.6) and temperature fields (6.10), as well as the boundary conditions (6.13) and (6.14) can be rewritten in dimensionless

form:

$$\nabla \tilde{p} = \nabla^2 \tilde{\mathbf{u}}, \quad (6.18)$$

$$\nabla \cdot \tilde{\mathbf{u}} = 0 \quad (6.19)$$

$$\nabla^2 \tilde{T} = \frac{\delta(|\tilde{\mathbf{r}} - \tilde{\mathbf{r}}_0|)}{|\tilde{\mathbf{r}} - \tilde{\mathbf{r}}_0|^2}, \quad (6.20)$$

$$-\nabla \tilde{T} \cdot \mathbf{n} = \text{Bi} \tilde{T}, \quad (6.21)$$

$$\mathbf{t} \cdot \tilde{\boldsymbol{\pi}} \cdot \mathbf{n} = \mathbf{t} \cdot \nabla_s \tilde{T}, \quad (6.22)$$

where $\text{Bi} = ha/k_w$ is the Biot number. The tildes on top of the dimensionless variables will be omitted in the following sections; henceforward, all variables are dimensionless unless otherwise noted.

6.4.2 Temperature field

The solution to equation (6.20) is obtained via separation of variables. Because the equation is linear, the solution can be written as the sum of the Green's function of the Laplacian with a singularity at \mathbf{r}_0 , and a continuous function that can be developed in Legendre polynomials. The problem is assumed to be axisymmetric and, in the spherical coordinate system defined in Figure 6-1, the solution to the heat problem can be written as the following summation:

$$T(r, \theta) = \frac{1}{(r^2 + 1 - 2r \cos \theta)^{\frac{1}{2}}} + \sum_{n=0}^{\infty} c_n r^n P_n(\cos \theta) \quad (6.23)$$

where P_n is the Legendre polynomial of order n .

By introducing (6.23) into the boundary condition (6.21), the coefficients, c_n , of the series can be directly identified and evaluated as

$$c_n = \frac{1 - 2\text{Bi}}{2(n + \text{Bi})}. \quad (6.24)$$

Details on this derivation can be found in appendix C.

6.4.3 Velocity field

For axisymmetrical fluid motions, the solution to the Stokes problem can be found in terms of Stokes' streamfunction ψ ([70]). The velocity field can be extracted from the the streamfunction using the following relations in spherical coordinates:

$$u_r = -\frac{1}{r^2 \sin \theta} \frac{\partial \psi}{\partial \theta}, \quad u_\theta = \frac{1}{r \sin \theta} \frac{\partial \psi}{\partial r}. \quad (6.25)$$

In spherical coordinates, Stokes equations (6.6) become

$$E^2 (E^2 \psi) = 0, \quad (6.26)$$

where

$$E^2 \equiv \frac{\partial^2}{\partial r^2} + \frac{\sin \theta}{r^2} \frac{\partial}{\partial \theta} \left(\frac{1}{\sin \theta} \frac{\partial}{\partial \theta} \right). \quad (6.27)$$

Using separation of variables, the solution to equation (6.26) can be written as the following series:

$$\psi(r, \theta) = \sum_{n=2}^{\infty} (R_n r^n + S_n r^{-n+1} + T_n r^{n+2} + U_n r^{-n+3}) C_n^{-1/2}(\cos \theta), \quad (6.28)$$

where $C_n^{-1/2}$ is the Gegenbauer polynomial of order n and degree $-1/2$ defined as

$$C_n^{-1/2}(\cos \theta) = \frac{1}{2n-1} [P_{n-2}(\cos \theta) - P_n(\cos \theta)] \quad \text{for } n \geq 2. \quad (6.29)$$

Details on the derivation of the solution to equation (6.26) may be found in [70]. The streamfunction (6.28) is then introduced in the boundary condition for the Stokes flow (6.22) using (6.25), which takes the following form in spherical coordinates:

$$r \frac{\partial}{\partial r} \left(\frac{u_\theta}{r} \right) + \frac{1}{r} \frac{\partial u_r}{\partial \theta} = -\frac{\partial T}{\partial \theta} \Big|_{r=a}. \quad (6.30)$$

Identifying the coefficients P_n , Q_n , R_n and S_n in equation (6.28) yields an analytical

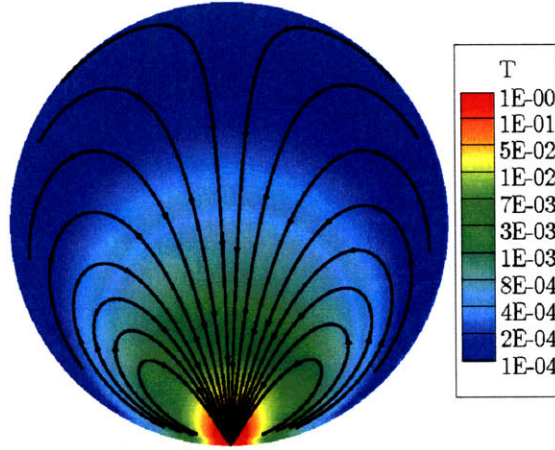


Figure 6-5: Analytic solution of the temperature field and corresponding streamlines. The colormap represents the dimensionless analytical temperature field for $Bi = 800$ and the black arrows represent the streamlines of the flow in the centerplane defined by $\varphi = 0$. The analytical solution is computed using $n = 100$ terms in the expansion.

expression for the streamfunction

$$\psi(r, \theta) = -\frac{1}{8}(1-r^2) \left[1 + r \cos \theta - \frac{1-r^2}{(r^2+1-2r \cos \theta)^{1/2}} + \sum_{n=2}^{\infty} \frac{(n-1) - (2n-1)Bi}{(2n-1)((n-1)+Bi)} r^n (P_{n-2}(\cos \theta) - P_n(\cos \theta)) \right]. \quad (6.31)$$

Details on this derivation can also be found in appendix C. Using equations (6.23) and (6.31), the temperature field and streamfunction can be easily computed. Figure 6-5 shows the temperature field (6.23) and the streamlines (6.31). The convergence of the sums in the expressions for the temperature field and the streamfunction in equations (6.23,6.31) is dependent on the Biot number, Bi . For higher values of Bi , more terms need to be computed in order to accurately approximate the solution. From the form of the coefficients, we expect the number of terms required to increase linearly with Bi . Finally, the velocity field components, u_r and u_θ , can be deduced from equation (6.31) using equations (6.25).

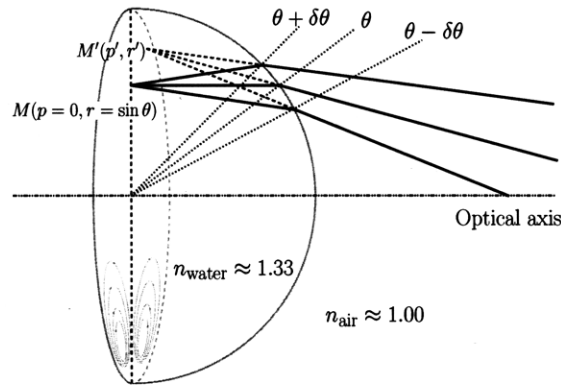


Figure 6-6: Schematic ray-tracing diagram of the geometrical optics for a spherical liquid droplet.

6.5 Experimental validation of the model

Using the experimental setup described in section 6.2, data was collected for a variety of heat fluxes and drop sizes. The velocity of the flow at different locations was determined by tracking particles. Following this procedure, details of the fluid flow inside the droplet were experimentally reconstructed and compared to the analytical solution developed in section 6.4.3.

6.5.1 Optical correction for spherical droplet

In order to compare the experimentally observed flow field to the analytical solution, we need to correct the observed particle displacements for the optical deformation induced by the fluid droplet itself. The image plane from the midsection of the droplet is focused on the CCD chip of the high-speed camera through the optical system (see Figure 6-2). However, the hemispherical droplet of water acts as an additional lens between the midsection of the droplet and the optical system (see Figure 6-6). Applying the Snell–Descartes law [68] to light rays close to the optical axis, the system is found to be stigmatic to the first order and the image of an object

$M(0, r)$ in the midsection appears at the point $M'(p', r')$ (see Figure 6-6) such that

$$p' = g(r) = -\frac{n_{\text{water}}}{n_{\text{air}}}r \sin \left[\arcsin r - \arcsin \left(\frac{n_{\text{water}}}{n_{\text{air}}}r \right) \right], \quad (6.32)$$

$$r' = f(r) = \frac{n_{\text{water}}}{n_{\text{air}}}r \cos \left[\arcsin r - \arcsin \left(\frac{n_{\text{water}}}{n_{\text{air}}}r \right) \right], \quad (6.33)$$

where r is the distance from the object to the optical axis (recall that lengths have been scaled by the drop radius), r' the distance from the image to the optical axis, p' the distance from the image to the midsection plane of the droplet, n_{water} the index of refraction of water and n_{air} the index of refraction of air. The optical distortion increases with distance from the optical axis. When applied to the raw data, this analysis provides a correction of approximately 17 % (of the radius) for $r = 0.65$, which is the upper limit of our recorded data.

6.5.2 Experimental and analytical results comparison

To compare the analytical solution of the flow field to the experiment, the velocity profile along the x -axis was measured by tracking particles in the focal plane whose trajectories remained close to the x -axis, defined by $\theta = 0$ in spherical coordinates (see Figure 6-1). The observed position x' of the particle along the axis and its velocity $|\mathbf{u}'|$ were recorded and the real position $x = r$ along the x -axis and velocity $|\mathbf{u}| \approx |u_x|$ were deduced by correcting for optical deformation as described in section 6.5.1, $x = f^{-1}(x')$ and $|\mathbf{u}| = \frac{d}{dx}f^{-1}(x')|\mathbf{u}'|$. Several experiments were performed for different magnitudes of the heat source, Φ_s , as summarized in Table 6.3. The heat flux, Φ_s , was evaluated by measuring the rate of change of the radius of the droplet, which is related to the evaporation loss. Assuming that the bulk of the energy transfer was used in the phase transition, the heat flux is approximated as $\Phi_s \approx 4\pi a^2 \frac{da}{dt} \rho L_v$. The radius of the droplet was roughly half a millimeter in all three experiments. The heat source intensity on the other hand varied significantly between the different experiments (see Table 6.3). The velocities measured inside the droplets were nondimensionalized using the scaling described in equation (6.17).

	a in mm	Φ_s in J s^{-1}	ΔT_{ref} in K	u_{ref} in m s^{-1}
Experiment 1	0.534	0.0139	3.51	0.54
Experiment 2	0.681	0.0453	8.97	1.39
Experiment 3	0.664	0.0657	13.34	2.06

Table 6.3: Summary of the experiments

Figure 6-7 shows the nondimensional flow velocities from all three experiments measured along the x -axis and Figure 6-8 represents the experimentally observed particle pathlines plotted on top of the streamfunction as computed for $\text{Bi} = 800$. Streamlines were recorded experimentally by tracking one particle over an extended period of time. The different sets of data shown in Figure 6-7 all collapse onto one curve as anticipated, which validates the scaling. Additionally, this confirms that, in the low Reynolds number and low Péclet number regime, the internal dynamics and heat transfer of the droplet only depend on one nondimensional parameter, the Biot number. Finally, an important observation, which can be made by looking at the velocity profile in figure 6-8, is that the experimental data validates our initial assumption of a localized heat source at the contact point. In fact, the experimental data itself shows a singular-like increase in the velocity of the flow between the center of the drop and the contact point. Experimental data can only be recorded up to a distance of 65 % of the radius a away from the center, because of optical limitations. Over this distance, the increase in velocity, which is measured experimentally, is of more than a factor of ten and strongly suggests that the flow velocities close to the contact point are indeed fairly high.

The only parameter that is not explicitly known in the experiment is the effective heat transfer coefficient, h , which appears in the Biot number. To calculate the analytic velocity profile in Figure 6-7, we first computed a family of profiles along x , each profile corresponding to a different Bi , and fit the data by minimizing the error between the analytical solution and the experimental data. The fitted Biot number has a value of $\text{Bi} = 800$, which corresponds to a generalized heat transfer coefficient of $h \approx 7.1 \times 10^5 \text{ W m}^{-2}\text{K}^{-1}$. For this Biot number, the analytical solution and the

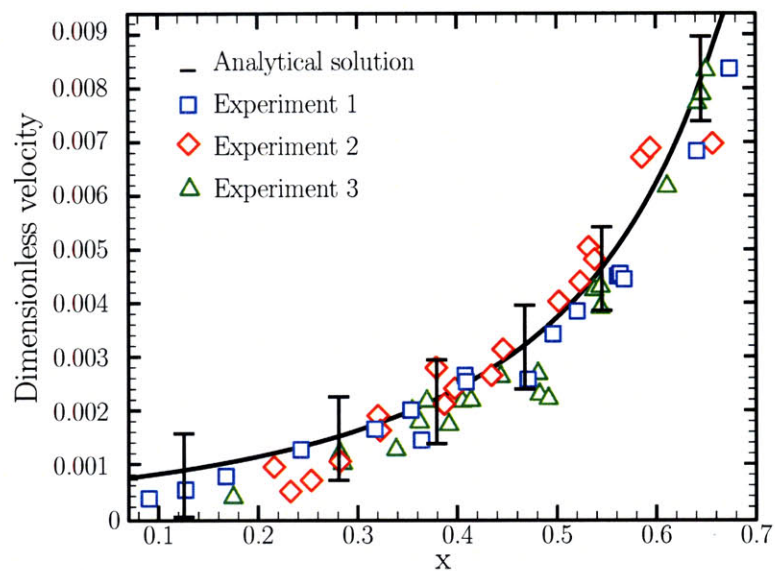


Figure 6-7: Analytical and experimental velocity profile, $|\mathbf{u}|$. The spatial variable x represents the dimensionless coordinate along the x -axis: $x = 0$ lies at the center of the droplet, $x = 1$ lies at the contact point. The black line represents the analytic velocity profile in the drop for $Bi = 800$. Different symbols correspond to three sets of data with heat sources of different intensity. Error bars give an estimate of the error in measuring the velocity of a particle by extracting the position of its centroid in successive frames and hence are a reflection of the resolution of the image.

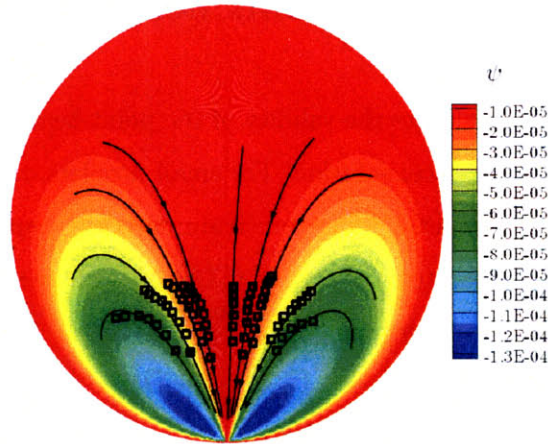


Figure 6-8: Analytical and experimental streamlines. The colormap represents the analytical streamfunction; black lines represent particular streamlines computed analytically; black squares represent experimentally recorded particle trajectories. The analytical solution is computed using $n = 100$ terms in the expansion.

experimental data are in extremely good agreement.

The fitted value for the heat transfer coefficient h can be compared to the value of the coefficient in the case of a sphere in quiescent air, for which the heat loss is only due to diffusion. For this system, the heat transfer coefficient is on the order of $10^2 \text{ W m}^{-2}\text{K}^{-1}$, corresponding to the small Biot number limit in which only small temperature gradients are expected inside the sphere. This observation suggests that, in our case, evaporation is the dominant form of heat transfer from the droplet to the surrounding air and thus $h \approx h_e$. This is consistent with our heat flux estimations, since we have chosen $\Phi_s \approx \iint \phi_{\text{evaporation}} dS$.

However, even for heat transfer in systems involving phase changes (which can easily achieve h 's on the order of 10^4 or $10^5 \text{ W m}^{-2}\text{K}^{-1}$), our value is quite high and we believe that, in neglecting convective transport (i.e. assuming small Péclet number everywhere) we are perhaps overestimating h . While our results are correct to first order, the addition of convective effects would tend to smooth out the temperature gradient near the singularity, lowering the effective heat transfer coefficient. A quantitative analysis of the first order effects of finite Pe is included at the end of the chapter in section 6.7.

6.6 Validity of the point heat source assumption

In this section, we investigate the validity of the point heat source assumption, which leads to a singular analytical solution. For small droplets, the radius ℓ of the contact region between the droplet and the substrate decreases rapidly as suggested by the scaling giving in equation (6.3) of section 6.3.1. In our experiments, the ratio between the radius of the contact region and the radius of the droplet is on the order of $\ell/a \approx 10\%$ (see Figure 6-3).

In the following, the heat source is no longer modeled as a singular heat source but rather as a distributed heat source. The governing equations for the heat problem (6.10, 6.13) are replaced by

$$k_w \nabla^2 T^\alpha = 0 , \quad (6.34)$$

$$-k_w \nabla T^\alpha \cdot \mathbf{n} = h(T^\alpha - T_0) + \frac{\Phi_s}{4\pi a^2} f^\alpha(\cos \theta) , \quad (6.35)$$

which can be written in nondimensional form

$$\nabla^2 T^\alpha = 0 , \quad (6.36)$$

$$-\nabla T^\alpha \cdot \mathbf{n} = \text{Bi} T^\alpha + f^\alpha(\cos \theta) . \quad (6.37)$$

The function $f^\alpha(\cos \theta)$ characterizes the distribution of the heat source and is subjected to the normalization constrain

$$\int_0^\pi f^\alpha(\cos \theta) \sin \theta d\theta = 2 . \quad (6.38)$$

Here we consider a sequence of functions f^α defined as follow:

$$f^\alpha(\cos \theta) = \begin{cases} \frac{6(\cos \theta - \cos \alpha)^2}{(1 - \cos \alpha)^3} & 0 \leq \theta \leq \alpha, \\ 0 & \alpha \leq \theta \leq \pi. \end{cases}$$

α characterizes the area over which the heat source is distributed. For small α , this

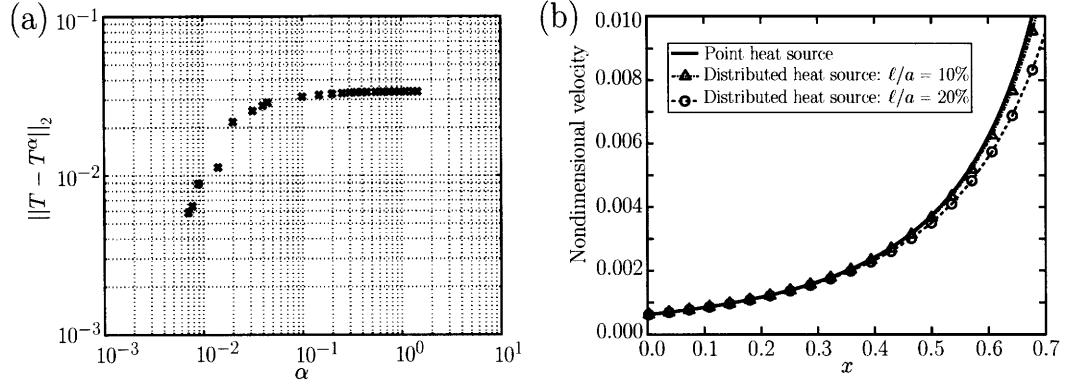


Figure 6-9: a) Error $\|T - T^\alpha\|_2$ as a function of α showing the convergence of the sequence T^α to the point heat source solution T . b) Velocity profile $|\mathbf{u}|$ along the x -axis for the point heat source solution and for distributed heat source solutions with $\ell/a = 10\%$ and 20% .

sequence of functions converges to a delta function.

A derivation similar to the one presented in appendix C yields the following expressions for the temperature field and the streamfunction:

$$T^\alpha(r, \theta) = \sum_{n=0}^{\infty} \frac{f_n^\alpha}{n + \text{Bi}} r^n P_n(\cos \theta), \quad (6.39)$$

$$\psi^\alpha(r, \theta) = \sum_{n=2}^{\infty} -\frac{n(n-1)f_{n-1}^\alpha}{2(2n-1)(n-1 + \text{Bi})} (r^n - r^{n+2}) C_n^{-1/2}(\cos \theta), \quad (6.40)$$

where

$$f_n^\alpha = \frac{2n+1}{2} \int_{-1}^1 f^\alpha(x) P_n(x) dx. \quad (6.41)$$

Figure 6-9(a) shows the convergence of the solution T^α for a distributed heat source to the solution T for a point heat source as α goes to zero (i.e.: the surface area over which the heat source is distributed goes to zero). Figure 6-9(b) shows the magnitude of the flow velocity along the x -axis within the region of the droplet that can be observed experimentally (see figure 6-7). The velocity profile for a heat source distributed over 20 % of the radius is already very close to that of a point heat source and it is even more so for a source distributed over 10 % of the radius. As expected the distribution of the heat source only affects the solution of the flow in the vicinity of the contact region.

In the present study, the model is compared to experimental results in a region of the droplet far enough from the contact region (see figure 6-9b). Hence, our original assumption of a point heat source is valid and accurate enough to allow comparison between our experimental data and the analytical expression for the flow and temperature fields.

6.7 Effect of finite Péclet number

The only major physical phenomenon, which we neglected in our analytical study and which is susceptible to affect our results, is the advection of heat. In this section, we investigate the first order effect of a finite Péclet number on the steady state temperature, pressure and velocity fields. For a finite Péclet number, the governing equations in nondimensional form can be written

$$\nabla^2 T - \frac{\delta(|\mathbf{r} - \mathbf{r}_0|)}{|\mathbf{r} - \mathbf{r}_0|^2} = \text{Pe } \mathbf{u} \cdot \nabla T, \quad (6.42)$$

$$\nabla^2 \mathbf{u} = \nabla p, \quad (6.43)$$

$$\nabla \cdot \mathbf{u} = 0, \quad (6.44)$$

$$-\nabla T \cdot \mathbf{n} = \text{Bi } T, \quad (6.45)$$

$$\mathbf{t} \cdot \boldsymbol{\pi} \cdot \mathbf{n} = \mathbf{t} \cdot \nabla_s T. \quad (6.46)$$

The fields are each split into two terms: $\mathbf{u} = \mathbf{u}_0 + \mathbf{u}_1$, $T = T_0 + T_1$ and $p = p_0 + p_1$, where the subscript “0” represents the known analytical solution to the zero Péclet number problem (6.23 and 6.31) and the subscript “1” represents the perturbation fields due to the nonlinear advection term for finite Péclet number. This splitting scheme is introduced in equations (6.42-6.46). The solution (\mathbf{u}_0, p_0, T_0) to the linear system with a point heat source is subtracted from the finite Péclet number system, leading to a set of equations for the perturbation field (\mathbf{u}_1, p_1, T_1) . These equations are discretized using finite differences and the full nonlinear system is solved using

the following iteration scheme

$$\nabla^2 T_1^{n+1} - \text{Pe} (\mathbf{u}_0 + \mathbf{u}_1^n) \cdot \nabla T_1^{n+1} = \text{Pe} (\mathbf{u}_0 + \mathbf{u}_1^n) \cdot \nabla T_0, \quad (6.47)$$

$$\nabla^2 \mathbf{u}_1^{n+1} = \nabla p_1^{n+1}, \quad (6.48)$$

$$\nabla \cdot \mathbf{u}_1^{n+1} = 0, \quad (6.49)$$

$$-\nabla T_1^{n+1} \cdot \mathbf{n} = \text{Bi} T_1^{n+1}, \quad (6.50)$$

$$\mathbf{t} \cdot \boldsymbol{\pi}_1^{n+1} \cdot \mathbf{n} = \mathbf{t} \cdot \nabla_s T_1^{n+1}. \quad (6.51)$$

The iteration procedure is stopped once the convergence criterion $\|\mathbf{u}_1^{n+1} - \mathbf{u}_1^n\|_2 \leq \epsilon$ is satisfied.

When the advection term is included, cool water is advected downwards through the center of the droplet towards the contact point, which lowers the temperature in this region. Similarly heat is removed from the contact region and advected to the sides of the droplet, which reduces temperature gradients. The general effect is to decrease the Marangoni stress at the surface of the droplet and thus, for a given Biot number, we expect to observe smaller velocities. Hence, increasing the Péclet number has a similar effect on the velocity field as increasing the Biot number: both tend to lower the temperature gradient at the surface and as a consequence the Marangoni stress. Therefore, it is expected that for a given Péclet number the Biot number required to fit the experimental data will be lower than the first order estimate in which we neglected heat advection.

This can be seen on figure 6-10(a). Consider the velocity profile along the $\hat{\mathbf{x}}$ -axis for a Biot number of $\text{Bi} = 600$ and a Péclet number of $\text{Pe} = 3500$. This velocity profile is very similar to the velocity profile for $\text{Bi} = 650$ and $\text{Pe} = 0$. In this case, we call effective Biot number $\text{Bi}^{\text{Eff}} = 650$, the Biot number which has the most similar velocity profile when heat advection is neglected ($\text{Pe} = 0$). It can be seen that a finite Péclet number has a similar influence on the velocity profile along the $\hat{\mathbf{x}}$ -axis as an increasing effective Biot number. Note that although a Péclet number of $\text{Pe} = 3500$ seems to be very large in this calculation, the heat advection term remains small in

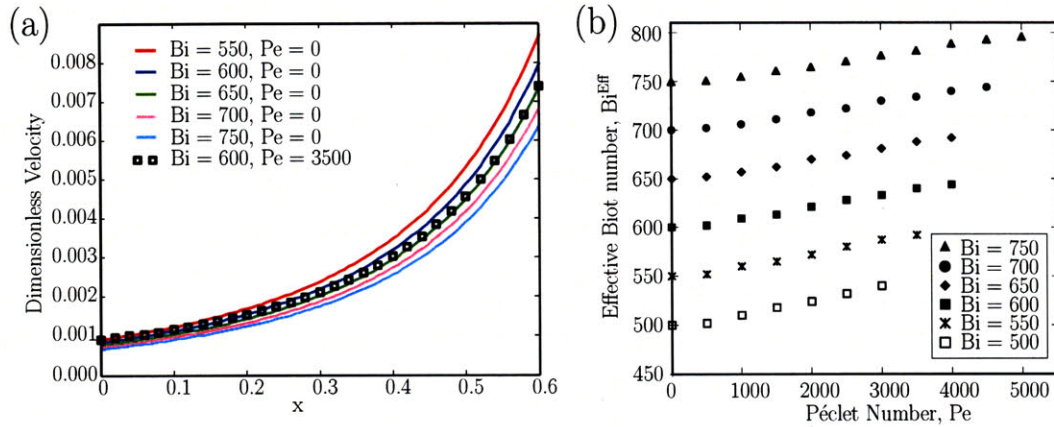


Figure 6-10: (a) Effect of increasing Biot number and increasing Péclet number on the velocity along the x -axis. (b) Apparent biot number for which the velocity profile of the numerical solution along the x -axis best fits the experimental data as a function of the Péclet number.

most of the droplet and is only finite and non negligible around the contact region. This is because the Péclet number is proportional to the reference velocity u_{ref} used in the nondimensionalization, which is large and characteristic of the velocity induced close to the heat source singularity (see section 6.4.1). The value of the Péclet number computed with the flow velocity measured at the center of the droplet would still be small as discussed in section 6.3.2.

Figure 6-10(b) further characterizes the increase in effective Biot number as the Péclet number is increased for a fixed Biot number. The effective Biot number is found by minimizing the error between the velocity profile for a given Biot and Péclet number and the velocity profiles for a given Biot number and no heat advection. As expected, the effective Biot number always increases with increasing Péclet number indicating that, by neglecting heat advection, our lowest order model is likely to overestimate the Biot number and the effective heat transfer coefficient. The gravity of the error is illustrated in Figure 6-10(b), when the heat advection remains small and the governing equation are only weakly nonlinear.

6.8 Discussion

In conclusion, we have observed convective structures inside water droplets sitting on superhydrophobic surfaces. A physical model has been proposed, suggesting that these structures arise due to thermocapillary-driven Marangoni convection. Because the Reynolds number and Péclet number are small and viscous dissipation is negligible, the heat transfer and fluid momentum problems decouple. It is then possible to find a solution analytically in terms of Gegenbauer polynomials. This solution has the form of a toroidal vortex and compares favorably with experimental measurements of particle pathlines inside the drop. By matching the Biot number from experimental observations to the numerical simulation, we are able to estimate the effective heat transfer coefficient $h \approx 7.1 \times 10^5 \text{ W m}^{-2}\text{K}^{-1}$ for droplets sitting on hot hydrophobic surfaces.

It may come as a surprise that, in our physical model, the dynamics of the system depends on only one dimensionless parameter, Bi, whereas a standard dimensional analysis would predict four relevant dimensionless groups: the Reynolds number, Re, the Péclet number, Pe, the Biot number, Bi and the Marangoni number, $\text{Ma} = \alpha a \Delta T / \kappa \mu$. However, recall that as a first approximation, both the Reynolds number and the Péclet are assumed to be small. Since $\text{Pe} = \text{Re} \cdot \text{Pr}$, the Reynolds number and the Péclet number cannot be varied independently without changing the material properties of the fluid. This assumption reduces the number of independent dimensionless groups to two. Furthermore, the governing equations are linear in velocity thus the velocity scale may be chosen to eliminate a third dimensionless group. By using the characteristic Marangoni velocity, $\alpha \Phi_s / \mu k_w$, as a reference velocity, the Marangoni number can be eliminated from the dimensionless governing equations. Thus, the small Reynolds number assumption combined with the linear structure of the governing equations leaves only one dimensionless parameter, Bi. Note however that the *dimensional* velocities still scale linearly with the Marangoni number.

Furthermore, the analysis could be extended to include the influence of finite Pe and Re by including a small Pe and Re perturbation about the base state computed

herein. This introduces a weak coupling between the fluid flow and the heat transfer, ultimately yielding a dimensionless heat transfer correlation function for the Biot (or Nusselt) number as a function of Re , Pe and Ma . The first order effects of finite Péclet number are described in section 6.7, however a detailed analysis is beyond the scope of the present study.

Finally, beyond heat transfer implications discussed herein, it is quite remarkable to see how regular and stable this self-generated and self-sustained flow pattern is. It could be interesting to further investigate, what kind of Marangoni driven flow patterns could be generated and controlled at the microscale. Such controllable convective patterns could be exploited to enhance micromixing in fluid droplets [46] and also possibly as an original microbiological assay [30].

Chapter 7

Conclusions and outlook

7.1 Summary

In this thesis, we have presented a collection of work related to problems of motion, transport and mixing in the inertialess low Reynolds number regime. While most of the work consists of modeling and understanding the behavior of dynamical systems at the micron scale, conclusions and observations are presented in the context of relevant biological systems or compared to results obtained from direct experimentation.

Chapter 2 through chapter 5 present a detailed analysis of the locomotion of self-propelled microswimmers. Chapter 2 describes the modeling approach and optimization framework developed in order to investigate optimal swimming strategies for deforming slender bodies at low Reynolds number. A brief discussion about the physical significance of swimming efficiency demonstrates the relevance of optimizing stroke kinematics for microswimmers.

In chapter 3, we apply our modeling framework to a historical figure first introduced by E.M. Purcell in the discussion of low Reynolds number swimming: the three-link swimmer. In this chapter we discuss the existence and characteristics of well-defined optimal stroke kinematics, which are found for this simple system. The influence of the geometry of the swimmer is also investigated and swimmers are found to perform better as they become increasingly slender, particularly in the limit of a slenderness similar to those observed in biological systems. We also investigate the

efficiency of large amplitude strokes and find that, while they do exhibit better efficiencies in the unphysical limit of infinite slenderness, their performances decrease drastically as the slenderness is decreased. The efficiency of such stroke is well-below the reported efficiency of our optimal stroke for any realistic value of the slenderness. In the three-link case, the optimization procedure is found to perform well and to converge towards an infinitely differentiable solution, which appears to be a global optimum.

The modeling framework used for the three-link swimmer has been generalized in order to represent flagellated swimmers, which are biologically more relevant. This generalized framework is described in chapter 4. We first look at a single-tail swimmer with no head attached. In this case, the effectiveness of the optimization procedure is first verified against what is analytically known to be an optimal periodic traveling wave solution: the saw-tooth wave. We find that our procedure converges to the analytical saw-tooth regardless of the initial guess. We then use our method on a typical unflagellated swimmer with a spheroidal head and dimensions comparable to sperm cells and find that regardless of the initial guess, optimal strokes are always found to be traveling waves propagating from the base of the head to the end of the flagellum. This suggests that microorganisms using this mode of locomotion are in fact using an optimal swimming strategy. For such unflagellated swimmers the waveform is found to evolve as it propagates down the tail. The curvature of the centerline is initially higher as the wave takes form at the base of the head and decreases slightly as the wave propagates. We further investigate the influence of the geometry of the unflagellate on the swimming efficiency. For the geometry of the head, we find that there is a trade-off between minimizing the axial drag coefficient and maximizing the normal drag coefficient, as both lead to increase in efficiency. We also find the existence of an optimal tail length for a given head size, which lead to an optimal geometry criterion. Further looking at published data on sperm morphometry for all mammalian species, we find that this criterion is reflected in biological microswimmers.

Chapter 5 presents a study of biflagellated swimmers using a more general for-

mulation of our model, which is able to consider multiple flagella. This analysis is inspired by the experimental observations of stroke patterns of the green algae *chlamydomonas*, which is known to undergo strokes which are structurally different: an undulatory stroke, which resembles traveling waves observed in many smaller unflagellated organisms and a breaststroke, which resembles the effective-recovery stroke observed in larger ciliates. In the case of biflagellates, the optimization procedure is observed to converge to different local optima, depending on the initial guess for the stroke and whether a swimming or feeding efficiency is considered. All experimentally observed strokes are found to be local hydrodynamic optima. Undulatory strokes are found when optimizing for swimming efficiency and starting from small amplitude strokes. Breaststrokes are always found when optimizing for feeding efficiency, regardless of the initial guess and are also found when optimizing for the swimming efficiency, with the initial guess being the feeding efficient breaststroke. Hence the breaststroke is found to be efficient both for swimming and for generating feeding currents, which can enhance transport of nutrient uptake. Undulatory strokes are found to be only locally optimal for swimming. An important observation from our investigation of both unflagellates and biflagellates is that all biologically observed stroke patterns are found to be hydrodynamical optima, with no further consideration of the internal dynamics of the swimmer. This fact strongly emphasizes the crucial role of the hydrodynamics in the internal self-organization of the flagellum.

A final investigation of self-organized mixing and transport at low Reynolds number is presented in chapter 6. We no longer consider biological systems and look at self-sustained and regular convective structures in microdroplets. Experiments are performed on small droplets sitting on top of superhydrophobic substrates for which the contact angle approaches 180° . Upon heating of the substrate, a self-sustained toroidal convective roll is observed and experimental data is recorded. We perform a scaling analysis which shows that this mixing pattern originates in thermocapillary Marangoni flow at the surface of the droplet. An analytical solution for the temperature and velocity fields inside the droplet is derived in the limit case of a inertialess and diffusion dominated system characterized by small Reynolds and Péclet num-

bers. The solution agrees with experimental data. The effect of non-negligible heat advection, characterized by a finite Péclet number, is investigated numerically.

7.2 Future work

The present investigation lays the groundwork for further complementary studies, which could be addressed by extending and improving methodologies developed in this thesis. It also raises new questions, which will require the development of new tools.

Cilia

A direct extension of the work presented herein would be to conduct a similar study on a single cilium in order to see whether the effective/recovery stroke is optimal from a hydrodynamic standpoint. Given the recent technological interest in designing artificial cilia for microfluidic applications, this procedure would allow one to find cilia strokes, which are effective at moving or mixing the fluid, depending on the needs of the particular application. This would constitute an extremely useful tool in the design of artificial cilia devices. Furthermore, recent studies have suggested that hydrodynamic interactions may be responsible for the metachronal wave observed in beating cilia [66]. Thus, it would be interesting to extend the study to an array of cilia beating collectively and investigate the relevance of metachronal coordination and phase differences between adjacent cilia with regard to motility. Some insight could be found as to whether cilia exhibit optimal self-controlled locomotion. This study would require a more efficient implementation of hydrodynamic interactions (as it is done in suspensions simulations for instance [158,159]) in order to handle the increasing complexity of the system.

Interacting swimmers

The coordination of cilia further opens the door to the investigation of collective and synchronized behavior at low Reynolds number. Such phenomena are in fact a dom-

inant aspect of the motility of microorganisms and give rise to extremely complex dynamics. Recently, the effect of coordination on transport, mixing and diffusion has been investigated in colonies of *chlamydomonas* (volvox) [145,147] as well as suspensions of microswimmers [44,72,138]. In general, accurate numerical representation of both the near and far field hydrodynamic interactions in such systems is extremely challenging owing to the large number of interacting free agents. Looking at a simple system made of two interacting swimmers could give insights as to how and why coordination occurs as well as the existence of stable, unstable or oscillatory cooperative swimming configurations.

Suspensions of swimmers

Transport properties in swarming suspensions of microswimmers have been studied numerically by several authors, who computed and tracked the exact motion of a large number of interacting swimmers [44,72,138]. These computations are fully deterministic and the time integration of each trajectory requires the evaluation of all the interaction terms in addition to imposing the force and torque free conditions on each swimmer. However, experimental video recordings of swarming colonies of bacteria show what appears to be a highly stochastic phenomenon. It would be interesting to develop a statistical framework for the analysis of such suspensions.

Rolling spheres on superhydrophobic surfaces

Finally, it could be interesting to follow our investigation of thermocapillary driven convection, with a stability analysis of the toroidal convective roll. The scaling analysis in section 6.3.1 suggests that the convective inner motion of the droplet can become unstable because of the rolling instability due to the gradient in density. This instability has in fact been observed experimentally, although it could not be reproduced systematically. It has been further observed that in such cases, when the droplet begins to roll, it can spontaneously depart and accelerate at the surface of the substrate. Inducing motion of droplets on a solid substrate has been achieved through chemical gradients [7,82] or electric fields [67]. If controlled, this mechanism could

have interesting applications as it would provide a purely mechanical mechanism to transport small amounts of fluid.

Appendix A

Three-link swimmer coefficients

In this appendix, we describe the expressions of all parameters used in the model of the hydrodynamics around the three-link swimmer. All notations used for the geometry of the three-link swimmer have been introduced in section 3.2.1. Let s_i be the arc-length along the centerline of the nodes between two links such that $s_{i+1} = s_i + 2L_{i+1}$ and $s_0 = 0$. The center of each link is defined by the arc-length σ_i such that $\sigma_{i+1} = \sigma_i + L_{i+1} + L_i$ and $\sigma_0 = 0$.

A.1 Expression for drag coefficients

The expressions for the matrices \mathbf{A}_i^j given in equation (3.5) are evaluated by splitting all integrals over each link. We assume that the point of arc-length s is on the i^{th} link, such that $s \in [s_{i-1} \ s_i]$. The local hydrodynamic force $\mathbf{f}_i(s)$ at s is given by equation (3.2) and the subscript i is simply a reminder that s is on the i^{th} . It can be readily seen in equation (3.2) that the local hydrodynamic force $\mathbf{f}_i(s)$ depends on the velocity distribution along the entire swimmer. We reformulate equation (3.2) by

separating the contributions of each link:

$$\begin{aligned} \mathbf{f}_i(s) &= \sum_{j=1}^3 \mathbf{f}_i^j(s), \\ \frac{\mathbf{f}_i^i(s)}{2\pi\mu} &= \left[\frac{-\mathbf{U}(s)}{\ln \kappa} + \lim_{\epsilon \rightarrow 0} \frac{(\mathbf{J}_i^i(s) - \mathbf{U}(s) \ln 2\epsilon)}{\ln^2 \kappa} \right] [\mathbf{t}_i \mathbf{t}_i - 2\mathbf{I}] - \frac{\mathbf{U}(s)}{2 \ln^2 \kappa} [3\mathbf{t}_i \mathbf{t}_i - 2\mathbf{I}], \\ \frac{\mathbf{f}_i^j(s)}{2\pi\mu} &= \frac{\mathbf{J}_i^j(s)}{\ln^2 \kappa} [\mathbf{t}_i \mathbf{t}_i - 2\mathbf{I}], \end{aligned}$$

where

$$\begin{aligned} \mathbf{J}_i^i(s) &= -\frac{1}{2} \left[\int_{s_{i-1}}^{s-2L\epsilon} + \int_{s+2L\epsilon}^{s_i} \right] \left[\frac{\mathbf{I}}{|\Delta|} + \frac{\Delta\Delta}{|\Delta|^3} \right] \times \left[\mathbf{I} - \frac{1}{2} \mathbf{t}_i \mathbf{t}_i \right] \cdot \mathbf{U}(\hat{s}) d\hat{s}, \\ \mathbf{J}_i^j(s) &= -\frac{1}{2} \left[\int_{s_{j-1}}^{s_j} \right] \left[\frac{\mathbf{I}}{|\Delta|} + \frac{\Delta\Delta}{|\Delta|^3} \right] \times \left[\mathbf{I} - \frac{1}{2} \mathbf{t}_j \mathbf{t}_j \right] \cdot \mathbf{U}(\hat{s}) d\hat{s}, \text{ for } i \neq j. \end{aligned}$$

The local velocity $\mathbf{U}(s)$ at a point on the i^{th} -link such that $s \in [s_{i-1} \ s_i]$ can be readily expressed in terms of the components of \mathbf{V}_i as

$$\mathbf{U}(s) = \begin{pmatrix} \dot{x}_i \\ \dot{y}_i \end{pmatrix} + (s - \sigma_i) \theta_i \mathbf{n}_i.$$

With this expression for the velocity at each point, the local force can be integrated over the length of each link to find the total force and torque applied on each link.

Principal hydrodynamic matrix \mathbf{A}_i^i

The coefficients for the matrix \mathbf{A}_i^i characterize the hydrodynamic drag on the i^{th} -link due to its own motion. As mentioned in section 3.2.2 all moments are taken about the center of the middle link. The value for all entries of the \mathbf{A}_i^i matrix can be found analytically and after integration they take the following form:

$$\mathbf{A}_i^i = \begin{pmatrix} a_i & b_i & 0 \\ b_i & c_i & 0 \\ a_i(y_2 - y_i) - c_i(x_2 - x_i) & c_i(y_2 - y_i) - b_i(x_2 - x_i) & d_i \end{pmatrix},$$

with

$$\begin{aligned}
a_i &= c_i^{\parallel} \cos^2 \theta_i + c_i^{\perp} \sin^2 \theta_i , \\
b_i &= c_i^{\parallel} \sin^2 \theta_i + c_i^{\perp} \cos^2 \theta_i , \\
c_i &= (c_i^{\parallel} - c_i^{\perp}) \sin \theta_i \cos \theta_i , \\
d_i &= c_i^{\odot}
\end{aligned}$$

and

$$c_i^{\parallel} = -\frac{4\pi L_i \mu}{\ln(\frac{2}{\kappa}) - \frac{3}{2}} , \quad c_i^{\perp} = -\frac{8\pi L_i \mu}{\ln(\frac{2}{\kappa}) - \frac{1}{2}} , \quad c_i^{\odot} = -\frac{8\pi L_i^3 \mu}{3(\ln(\frac{2}{\kappa}) + \frac{11}{6})} .$$

Hydrodynamic interaction matrix \mathbf{A}_i^j

We now turn to the hydrodynamic force due to the interaction between the different links. The matrix \mathbf{A}_i^j characterizes the hydrodynamic drag on the i^{th} -link due to the motion of the j^{th} -link. We first need to find expressions for $\mathbf{J}_i^j(s)$ as a function of \mathbf{V}_j , for $s \in [s_{i-1} \ s_i]$. We therefore substitute the velocity along the j^{th} -link using equation (A.1) and analytically evaluate all integrals

$$\mathbf{J}_i^j(s) = \begin{pmatrix} (J_i^j)_{11}(s) & (J_i^j)_{12}(s) & (J_i^j)_{13}(s) \\ (J_i^j)_{21}(s) & (J_i^j)_{22}(s) & (J_i^j)_{23}(s) \end{pmatrix} \mathbf{V}_j , \quad (\text{A.1})$$

where

$$\begin{aligned}
(J_i^j)_{11}(s) &= \frac{1}{2} \ln T_i^j(s) + \frac{\cos \theta_j P_i^j(s) - 2 \sin \theta_j Q_i^j(s)}{4\sqrt{P_i^j(s)^2 + Q_i^j(s)^2}} - \frac{\cos \theta_j R_i^j(s) - 2 \sin \theta_j S_i^j(s)}{4\sqrt{R_i^j(s)^2 + S_i^j(s)^2}} , \\
(J_i^j)_{12}(s) &= \frac{\sin \theta_j P_i^j(s) + 2 \cos \theta_j Q_i^j(s)}{4\sqrt{P_i^j(s)^2 + Q_i^j(s)^2}} - \frac{\sin \theta_j R_i^j(s) + 2 \cos \theta_j S_i^j(s)}{4\sqrt{R_i^j(s)^2 + S_i^j(s)^2}} , \\
(J_i^j)_{13}(s) &= \frac{1}{2} (y - s \sin \theta_i) \ln T_i^j(s) + \frac{Q_i^j(s)}{2\sqrt{P_i^j(s)^2 + Q_i^j(s)^2}} - \frac{S_i^j(s)}{2\sqrt{R_i^j(s)^2 + S_i^j(s)^2}} ,
\end{aligned}$$

$$\begin{aligned}
(J_i^j)_{21}(s) &= \frac{2 \sin \theta_j P_i^j(s) + \cos \theta_j Q_i^j(s)}{4\sqrt{P_i^j(s)^2 + Q_i^j(s)^2}} - \frac{2 \sin \theta_j R_i^j(s) + \cos \theta_j S_i^j(s)}{4\sqrt{R_i^j(s)^2 + S_i^j(s)^2}}, \\
(J_i^j)_{22}(s) &= \frac{1}{2} \ln T_i^j(s) - \frac{2 \cos \theta_j P_i^j(s) - \sin \theta_j Q_i^j(s)}{4\sqrt{P_i^j(s)^2 + Q_i^j(s)^2}} + \frac{2 \cos \theta_j R_i^j(s) - \sin \theta_j S_i^j(s)}{4\sqrt{R_i^j(s)^2 + S_i^j(s)^2}}, \\
(J_i^j)_{23}(s) &= \frac{1}{2} (s \cos \theta_i - x) \ln T_i^j(s) - \frac{P_i^j(s)}{2\sqrt{P_i^j(s)^2 + Q_i^j(s)^2}} - \frac{R_i^j(s)}{2\sqrt{R_i^j(s)^2 + S_i^j(s)^2}}.
\end{aligned}$$

We used the following notation simplifications:

$$\begin{aligned}
x &= x_j - x_i, \\
y &= y_j - y_i, \\
P_i^j(s) &= s \cos \theta_i - \cos \theta_j - x, \\
Q_i^j(s) &= s \sin \theta_i - \sin \theta_j - y, \\
R_i^j(s) &= s \cos \theta_i + \cos \theta_j - x, \\
S_i^j(s) &= s \sin \theta_i + \sin \theta_j - y, \\
T_i^j(s) &= \frac{\cos \theta_j P_i^j(s) + \sin \theta_j Q_i^j(s)}{\cos \theta_j R_i^j(s) + \sin \theta_j S_i^j(s)}.
\end{aligned}$$

The local hydrodynamic force at the arc-length $s \in [s_{i-1} \ s_i]$ due to the motion of the j^{th} -link can be deduced directly from equation (A.1) as:

$$\mathbf{f}_i^j(s) = \begin{pmatrix} (f_i^j)_{11}(s) & (f_i^j)_{12}(s) & (f_i^j)_{13}(s) \\ (f_i^j)_{21}(s) & (f_i^j)_{22}(s) & (f_i^j)_{23}(s) \end{pmatrix} \mathbf{V}_j = \frac{2\pi\mu\mathbf{J}_i^j(s)}{\ln^2 \kappa} \cdot [\mathbf{t}_i \mathbf{t}_i - 2 \mathbf{I}],$$

All coefficients of the matrix \mathbf{A}_i^j are obtained by numerical integration of these relations between $s = s_{i-1}$ and $s = s_i$ to match the total hydrodynamic force and moment (about the center of the middle link) on the i^{th} -link due to the motion of the j^{th} -link. In this study we use a ten-point gaussian quadrature rule for the numerical integration.

A.2 Expression for the artificial lubrication

We now describe the artificial lubrication term mentioned in section 3.4.2, which is used in the three-link model, to regularize the slenderbody theory formulation by R.G. Cox [41]. The short range lubrication interaction between two bodies have been investigated by Claeys & Brady [34]. In general, the lubrication term is simply added to the far field hydrodynamic interaction term and only dominates the interaction when the minimum distance between the two bodies is close to one diameter of the fiber. This approach is commonly used in suspension simulations [24, 35].

Consider two identical and parallel slender cylindrical fibers approaching one another at a velocity U in the direction normal to their centerline. The forces F acting on each fiber are equal and opposite in sign and can be computed using the lubrication approximation

$$F \approx -\frac{3\pi\sqrt{2}\mu}{8} \left(\frac{r}{\delta}\right)^{3/2} L U , \quad (\text{A.2})$$

where L is the length of each fiber, r its radius and δ is the gap distance between the two. In this analysis, we artificially account for lubrication by assuming that the i^{th} and $i + 1^{\text{th}}$ links both have a length of L_2 and approach one another with parallel centerlines at a velocity of $L_2(\dot{\theta}_{i+1} - \dot{\theta}_i)/2$. We assume the gap to have a size of $L_2|\theta_{i+1} - \theta_i|$. We then use the simple expression for the lubrication force given by equation A.2 to find the lubrication force acting on each link.

The lubrication force acting on each of the two neighboring links are equal and opposite and hence does not affect the equilibrium equation of the total swimmer. The lubrication term is only required in the computation of the viscous dissipation and will increase it significantly when two neighboring links are getting too close.

Appendix B

Numerical discretization of flagellated swimmers

Here we give expressions for all matrices, which appear in the numerical representation of the dynamics of flagellated swimmers. All notations used in this appendix have been previously introduced in section 4.2.1 and 4.2.4.

For each element $i = 1, \dots, N$ the expression for the matrices in equation 4.37 are obtained by numerical integration of the equations of motion (4.26,4.27,4.28). The distribution of hydrodynamic force per unit length $\mathbf{f}(s)$ is assumed to be piecewise constant over each element and the integrals are evaluated by applying the midpoint rule. The matrices in equation 4.37 yield the following expressions:

$$\begin{aligned}\mathcal{A}_i &= \begin{pmatrix} 1 & 0 & -(y_i - y_0) \\ 0 & 1 & (x_i - x_0) \end{pmatrix}, \\ \mathcal{L}_i &= \frac{1}{8\pi\mu} \left(\ln(\kappa^2 \exp(1)) [\mathbf{I} + 2\mathbf{t}_i\mathbf{t}_i] - 2[\mathbf{I} - \mathbf{t}_i\mathbf{t}_i] \right), \\ \mathcal{M}_{ij} &= \frac{1}{8\pi\mu} \left(\frac{\mathbf{I}}{|\mathbf{R}_i - \mathbf{R}_j|} + \frac{(\mathbf{R}_i - \mathbf{R}_j)(\mathbf{R}_i - \mathbf{R}_j)}{|\mathbf{R}_i - \mathbf{R}_j|^3} \right) \quad \text{for } i \neq j, \\ \mathcal{M}_{ii} &= \mathbf{0}, \\ \mathcal{N}_{ij} &= \frac{1}{8\pi\mu} \left(\frac{\mathbf{I} + \mathbf{t}_i\mathbf{t}_i}{|s_i - s_j|} \right) \quad \text{for } i \neq j, \\ \mathcal{N}_{ii} &= \mathbf{0}.\end{aligned}$$

Note that, eventhough both matrices \mathcal{M}_{ii} and \mathcal{N}_{ii} are individually singular, the difference between the two $\mathcal{M}_{ii} - \mathcal{N}_{ii}$ vanishes (see equation 4.26) and we can thus freely set both \mathcal{M}_{ii} and \mathcal{N}_{ii} to be equal to zero.

The evaluation of \mathcal{V}_{i0} and \mathcal{W}_{i0} involves the evaluation of integrals over the constant distribution of singularities located between the two foci of the prolate spheroidal head. A change of variables rescales the integral between the two foci to an integral for ξ between $\xi = -1$ and $\xi = 1$. The numerical integration is done by means of an N_q -point gaussian quadrature rule. The q quadrature points are called ξ_q with associated weights w_q . In our computations, the number of quadrature points used to estimate these integrals is $N_q = 10$. With these additional notations, the expressions for \mathcal{V}_{0i} and \mathcal{W}_{0i} , which characterize the ambient flow around the flagellum due to the motion of the head, take the following form:

$$\begin{aligned}\mathcal{V}_{i0} &= -\frac{1}{16\pi\mu} \sum_{q=1}^{N_q} w_q \left[\frac{\mathbf{I}}{|\mathbf{R}_{i0_q}|} + \frac{\mathbf{R}_{i0_q}\mathbf{R}_{i0_q}}{|\mathbf{R}_{i0_q}|^3} + \frac{L_0^2 e^2 (1 - \xi_q^2)}{2} \left(\frac{\mathbf{I}}{|\mathbf{R}_{i0_q}|^3} - \frac{3\mathbf{R}_{i0_q}\mathbf{R}_{i0_q}}{|\mathbf{R}_{i0_q}|^5} \right) \right], \\ \mathcal{W}_{i0} &= -\frac{3}{32\pi\mu} \sum_{q=1}^{N_q} w_q \left[3 \frac{(1 - e^2)}{(1 + e^2)} \left(\frac{L_0^2 e^2 (1 - \xi_q^2)^2 (\mathbf{R}_{i0_q} \cdot \mathbf{t}_0) \mathbf{n}_0 + (\mathbf{R}_{i0_q} \cdot \mathbf{n}_0) \mathbf{t}_0}{4 |\mathbf{R}_{i0_q}|^5} \right. \right. \\ &\quad \left. \left. + (1 - \xi_q^2) (\mathbf{R}_{i0_q} \cdot \mathbf{t}_0) (\mathbf{R}_{i0_q} \cdot \mathbf{n}_0) \left(1 - \frac{5L_0^2 e^2 (1 - \xi_q^2)}{4 |\mathbf{R}_{i0_q}|^2} \right) \frac{\mathbf{R}_{i0_q}}{|\mathbf{R}_{i0_q}|^5} \right) + \hat{\mathbf{z}} \times \frac{\mathbf{R}_{i0_q}}{|\mathbf{R}_{i0_q}|^3} \right],\end{aligned}$$

where $\mathbf{R}_{i0_q} = \mathbf{R}_i - (\mathbf{R}_0 + c\xi_q \mathbf{t}_0)$.

The expressions for all matrices appearing in equations (4.38) and (4.39) can be written:

$$\begin{aligned}\mathcal{L}_0 &= \frac{1}{c_0^{\parallel}} \mathbf{t}_0 \mathbf{t}_0 + \frac{1}{c_0^{\perp}} \mathbf{n}_0 \mathbf{n}_0, \\ \mathcal{M}_{0j} &= \frac{1}{8\pi\mu} \left(\frac{\mathbf{I}}{|\mathbf{R}_{0j}|} + \frac{\mathbf{R}_{0j}\mathbf{R}_{0j}}{|\mathbf{R}_{0j}|^3} \right) + \frac{L_0^2 (1 - e^2)}{48\pi\mu} \left[\left(\frac{-1}{|\mathbf{R}_{0j}|^3} + \frac{3(\mathbf{R}_{0j} \cdot \mathbf{t}_0)^2}{|\mathbf{R}_{0j}|^5} \right) \mathbf{I} \right. \\ &\quad \left. - \frac{6\mathbf{R}_{0j} \cdot \mathbf{t}_0}{|\mathbf{R}_{0j}|^5} (\mathbf{t}_0 \mathbf{R}_{0j} + \mathbf{R}_{0j} \mathbf{t}_0) + \frac{2\mathbf{t}_0 \mathbf{t}_0}{|\mathbf{R}_{0j}|^3} + \left(\frac{-3}{|\mathbf{R}_{0j}|^5} + \frac{15(\mathbf{R}_{0j} \cdot \mathbf{t}_0)^2}{|\mathbf{R}_{0j}|^7} \right) \mathbf{R}_{0j} \mathbf{R}_{0j} \right],\end{aligned}$$

$$\vartheta_0 = \frac{1}{c_0^\odot},$$

$$\eta_{0j} = \frac{1}{8\pi(2-e^2)\mu} \left[(1+e^2) \frac{\hat{\mathbf{z}} \times \mathbf{R}_{0j}}{|\mathbf{R}_{0j}|^3} + 3(1-e^2)(\mathbf{R}_{0j} \cdot \mathbf{t}_0)(\mathbf{R}_{0j} \cdot \mathbf{n}_0) \frac{\mathbf{R}_{0j}}{|\mathbf{R}_{0j}|^5} \right],$$

where $\mathbf{R}_{0j} = \mathbf{R}_0 - \mathbf{R}_j$.

Appendix C

Analytical solution for temperature and velocity

C.1 Derivation of the solution

The boundary condition 6.20 takes the following form:

$$-\frac{\partial}{\partial r}T(r, \theta)\Big|_{r=1} = \text{Bi } T(1, \theta). \quad (\text{C.1})$$

The *a priori* expression for the temperature 6.23 is differentiated with respect to r

$$\frac{\partial}{\partial r}T(r, \theta)\Big|_{r=1} = -\frac{1 - \cos \theta}{(2 - 2 \cos \theta)^{\frac{3}{2}}} + \sum_{n=0}^{\infty} n c_n P_n(\cos \theta). \quad (\text{C.2})$$

This expression C.2 is introduced in the boundary condition C.1 and yields the following development:

$$\sum_{n=0}^{\infty} (n + \text{Bi}) c_n P_n(\cos \theta) = \frac{1 - 2\text{Bi}}{2(2 - 2 \cos \theta)^{\frac{1}{2}}}. \quad (\text{C.3})$$

Using the identity

$$\frac{1}{(r^2 + 1 - 2r \cos \theta)^{\frac{1}{2}}} = \sum_{n=0}^{\infty} r^n P_n(\cos \theta) \quad (\text{C.4})$$

at $r = 1$ and the unicity of the development in Legendre series, the coefficients c_n can be determined

$$c_n = \frac{1 - \text{Bi}}{2(n + \text{Bi})} . \quad (\text{C.5})$$

Introducing the development of the streamfunction in Gegenbauer polynomials (6.28) in equation (6.25) and using the identities from appendix C.2 yields the following series expansion for the radial velocity:

$$u_r = \sum_{n=2}^{n=\infty} (R_n r^{n-2} + S_n r^{-(n+1)} + T_n r^n + U_n r^{-(n-1)}) P_{n-1}(\cos \theta). \quad (\text{C.6})$$

Since u_r has to be bounded at $r = 0$, the coefficients S_n and U_n must vanish. Also, the radial velocity has to vanish at the interface $r = 1$ for the droplet to remain spherical, thus $T_n = -R_n$. Hence the expansion (6.28) of the streamfunction can be rewritten in a simpler form

$$\psi(r, \theta) = \sum_{n=2}^{\infty} R_n (r^n - r^{n+2}) C_n^{-1/2}(\cos \theta) . \quad (\text{C.7})$$

The expression for the temperature field 6.23 and for the stream function C.7 are introduced in the tangential stress boundary condition 6.22

$$\sum_{n=2}^{\infty} 2(1-2n)R_n \frac{C_n^{-1/2}(\cos \theta)}{\sin \theta} = \frac{\sin \theta}{(2 - 2 \cos \theta)^{\frac{3}{2}}} + \sum_{n=2}^{\infty} n(n-1)c_{n-1} \frac{C_n^{-1/2}(\cos \theta)}{\sin \theta} . \quad (\text{C.8})$$

Using the identity

$$\frac{\sin \theta}{(2 - 2 \cos \theta)^{\frac{3}{2}}} = \sum_{n=2}^{\infty} n(n-1) \frac{C_n^{-1/2}(\cos \theta)}{\sin \theta} \quad (\text{C.9})$$

the tangential stress boundary condition yields the equation

$$\sum_{n=2}^{\infty} 2R_n(2n-1) C_n^{-1/2}(\cos \theta) = - \sum_{n=2}^{\infty} (1 + c_{n-1})(n-1)n C_n^{-1/2}(\cos \theta) . \quad (\text{C.10})$$

Thus, $R_n = -\frac{n(n-1)}{2(2n-1)}(1 + c_{n-1})$, $\forall n \geq 2$. Rearranging the different terms, in order to

isolate the singularity at \mathbf{r}_0 yields the final expression for the stream velocity (6.31).

C.2 Properties of Gegenbauer polynomials

$$\begin{aligned}\frac{d C_n^{-1/2}(\cos \theta)}{d \theta} &= \sin \theta P_{n-1}(\cos \theta) , \\ \frac{d P_{n-1}(\cos \theta)}{d \theta} &= -\frac{n(n-1)C_n^{-1/2}(\cos \theta)}{\sin \theta} .\end{aligned}$$

Bibliography

- [1] A. Acrivos and G.K. Youngren. Stokes flow past a particle of arbitrary shape: a numerical method of solution. *J. Fluid Mech.*, 69:377–403, 1975.
- [2] B. Alberts, D. Bray, J. Lewis, M. Raff, K. Roberts, and J.D. Watson. *Molecular Biol. Cell, 3rd edition*. Garland Publishing, Inc., New York, 1994.
- [3] M.J. Anderson, J. Nyholt, and A.F. Dixson. Sperm competition and the evolution of sperm midpiece volume in mammals. *J. Zool.*, 267:135–142, 2005.
- [4] J. Atencia and D.J. Beebe. Magnetically-driven biomimetic micro pumping using vortices. *Lab Chip*, 4 (6):598–602, 2004.
- [5] J.E. Avron, O. Gat, and O. Kenneth. Optimal swimming at low reynolds numbers. *Phys. Rev. Lett.*, 93 (18):Art. No. 186001, 2004.
- [6] J.E. Avron, O. Kenneth, and D.H. Oaknin. Pushmepullyou: an efficient micro-swimmer. *New J. Phys.*, 7:234, 2005.
- [7] C.D. Bain, G.D. Burnett-Hall, and R.R. Montgomerie. Rapid motion of liquid drops. *Nature*, 372:414, 1994.
- [8] G.K. Batchelor. Slender-body theory for particles of arbitrary cross-section in stokes flow. *J. Fluid Mech.*, 44 (3):419–440, 1970.
- [9] G.K. Batchelor. The stress system in a suspension of force-free particles. *J. Fluid Mech.*, 41 (3):545–570, 1970.
- [10] L.E. Becker, S.A. Koehler, and H.A. Stone. On self-propulsion of micro-machines at low reynolds number: Purcell’s three-link swimmer. *J. Fluid Mech.*, 490:15–35, 2003.
- [11] H.C. Berg. Motile behavior of bacteria. *Phys. Today*, 53(1):24–29, 2000.
- [12] H.C. Berg. How spiroplasma might swim. *J. Bacteriol.*, 184 (8):637–640, 2002.
- [13] D. Bertsekas. *Dynamic Programming and Optimal Control, 3rd Edition*. Athena Scientific, Belmont, MA, 2005.
- [14] A.L. Biance, C. Clanet, and D. Quéré. Leidenfrost drops. *Phys. Fluids*, 15(6):1632, 2003.

- [15] J. Bico, C. Marzolin, and D. Quéré. Pearl drops. *Europhys. Lett.*, 47:220 – 226, 1999.
- [16] J.R. Blake. Microbiological fluid mechanics: a tribute to sir james lighthill. *Math. Meth. Appl. Sci.*, 24 (17-18):1469–1483, 2001.
- [17] C. Brennen and H. Winet. Fluid mechanics of propulsion by cilia and flagella. *Annu. Rev. Fluid Mech.*, 9:339–398, 1977.
- [18] J.V. Briskie and R. Montgomerie. Sperm size and sperm competition in birds. *Proc. R. Soc. London, Ser. B*, 247 (1319):89–95, 1992.
- [19] C.J. Brokaw. Computer simulation of movement-generating cross-bridges. *Biophys. J.*, 16:1013–1027, 1976.
- [20] C.J. Brokaw. Automated methods for estimation of sperm flagellar bending parameters. *Cell Motil.*, 4:417–430, 1984.
- [21] C.J. Brokaw. Computerized analysis of flagellar motility by digitization and fitting of film images with straight segments of equal length. *Cell Motil. Cytoskeleton*, 17:309–316, 1990.
- [22] C.J. Brokaw. Simulating the effects of fluid viscosity on the behaviour of sperm flagella. *Math. Meth. Appl. Sci.*, 24:1351–1365, 2001.
- [23] C.J. Brokaw. Computer simulation of flagellar movement viii: Coordination of dynein by local curvature control can generate helical bending waves. *Cell Motil. Cytoskeleton*, 53:103124, 2002.
- [24] J.E. Butler and E.S. Shaqfeh. Dynamic simulations of the inhomogeneous sedimentation of rigid fibres. *J. Fluid Mech.*, 468:205–237, 2002.
- [25] M. Callies and D. Quéré. On water repellency. *Soft Matter*, 1:55–61, 2005.
- [26] S. Camalet, F. Julicher, and J. Prost. Self-organized beating and swimming of internally driven filaments. *Phys. Rev. Lett.*, 82 (7):1590–1593, 1999.
- [27] R.A. Cardullo and J.M. Baltz. Metabolic regulation in mammalian sperm: mitochondrial volume determines sperm length and flagellar beat frequency. *Cell Motil. Cytoskeleton*, 19:180–188, 1991.
- [28] B. Chan, N.J. Balmforth, and A.E. Hosoi. Building a better snail: Lubrication and gastropod locomotion. *Phys. Fluids*, 17(11):113101, 2005.
- [29] S. Chandrasekhar. *Hydrodynamic and hydromagnetic stability*. Clarendon press, Oxford, 1961.
- [30] S.T. Chang and O.D. Velev. Evaporation-induced particle microseparations inside droplets floating on a chip. *Langmuir*, 22:1459 – 1468, 2006.

- [31] S. Childress. *Mechanics of swimming and flying*. Cambridge University Press, Cambridge, 1981.
- [32] K.K. Christensen-Dalsgaard and T. Fenchel. Increased filtration efficiency of attached compared to free-swimming flagellates. *Aquat. Microb. Ecol.*, 33:77–86, 2003.
- [33] A.T. Ciofalo and T.Y. Wu. Hydromechanics of low-reynolds-number flow. part 2. singularity method for stokes flows. *J. Fluid Mech.*, 67 (4):787–815, 1975.
- [34] I.L. Claeys and J.F. Brady. Lubrication singularities of the grand resistance tensor for two arbitrary particles. *Physicochem. Hydrodyn.*, 11(3):261–293, 1989.
- [35] I.L. Claeys and J.F. Brady. Suspensions of prolate spheroids in stokes flow. part 1. dynamics of a finite number of particles in an unbounded fluid. *J. Fluid Mech.*, 251:411–442, 1993.
- [36] K.W. Cleland and L. Rothschild. The bandicoot spermatozoon: An electron microscope study of the tail. *Proc. R. Soc. London, Ser. B*, 150 (938):24–42, 1959.
- [37] R. Cortez. The method of regularized stokeslets. *Siam J. Sci. Comp.*, 23 (4):1204–1224, 2001.
- [38] R. Cortez, L. Fauci, N. Cowen, and R. Dillon. Simulation of swimming organisms: Coupling internal mechanics with external fluid dynamics. *Comput. Sci. Eng.*, 6 (3):38–45, 2004.
- [39] R. Cortez, L. Fauci, and A. Medovikovc. The method of regularized stokeslets in three dimensions: Analysis, validation, and application to helical swimming. *Phys. Fluids*, 17:031504, 2005.
- [40] J. Cosson. A moving image of flagella: News and views on the mechanisms involved in axonemal beating. *Cell Biol. Int.*, 20 (2):83–94, 1996.
- [41] R.G. Cox. The motion of slender bodies in a viscous fluid. part 1. general theory. *J. Fluid Mech.*, 44 (4):791–810, 1970.
- [42] R.G. Cox. The motion of slender bodies in a viscous fluid. part 2. shear flow. *J. Fluid Mech.*, 45:625–657, 1971.
- [43] J.M. Cummins and P.F. Woodall. On mammalian sperm dimensions. *J. Reprod. Fert.*, 75:153–175, 1985.
- [44] A. Czirók and T. Vicsek. Collective behavior of interacting self-propelled particles. *Phys. A*, 281:17–29, 2000.
- [45] S. Daniel, M.K. Chaudhury, and J.C. Chen. Fast drop movements resulting from the phase change on a gradient surface. *Science*, 291(5504):633 – 636, 2001.

- [46] A.A. Darhuber, J.Z. Chen, J.M. Davis, and S.M. Troian. A study of mixing in thermocapillary flows on micropatterned surfaces. *Phil. Trans. R. Soc. Lond. A*, 362:1037 – 1058, 2004.
- [47] N. Darnton, L. Turner, K. Breuer, and H. Berg. Moving fluid with bacterial carpets. *Biophys. J.*, 86:1863–1870, 2004.
- [48] S.H. Davis. Thermocapillary instabilities. *Ann. Rev. Fluid Mech.*, 19:403, 1987.
- [49] R.D. Deegan, O. Bakajin, T.F. Dupont, G. Huber, S.R. Nagel, and T.A. Witten. Capillary flow as the cause of ring stains from dried liquid drops. *Nature*, 389:827 – 829, 1997.
- [50] J. den Toonder, F. Bos, D. Broer, L. Filippini, M. Gillies, M. de Goede, T. Mol, M. Reijme, W. Talen, H. Wilderbeek, V. Khatavkarb, and P. Anderson. Artificial cilia for active micro-fluidic mixing. *Lab Chip*, 8(4):533–541, 2008.
- [51] R.D. Dresdner, D.F. Katz, and S.A. Berger. The propulsion by large amplitude waves of unflagellar micro-organisms of finite length. *J. Fluid Mech.*, 97(3):591–621, 1980.
- [52] R. Dreyfus, J. Baudry, M. Roper, M. Fermigier, H. Stone, and J. Bibette. Microscopic artificial swimmers. *Nature*, 437(6):862–865, 2005.
- [53] S.K. Dutcher. Flagellar assembly in two hundred and fifty easy-to-follow steps. *Trends Genet.*, 11(10):398–404, 1995.
- [54] R.A. Erb and Thelen. Promoting permanent dropwise condensation. *Ind. Eng. Chem.*, 57(10):49 – 52, 1965.
- [55] L.J. Fauci and R. Dillon. Biofluidmechanics of reproduction. *Annu. Rev. Fluid Mech.*, 38:371–394, 2006.
- [56] H.C. Fu, T.R. Powers, and C.W. Wolgemuth. Theory of swimming filaments in viscoelastic media. *Phys. Rev. Lett.*, 99(25):258101, 2007.
- [57] M.J.G. Gage. Mammalian sperm morphometry. *Proc. R. Soc. London, Ser. B*, 265(1391):97–103, 1998.
- [58] M.J.G. Gage and R.P. Freckleton. Relative testis size and sperm morphometry across mammals: no evidence for an association between sperm competition and sperm length. *Proc. R. Soc. London, Ser. B*, 270:625–632, 2003.
- [59] M.J.G. Gage, C. Macfarlane, S. Yeates, R. Shackleton, and G.A. Parker. Relationships between sperm morphometry and sperm motility in the atlantic salmon. *J. Fish Biol.*, 61:1528–1539, 2002.
- [60] L. Gao and T.J. McCarthy. A perfectly hydrophobic surface. *J. Am. Chem. Soc.*, 128:9052–9053, 2006.

- [61] T. Götz. *Interactions of Fibers and Flow: Asymptotics, Theory and Numerics*. PhD thesis, Universität Kaiserslautern, 2000.
- [62] T. Götz. On collocation schemes for integral equations arising in slender-body approximations of flow past particles with circular cross-section. *J. Eng. Math.*, 42:203–221, 2002.
- [63] S. Gourinath, D.M. Himmel, J.H. Brown, L. Reshetnikova, Szent-Gyorgyi A.G., and C. Cohen. Crystal structure of scallop myosin s1 in the pre-power stroke state to 2.6 a resolution: flexibility and function in the head. *Structure*, 11:1621–1627, 2003.
- [64] J. Gray. The movement of sea-urchin spermatozoa. *J. Exp. Biol.*, 32:775–801, 1955.
- [65] J. Gray and G.J. Hancock. The propulsion of sea-urchin spermatozoa. *J. Exp. Biol.*, 32:802–814, 1955.
- [66] B. Guirao and J.-F. Joanny. Spontaneous creation of macroscopic flow and metachronal waves in an array of cilia. *Biophys. J.*, 92:1900–1917, 2007.
- [67] M. Gunji and M. Washizu. Self-propulsion of a water droplet in an electric field. *J. Phys. D: Appl. Phys.*, 38:2417–2423, 2005.
- [68] D. Halliday, R. Resnick, and J. Walker. *Fundamentals of physics, seventh edition*. Wiley, New York, 2005.
- [69] G.J. Hancock. The self-propulsion of microscopic organism through liquids. *Proc. R. Soc. London, Ser. A*, 217:96–121, 1953.
- [70] J. Happel and H. Brenner. *Low Reynolds number hydrodynamics*. Noordhoff int. publ., Leyden, 1973.
- [71] B. He, N. Patankar, and J.J. Lee. Multiple equilibrium droplet shapes and design criterion for rough hydrophobic surfaces. *Langmuir*, 19:4999–5003, 2003.
- [72] J.P. Hernandez-Ortiz, C.G. Stoltz, and M.D. Graham. Transport and collective dynamics in suspensions of confined swimming particles. *Phys. Rev. Lett.*, 95:204501, 2005.
- [73] J.J.L. Higdon. The generation of feeding currents by flagellar motions. *J. Fluid Mech.*, 94 (2):305–330, 1979.
- [74] J.J.L. Higdon. A hydrodynamic analysis of flagellar propulsion. *J. Fluid Mech.*, 90 (4):685–711, 1979.
- [75] M.E. Holwill and J.L. McGregor. Micromanipulation of the flagellum of crithidia oncopelti. *J. Exp. Biol.*, 60:437–444, 1974.

- [76] H. Hu and R.G. Larson. Analysis of the effects of marangoni stresses on the microflow in an evaporating sessile droplet. *Langmuir*, 21:3972 – 3980, 2005.
- [77] K. Inaba. Molecular architecture of the sperm flagella: Molecules for motility and signaling. *Zool. Sci.*, 20 (9):1043–1056, 2003.
- [78] F.P. Incropera and D.P. deWitt. *Fundamentals of heat and mass transfer, fifth edition*. Wiley, New York, 2002.
- [79] K. Ishiyama, M. Sendoh, and K.I. Arai. Magnetic micromachines for medical applications. *J. Magn. Magnetic Mater.*, 242:41–46, 2002.
- [80] K. Ishiyama, M. Sendoh, A. Yamazaki, and M. Inoue. Swimming of magnetic micro-machines under a very wide-range of reynolds number conditions. *IEEE Trans. Magn.*, 37 (4):2868–2870, 2001.
- [81] W. Jia and H. Qiu. Fringe probing of an evaporating microdroplet on a hot surface. *Int. J. Heat and Mass Trans.*, 45:4141–4150, 2002.
- [82] K. John, M. Bär, and U. Thiele. Self-propelled running droplets on solid substrates driven by chemical reactions. *Eur. Phys. J. E*, 18:183–199, 2005.
- [83] R.E. Johnson. An improved slender-body theory for stokes flow. *J. Fluid Mech.*, 99 (2):411–431, 1980.
- [84] R.E. Johnson and C.J. Brokaw. Flagellar hydrodynamics: A comparison between resistive-force theory and slender-body theory. *Biophys. J.*, 25:113–127, 1979.
- [85] D.N. Johnston, N.R. Silvester, and M.E. Holwill. An analysis of the shape and propagation of waves on the flagellum of crithidia oncopelti. *J. Exp. Biol.*, 80:299–315, 1979.
- [86] S.G. Kandlikar. A theoretical model to predict pool boiling chf incorporating effects of contact angle and orientation. *ASME Journal of Heat Transfer*, 123:1071–1079, 2001.
- [87] M. Kawamura. Efficiency of swimming of micro-organism and singularity in shape space. *Mod. Phys. Lett. A*, 11 (24):1961–1969, 1996.
- [88] M. Kawamura and A. Sugamoto. Swimming of micro-organisms viewed from string and membrane theories. *Mod. Phys. Lett. A*, 9 (13):1159–1174, 1994.
- [89] J.B. Keller and S.I. Rubinow. Slender-body theory for slow viscous flow. *J. Fluid Mech.*, 75 (4):705–714, 1976.
- [90] V. Khatavkar, P. Anderson, J. den Toonder, and Meijer H. Active micromixer based on artificial cilia. *Phys. Fluids*, 19(8):083605, 2007.

- [91] S. Kim and S.J. Karrila. *Microhydrodynamics: Principles and Selected Applications*. Butterworth-Heinemann, Boston, 1991.
- [92] M. Kinukawa, J. Ohmuro, S.A. Baba, S. Murashige, M. Okuno, M. Nagata, and F. Aoki. Analysis of flagellar bending in hamster spermatozoa: Characterization of an effective stroke. *Biol. Reprod.*, 73:1269–1274, 2005.
- [93] T.N. Krupenkin, J.A. Taylor, T.M. Schneider, and S. Yang. From rolling ball to complete wetting: The dynamic tuning of liquids on nanostructured surfaces. *Langmuir*, 20:3824–3827, 2004.
- [94] K. Kruse, S. Camalet, and F. Julicher. Self-propagating patterns in active filament bundles. *Phys. Rev. Lett.*, 87 (13):138101, 2001.
- [95] A. Lafuma and D. Quéré. Superhydrophobic states. *Nat. Mater.*, 2(7):457–460, 2003.
- [96] C.W. LaMunyon and S. Ward. Evolution of sperm size in nematodes: sperm competition favours larger sperm. *Proc. R. Soc. London, Ser. B*, 266:263–267, 1999.
- [97] K.K.S. Lau, J. Bico, K.B.K. Teo, M. Chhowalla, G.A.J. Amaratunga, W.I. Milne, G.H. McKinley, and K.K. Gleason. Superhydrophobic carbon nanotube forests. *Nano Lett.*, 3 (12):1701–1705, 2003.
- [98] E. Lauga. Floppy swimming: Viscous locomotion of actuated elastica. *Phys. Rev. E*, 75:041916, 2007.
- [99] J. Lighthill. *Mathematical Biofluidynamics*. SIAM. Society For Industrial and Applied Mathematics, Philadelphia, 1975.
- [100] J. Lighthill. Flagellar hydrodynamics: the john von neumann lecture, 1975. *Siam Rev.*, 18 (2):161–230, 1976.
- [101] J. Lighthill. Helical distributions of stokeslets. *J. Eng. Math.*, 30 (1-2):35–78, 1996.
- [102] J. Lighthill. Reinterpreting the basic theorem of flagellar hydrodynamics. *J. Eng. Math.*, 30 (1-2):25–34, 1996.
- [103] C.B. Lindermann. Testing the geometric clutch hypothesis. *Biol. Cell*, 96:681–690, 2004.
- [104] C.P. Lowe. A hybrid particle/continuum model for micro-organism motility. *Future Generat. Comput. Syst.*, 17:853–862, 2001.
- [105] V. Magar, T. Goto, and T.J. Pedley. Nutrient uptake by a self-propelled steady squirmer. *Q. Jl Mech. Appl. Math.*, 56 (1):65–91, 2003.

- [106] L. Mahadevan and Y. Pomeau. Rolling droplets. *Phys. Fluids*, 11(9):2449–2453, 1999.
- [107] K. Makino, I. Michiyoshi, K. Sakamoto, and K. Hojo. The behaviour of a water droplet on heated surfaces. *Int. J. Heat. Mass Transfer*, 27 (5):781–791, 1984.
- [108] A.F. Malo, M. Gomendio, J. Garde, B. Lang-Lenton, A.J. Soler, and E.R.S. Roldan. Sperm design and sperm function. *Biol. Lett.*, 2:246249, 2006.
- [109] C. Marangoni. On the expansion of a drop of liquid floating on the surface of another liquid. Tipographia dei fratelli Fusi, Pavia, 1865.
- [110] Marcos and R. Stocker. Microorganisms in vortices: a microfluidic setup. *Limnol. Oceanogr. : Methods*, 4:392–398, 2006.
- [111] G. McHale, S. Aqil, N.J. Shirtcliffe, M.I. Newton, and H.Y. Erbil. Analysis of droplet evaporation on a superhydrophobic surface. *Langmuir*, 21(24):11053–11090, 2005.
- [112] A. Najafi and R. Golestanian. Simple swimmer at low reynolds number: Three linked spheres. *Phys. Rev. E*, 69 (6):Art. No. 062901 Part 1, 2004.
- [113] E.M. Neuhaus, A. Mashukova, J. Barbour, D. Wolters, and H. Hatt. Novel function of β -arrestin2 in the nucleus of mature spermatozoa. *J. Cell Sci.*, 119(15):3047–3056, 2006.
- [114] K. Nishimura, M. Sendoh, K. Ishiyama, K.I. Arai, H. Uchida, and M. Inoue. Fabrication and swimming properties of micro-machine coated with magnetite prepared by ferrite plating. *Phys. Status Solidi B*, 241 (7):1686–1688, 2004.
- [115] T. Onda, S. Shibuichi, N. Satoh, and K. Tsujii. Super-water-repellent fractal surfaces. *Langmuir*, 12:2125, 1996.
- [116] A. Otten and S. Herminghaus. How plants keep dry: A physicists point of view. *Langmuir*, 20:2405–2408, 2004.
- [117] C.S. Peskin. The immersed boundary method. *Acta Numer.*, 11:479–517, 2002.
- [118] O. Pironneau and D.F. Katz. Optimal swimming of flagellated micro-organisms. *J. Fluid Mech.*, 66 (2):391–415, 1974.
- [119] S. Plon and Bernard R.T.F. A review of spermatozoan morphology in cetacea with new data for the genus kogia. *J. Zool.*, 269:466–473, 2006.
- [120] W.H. Press, S.A. Teukolsky, W.T. Vetterling, and B.P. Flannery. *Numerical recipes in C, Second Edition*. Cambridge University Press, Cambridge, 1992.
- [121] E.M. Purcell. Life at low reynolds number. *Amer. J. Phys.*, 45 (1):3–11, 1977.

- [122] E.M. Purcell. The efficiency of propulsion by a rotating flagellum. *Proc. Nat. Acad. Sci. U.S.A.*, 94 (21):11307–11311, 1997.
- [123] Y.M. Qiao and S. Chandra. Experiments on adding surfactant to water drops boiling on a hot surface. *Proc. R. Soc. London, Ser. A*, 453:673–689, 1997.
- [124] D. Quéré. Fakir droplets (news & views). *Nat. Mater.*, 1:14–15, 2002.
- [125] D Quéré. Rough ideas on wetting. *Phys. A*, 313:32–46, 2003.
- [126] O. Raz and J.E. Avron. Comment on “optimal stroke patterns for purcells three-link swimmer”. *Phys. Rev. Lett.*, 100:029801, 2008.
- [127] M. Reyssat, Y. Chen, F. Marty, A. Pepin, and D. Quéré. Microfabricated textured surfaces for super-hydrophobicity investigations. *Microelectron. Eng.*, 78-79:100–105, 2005.
- [128] M. Reyssat, A. Pepin, F. Marty, Y. Chen, and D. Quéré. Bouncing transitions on microtextured materials. *Europhys. Lett.*, 74 (2):306–312, 2006.
- [129] D. Richard, C. Clanet, and D. Quéré. Contact time of a bouncing drop. *Nature*, 417:811, 2002.
- [130] R. Robinson. Ciliate genome sequence reveals unique features of a model eukaryote. *PLoS Biol.*, 4(9):1473, 2006.
- [131] U. Rüffer and W. Nultsch. High-speed cinematographic analysis of the movement of chlamydomonas. *Cell Motil.*, 5:251–263, 1985.
- [132] U. Rüffer and W. Nultsch. Flagellar photoresponses of chlamydomonas cells held on micropipettes: I. change in flagellar beat frequency. *Cell Motil. Cytoskeleton*, 15:162–167, 1990.
- [133] U. Rüffer and W. Nultsch. Flagellar photoresponses of chlamydomonas cells held on micropipettes: Ii. change in flagellar beat pattern. *Cell Motil. Cytoskeleton*, 18:269–278, 1991.
- [134] U. Rüffer and W. Nultsch. Flagellar photoresponses of chlamydomonas cells held on micropipettes: Iii. shock response. *Bot. Acta*, 108:255–265, 1995.
- [135] U. Rüffer and W. Nultsch. Flagellar coordination in chlamydomonas cells held on micropipettes. *Cell Motil. Cytoskeleton*, 41:297–307, 1998.
- [136] E. Ruiz-Pesini, C. Diez, C. Lapen, A. Perez-Martos, J. Montoya, E. Alvarez, J. Arenas, and M.J. Lopez-Perez. Correlation of sperm motility with mitochondrial enzymatic activities. *Clin. Chem.*, 44 (8):1616–1620, 1998.
- [137] S.S. Sadhal and M.S. Plesset. Effect of solid properties and contact angle drop-wise condensation and evaporation. *J. Heat Transfer*, 101:48–54, 1979.

- [138] D. Saintillan and M.J. Shelley. Orientational order and instabilities in suspensions of self-locomoting rods. *Phys. Rev. Lett.*, 99:058102, 2007.
- [139] M.F. Schatz and G.P. Neitzel. Experiments on thermocapillary instabilities. *Ann. Rev. Fluid Mech.*, 33:93 – 127, 2001.
- [140] E. Schmidt, W. Schurig, and W. Sellschopp. Versuche über die kondensation von wasserdampf in film- und tropfenform. *Techn. Mech. u. Thermodynam.*, 1:53, 1930.
- [141] L.E. Scriven and C.V. Sternling. On cellular convection driven by surface-tension gradients: effects of mean surface tension and surface viscosity. *J. Fluid Mech.*, 19:321–340, 1964.
- [142] A. Shapere and F. Wilczek. Self-propulsion at low reynolds number. *Phys. Rev. Lett.*, 58 (20):2051–2054, 1987.
- [143] A. Shapere and F. Wilczek. Efficiencies of self-propulsion at low reynolds number. *J. Fluid Mech.*, 198:587–599, 1989.
- [144] A. Shapere and F. Wilczek. Geometry of self-propulsion at low reynolds number. *J. Fluid Mech.*, 198:557–585, 1989.
- [145] M.B. Short, C.A. Solari, S. Ganguly, T.R. Powers, J.O. Kessler, and R.E. Goldstein. Flows driven by flagella of multicellular organisms enhance long-range molecular transport. *Proc. Nat. Acad. Sci. U.S.A.*, 103 (22):8315–8319, 2006.
- [146] R.R. Snook. Sperm in competition: not playing by the numbers. *Trends Ecol. Evol.*, 20(1):46–53, 2005.
- [147] C.A. Solari, S. Ganguly, J.O. Kessler, R.E. Michod, and R.E. Goldstein. Multicellularity and the functional interdependence of motility and molecular transport. *Proc. Nat. Acad. Sci. U.S.A.*, 103 (5):1353–1358, 2006.
- [148] R. Stocker, J.R. Seymour, A. Samadani, Hunt D.E., and M.F. Polz. Rapid chemotactic response enables marine bacteria to exploit ephemeral microscale nutrient patches. *Proc. Natl. Acad. Sci. USA*, 105:4209–4214, 2008.
- [149] H.A. Stone, A.D. Stroock, and A. Ajdari. Engineering flows in small devices: microfluidics toward a lab-on-a-chip. *Ann. Rev. Fluid Mech.*, 36:381–411, 2004.
- [150] R.S. Subramanian and R. Balasubramaniam. *The motion of bubbles and drops in reduced gravity*. Cambridge university press, Cambridge, 2001.
- [151] S. Sudo, R. Orikasa, and T. Honda. Locomotive characteristics of swimming mechanism propelled by alternating magnetic field. *Int. J. Appl. Electromagnet Mech.*, 19:263–267, 2004.
- [152] D. Tam and A.E. Hosoi. Optimal stroke patterns for purcell’s three-link swimmer. *Phys. Rev. Lett.*, 98:068105, 2007.

- [153] D. Tam and A.E. Hosoi. Tam and Hosoi reply. *Phys. Rev. Lett.*, 100:029802, 2008.
- [154] G.I. Taylor. Analysis of the swimming of microscopic organisms. *Proc. R. Soc. London, Ser. A*, 209:447–461, 1951.
- [155] G.I. Taylor. The action of waving cylindrical tails in propelling microscopic organisms. *Proc. R. Soc. London, Ser. A*, 211:225–239, 1952.
- [156] O.C. Thomas, R.E. Cavicchi, and M. Tarlov. Effect of surface wettability on fast transient microboiling behavior. *Langmuir*, 19(15):6168 – 6177, 2003.
- [157] J.P.K. Tillett. Axial and transverse stokes flow past slender axisymmetric bodies. *J. Fluid Mech.*, 44(3):401–417, 1970.
- [158] A.K. Tornberg and K. Gustavson. A numerical method for simulations of rigid fiber suspensions. *J. Comput. Phys.*, 215:172–196, 2006.
- [159] A.K. Tornberg and M.J. Shelley. Simulating the dynamics and interactions of flexible fibers in stokes flows. *J. Comput. Phys.*, 196:8–40, 2004.
- [160] C.H. Wang and V.K. Dhir. Effect of surface wettability on active nucleation site density during pool boiling of water on a vertical surface. *J. Heat Transfer*, 115:659, 1993.
- [161] P. Weiss. Artificial animalcules. *Science news*, 169(7):107, 2006.
- [162] K.A. Wemmer and W.F. Marshall. Flagellar motility: all put together. *Curr. Biol.*, 14:992–993, 2004.
- [163] R.N. Wenzel. Resistance of solid surfaces to wetting by water. *Ind. Eng. Chem.*, 28(8):988, 1936.
- [164] C.H. Wiggins and R.E. Goldstein. Flexive and propulsive dynamics of elastica at low reynolds number. *Phys. Rev. Lett.*, 80 (17):3879–3882, 1998.
- [165] D.E. Wilson and D.M. Reeder. *Mammal Species of the World, third edition*. Johns Hopkins University Press, Baltimore, 2005.
- [166] R. Wood. Fly, robot fly. *IEEE Spectr.*, March 2008:25–29, 2008.
- [167] A. Yamazaki, M Sendoh, K. Ishiyama, T. Hayase, and K.I. Arai. Three-dimensional analysis of swimming properties of a spiral-type magnetic micro-machine. *Sens. Actuators*, 105:103–108, 2003.
- [168] K. Yoshimura, C. Shingyoji, and K. Takahashi. Conversion of beating mode in chlamydomonas flagella induced by electric stimulation. *Cell Motil. Cytoskeleton*, 36:236–245, 1997.

- [169] T.S. Yu, E. Lauga, and A.E. Hosoi. Experimental investigations of elastic tail propulsion at low reynolds number. *Phys. Fluids*, 18(9):685–711, 2006.
- [170] L. Zhai, F.C. Cebeci, R.E. Cohen, and M.F. Rubner. Stable superhydrophobic coatings from polyelectrolyte multilayers. *Nano Lett.*, 4:1349–1353, 2004.
- [171] N. Zhao, J. Xu, Q. Xie, L. Weng, X. Guo, X. Zhang, and L. Shi. Fabrication of biomimetic superhydrophobic coating with a micro-nano-binary structure. *Macromol. Rapid Commun.*, 26:1075 – 1080, 2005.